



HAL
open science

**Propriétés structurales et magnétiques dans les
composants de manganèse $\text{Ln}_{0.5}\text{Ca}_{0.5}\text{MnO}_3$ ($\text{Ln}=\text{La}$,
 Pr , Nd , ..., Lu): Une étude systématique par diffusion
des neutrons et calculs ab initio.**

Emanuela Pusceddu

► **To cite this version:**

Emanuela Pusceddu. Propriétés structurales et magnétiques dans les composants de manganèse $\text{Ln}_{0.5}\text{Ca}_{0.5}\text{MnO}_3$ ($\text{Ln}=\text{La}$, Pr , Nd , ..., Lu): Une étude systématique par diffusion des neutrons et calculs ab initio.. Autre [cond-mat.other]. Université de Grenoble, 2011. Français. NNT : 2011GRENY021 . tel-00609199

HAL Id: tel-00609199

<https://theses.hal.science/tel-00609199>

Submitted on 18 Jul 2011

HAL is a multi-disciplinary open access archive for the deposit and dissemination of scientific research documents, whether they are published or not. The documents may come from teaching and research institutions in France or abroad, or from public or private research centers.

L'archive ouverte pluridisciplinaire **HAL**, est destinée au dépôt et à la diffusion de documents scientifiques de niveau recherche, publiés ou non, émanant des établissements d'enseignement et de recherche français ou étrangers, des laboratoires publics ou privés.

THÈSE

Pour obtenir le grade de

DOCTEUR DE L'UNIVERSITÉ DE GRENOBLE

Spécialité : **Physique de la Matière et du Rayonnement**

Arrêté ministériel : 7 août 2006

Présentée par

Emanuela PUSCEDDU

Thèse dirigée par **Mark R. Johnson**

et codirigée par **Claudia Mondelli**

préparée au sein **Institute Laue Langevin**

et de **Université de Grenoble**

Structure and magnetic properties in half-doped manganites $\text{Ln}_{0.5}\text{Ca}_{0.5}\text{MnO}_3$ (Ln=La, Pr, Nd, ..., Lu). A systematic study by neutron scattering and ab-initio calculations.

Thèse soutenue publiquement le **16 Mai 2011**,
devant le jury composé de :

M. Olivier Isnard

Professeur, Université de Grenoble, Président

M. Sergio DiMatteo

Professeur, Université de Rennes 1, Rapporteur

M. Vincenzo Fiorentini

Professeur, Università di Cagliari, Rapporteur

M. Maurizio Ferretti

Professeur, Università di Cagliari, Examineur

M. Mark R. Johnson

Professeur, ILL, Directeur de thèse

Mme. Claudia Mondelli

Docteur, CNR-IOM, ILL, Co-Directeur de thèse



Remerciements

Beaucoup des personnes ont contribué directement ou indirectement à m'aider à mener bonne fin ce travail de thèse et je voudrais exprimer mes plus sincères remerciements à tous.

Merci à Claudia Mondelli pour m'avoir introduit dans le monde des manganites, pour m'avoir proposé ce travail de thèse et m'avoir guidée avec patience et constance pendant toutes ces années.

Merci à Mark R. Johnson pour avoir été mon directeur de thèse et pour avoir suivi attentivement son développement avec des bonnes suggestions.

Je suis très reconnaissante à tous les membres du jury de thèse: à mes deux rapporteurs Sergio DiMatteo et Vincenzo Fiorentini pour avoir accepté ce travail ingérant et l'avoir accompli avec grande patience; à Olivier Isnard et Maurizio Ferretti pour l'agréable partage de connaissances, pour les suggestions et leur questions lors de la soutenance.

Ce travail a été réalisé au sein du groupe CS (Computing for Science) de l'Institut Laue Langevin à Grenoble; merci à tous les membres du groupe pour l'agréable accueil et l'aide pendant ces ans, plus particulièrement Eric Pellegrini pour les précieuses indications et conseils.

Des remerciements tout particuliers à Mohamed Zbiri les discussions et les bonnes suggestions dans la partie des simulations. Merci beaucoup à Silvia Capelli, Aziz Daoud-Aladine et Juan Rodriguez-Carvajal pour leurs aide précieuse dans la partie de diffraction. Je voudrais remercier Roberta Cimberle, Carlo Tropeano et Gustavo Varvaro pour nous avoir donné les mesures de susceptibilité.

Il est impossible de remercier toutes les personnes qui ont contribué, directement ou indirectement, généralement de façon complètement inconsciente à me faire devenir celle que je suis aujourd'hui, après ces ans. Pour avoir vécu avec moi une période très importante de ma vie, à ces personnes va toute ma reconnaissance, ce qui est bien plus important que ne le serait une liste à l'ordre nécessairement trompeur.

Contents

1	Physical properties of manganites	21
1.1	Phase diagram	23
1.2	Rare earth manganites	27
1.3	Electronic structure and magnetic exchange	28
1.3.1	Jahn-Teller effect	29
1.3.2	Superexchange interaction	32
1.3.3	Double exchange and Zener model	32
1.3.4	Magnetic and electronic properties in phase diagrams: conclusions	35
2	Experimental approach and methods	41
2.1	Static magnetic properties: magnetization and uniform susceptibility . . .	42
2.1.1	DC SQUID magnetometry	43
2.2	Neutron scattering	45
2.2.1	Neutron properties	46
2.2.2	Neutron diffraction	47
2.3	Refinement of neutron powder diffraction data	50
2.3.1	Rietveld method	50
2.3.2	Layout of neutron diffractometers	54
3	Experimental results and discussion	59
3.1	Half-doped manganites series: synthesis	61
3.2	Bulk magnetic properties: susceptibility measurements	62
3.3	Nuclear and magnetic structure of $\text{Ln}_{0.5}\text{Ca}_{0.5}\text{MnO}_3$ compounds	67
3.4	Systematic study as a function of Ln ionic radius	76
3.5	Conclusions	79
4	Computational methods: theory and practice	85
4.1	First principle	88
4.2	Density functional theory	89
4.2.1	Exchange-correlation functional	91
4.2.2	Pseudo-potential Approximation	92
4.2.3	Projected Augmented Waves Approximation	94
4.2.4	LDA and GGA approximations	95
4.2.5	The Hubbard model: GGA+U	95
4.2.6	DFT in practice: VASP	96
5	Computational results	101
5.1	Calculation model	102
5.2	Structure geometry optimization	103
5.3	Comparison between experimental and computational structural data . . .	106

5.4	Magnetic properties	110
5.5	$Nd_{0.5}Ca_{0.5}MnO_3$ and $Lu_{0.5}Ca_{0.5}MnO_3$ super-cell structures	117
5.5.1	Electronic density of states of $Nd_{0.5}Ca_{0.5}MnO_3$ and $Lu_{0.5}Ca_{0.5}MnO_3$ super-cells	118
5.6	Conclusions	121
6	General conclusions	127
A	Magnetism	135
A.1	Ferromagnetism	136
A.1.1	Curie Temperature	136
A.2	Antiferromagnetism	137
A.2.1	Weiss model of an antiferromagnet and Neèl temperature	137
A.2.2	Critical Temperature	138
A.3	Paramagnetism and Diamagnetism	139
A.3.1	Paramagnetism	139
A.3.2	Diamagnetism	140
B	Systematic study of half-doped manganites	141
B.0.3	Pnma vs. Pbnm symmetry group	141
B.0.4	Structural and magnetic properties of $Ln_{0.5}Ca_{0.5}MnO_3$, $Ln = Dy, Ho, Er, Tm$ and Lu	142

List of Tables

2.1	Neutron properties	52
3.1	Table of samples, electronic configuration of the atoms, ionic radius in Å of Ln and the instruments used.	69
3.2	Table of Néel temperature T_N , charge ordering temperature T_{CO} and C_{LT}/C_{HT} obtained by inverse susceptibility analysis.	73
3.3	$\text{Pr}_{0.5}\text{Ca}_{0.5}\text{MnO}_3$, $\text{Nd}_{0.5}\text{Ca}_{0.5}\text{MnO}_3$ and $\text{Lu}_{0.5}\text{Ca}_{0.5}\text{MnO}_3$ structural parameters determined at room and low T temperature; the manganese atom is in high symmetry site (1/2, 0, 0). We have compared $\text{Nd}_{0.5}\text{Ca}_{0.5}\text{MnO}_3$ structural and magnetic parameters, at low temperature, with available results in lecture [69]. We found the pseudo-CE magnetic phase; we reported the modules of μ_{Mn}^{3+} and μ_{Mn}^{4+} , plane-angle of φ , space-angle of ϑ associated at spin vector of Mn atom.	77
5.1	External electronic configuration considered in PAW data sets	109
5.2	Convergence parameters and final energy of relaxation of CaMnO_3 with and without Hubbard correction, in FM and AFM (G-type) spin configurations.	110
5.3	Convergence parameters and final energy of relaxation of NdMnO_3 with and without Hubbard approximation, in FM and AFM (A-type) spin configurations.	112
5.4	Convergence parameters and final energy of relaxation of $\text{Nd}_{0.5}\text{Ca}_{0.5}\text{MnO}_3$ calculated with and without Hubbard correction, in FM and AFM (C-type) spin configurations.	112

5.5	Cell parameters, volume, bond lengths and angles of CaMnO_3 from DFT-VASP calculations, with and without Hubbard approximation, in FM and AFM spin configurations, compared with the available experimental data [102].	113
5.6	Structural parameters of NdMnO_3 single cell with and without Hubbard approximation, in FM and AFM configuration, compared with the experimental results [101].	114
5.7	Cell parameters, volume, bond lengths and angles of $\text{Nd}_{0.5}\text{Ca}_{0.5}\text{MnO}_3$, NdCa_a (see figure 5.1(a)) compared with our experimental results (obtained on D20 instrument at ILL).	116
5.8	Values of total energy in eV for CaMnO_3 . The details of calculations are specified in the text. ΔE corresponds to the variation of the energy with respect to the appropriate minimum values.	118
5.9	Values of total energy in eV for CaMnO_3 calculated for three different values of Coulomb interaction, $U = 6.9 \text{ eV} - 7.9 \text{ eV} - 8.9 \text{ eV}$, in the GGA+U approach.	118
5.10	Values of total energy in eV for NdMnO_3 . The details of calculations are specified in the text. ΔE corresponds to the variation of the energy with respect to the appropriate minimum values.	120
5.11	Values of total energy in eV for the half-doped Nd-Ca system. The details of calculations are specified in the text. ΔE corresponds to the variation of the energy with respect to the appropriate minimum values.	121
5.12	$\text{Nd}_{0.5}\text{Ca}_{0.5}\text{MnO}_3$ and $\text{Lu}_{0.5}\text{Ca}_{0.5}\text{MnO}_3$ structural features: cell parameters, bond distances Mn-O and bond angles Mn-O-Mn, without Hubbard correction.	123
B.1	Table of firsts and second phase of our samples, obtained by Rietveld refinement of NPD data measured on D1A and D20 at ILL, at $\lambda = 1,9 \text{ [\AA]}$	148
B.2	$\text{Dy}_{0.5}\text{Ca}_{0.5}\text{MnO}_3$, $\text{Ho}_{0.5}\text{Ca}_{0.5}\text{MnO}_3$ and $\text{Er}_{0.5}\text{Ca}_{0.5}\text{MnO}_3$ structural parameters determined at room and lower temperature, measured on D1A at ILL, at $\lambda = 1,9 \text{ [\AA]}$; the manganese atom is in high symmetry site $(1/2, 0, 0)$	149

- B.3 $\text{Tm}_{0.5}\text{Ca}_{0.5}\text{MnO}_3$ and $\text{Lu}_{0.5}\text{Ca}_{0.5}\text{MnO}_3$ structural parameters determined at room and lower temperature, measured on D1A at ILL, at $\lambda = 1,9 \text{ [\AA]}$; the manganese atom is in high symmetry site $(1/2, 0, 0)$. 152

List of Figures

1	Typical perovskite structures of manganites ([4]).	14
2	Possible magnetic spin configuration in manganitic compounds [5]. . .	14
3	5d-Mn level split into t_{2g} (d_{xy} , d_{xz} , and d_{yz}) and e_g ($d_{x^2-y^2}$, d_{z^2}) sublevels.	16
1.1	Typical perovskite structures of manganites [4]	27
1.2	$\text{La}_{1-x}\text{Ca}_x\text{MnO}_3$ phase diagram for polycrystalline samples reproduced from Tomioka et al. [15].	29
1.3	The charge and orbital ordering configurations for $\text{Ln}_{1-x}\text{Ca}_x\text{MnO}_3$, $x = 0.5$. Circles are Mn^{+4} and the lobes show the orbital ordering of the e_g -electrons of Mn^{+3}	32
1.4	Phase diagrams of $\text{Pr}_{1-x}\text{Ca}_x\text{MnO}_3$ reproduced by C. Martin et al. [24]	32
1.5	Field splitting of the five-fold degenerate atomic 5d levels into lower t_{2g} and higher e_g levels.	35
1.6	Sketch of the Q2 JT distortion in the ab plane, obeying Pbnm symmetry. Mn atoms are represented by the circles. Closed arrows indicate the movement associated with the JT distortion.	36
1.7	Field splitting of Mn-5d orbital, t_{2g} and e_g , in particular Jahn-Teller distortion shown in the figure further lifts each degeneracy.	37
1.8	Superexchange interaction between manganese and oxygen atoms. The three panels result in an (i) antiferromagnetic, (ii) antiferromagnetic and (iii) ferromagnetic arrangement of the core manganese spins respectively.	39
1.9	Draw of the double-exchange mechanism which involves two Mn ions and one O ion.	40

1.10	Phase diagram of $\text{La}_{1-x}\text{Sr}_x\text{MnO}_3$ (by Y. Tokura and Y. Tomioka) prepared with data from Urushibara et al. [52] and Fujishiro et al. [53].	42
1.11	Phase diagram of $\text{Nd}_{1-x}\text{Sr}_x\text{MnO}_3$, reproduced from Kajimoto et al. [54].	42
2.1	Susceptibility of $\text{Nd}_{0.5}\text{Ca}_{0.5}\text{MnO}_3$ obtained by SQUID measurement.	50
2.2	Scheme of the MPMS-5S Squid magnetometer showing: (a) second-derivative coil; (b) the Squid loop; (c) the response signal. . .	51
2.3	Sketch of a neutron scattering experiment	52
2.4	A scattering event in real space (a); the corresponding triangle scattering (b)	53
2.5	Sketch of two-dimensional unit cells, without a basis (a) and with basis (b).	54
2.6	The Ewald construction for the powder diffraction method.	56
2.7	Pattern of $\text{Nd}_{0.50}\text{Ca}_{0.50}\text{MnO}_3$ obtained by Rietveld method refinement.	57
2.8	High-resolution diffractometer D1A at ILL	61
2.9	High-resolution diffractometer D20 at ILL	62
3.1	Lanthanide atoms and corrispectively neutron scattering absorption cross section in barn for 0.0253 eV stands for estimated values [64]. .	67
3.2	Susceptibility measurement, by SQUID, of $\text{Pr}_{0.5}\text{Ca}_{0.5}\text{MnO}_3$, $\text{Nd}_{0.5}\text{Ca}_{0.5}\text{MnO}_3$, and $\text{Lu}_{0.5}\text{Ca}_{0.5}\text{MnO}_3$ in FC and ZFC, in the temperature range 5 ÷ 530 K.	70
3.3	Inverse susceptibility of $\text{Pr}_{0.5}\text{Ca}_{0.5}\text{MnO}_3$, $\text{Nd}_{0.5}\text{Ca}_{0.5}\text{MnO}_3$, $\text{Yb}_{0.5}\text{Ca}_{0.5}\text{MnO}_3$, $\text{Er}_{0.5}\text{Ca}_{0.5}\text{MnO}_3$ and $\text{Lu}_{0.5}\text{Ca}_{0.5}\text{MnO}_3$, in the temperature range 0 ÷ 530 K.	72
3.4	Diffraction pattern of $\text{Pr}_{0.5}\text{Ca}_{0.5}\text{MnO}_3$ at $T = 300\text{K}$, and $\text{Pr}_{0.5}\text{Ca}_{0.5}\text{MnO}_3$ at $T = 20\text{ K}$, $\text{D20}, \lambda = 1,9 [\text{Å}]$. The lower solid lines show the difference profiles and the tick marks show the reflection positions. .	75
3.5	Scheme of CE and <i>pseudo</i> -CE magnetic structure. The arrows in gray of the upper planes correspond to the translation of the magnetic moment of the Mn placed must below, in order to visualize the angle θ between the two magnetic moment [68].	76
3.6	Pattern of $\text{Lu}_{0.5}\text{Ca}_{0.5}\text{MnO}_3$ at $T = 300\text{ K}$ and $\lambda = 1,9 \text{ Å}$	78

3.7	Pr _{0.5} Ca _{0.5} MnO ₃ with the orthorhombic polyhedron MnO ₆ . The Pr/Ca atoms are represented with silver color, the O atoms in red color and the Mn atoms, inside the polyhedron, in magenta color.	78
3.8	Cell parameters, Jahn-Teller effect, Tilting of octahedra and susceptibility of Pr _{0.5} Ca _{0.5} MnO ₃ and Nd _{0.5} Ca _{0.5} MnO ₃ . In the square, we emphasize the charge ordering region.	79
3.9	Bandwidth of e _g -Mn calculated for Nd _{0.5} Ca _{0.5} MnO ₃ on the basis of eq.(1.1).	80
3.10	Magnetic moment Mn ³⁺ and Mn ⁴⁺ as a function of temperature for Ln _{0.5} Ca _{0.5} MnO ₃ , where Ln = Pr, Nd, Ho and Lu.	81
3.11	Cell parameters, Jahn-Teller effect, Mn-O-Mn bond angles and susceptibility of Lu _{0.5} Ca _{0.5} MnO ₃	82
3.12	Cell parameters, Jahn-Teller distortion and tilting effect as a function of lanthanide ionic radius, at room temperature.	83
3.13	Percentage variation of the magnetic moments associate to Mn ³⁺ -Mn ⁴⁺ as a function of Ln ionic radius at lowest temperature. The percentage variation of the magnetic moments for the LaCa compounds is obtained by Radaelli et al. [28].	84
4.1	Schematic illustration of the potential and the wavefunction to any electrons (solid lines), and the pseudopotential and pseudofunction respectively (drawn lines). The values of two curves intersection is r _c [87].	99
5.1	Arrangement Neodymium (gray circles)-Calcium (green circles) (Nd/Ca) in the three different cases for Nd _{0.5} Ca _{0.5} MnO ₃ system simulated	108
5.2	CaMnO ₃ structure obtained from geometry relaxation simulation with the Hubbard correction.	110
5.3	The trend of forces acting on atoms (max and average) during geometry optimisation. This example relates to the Nd-Ca half-doped system in the antiferromagnetic, C-type spin configuration, without Hubbard correction.	111
5.4	Nd _{0.5} Ca _{0.5} MnO ₃ system obtained from geometry relaxation simulation in GGA+U approach. In red circles: O; in magenta circles: Mn; in gray circles: Nd; in green circles: Ca.	115

5.5	Layout of AFM structure of simulated systems: A-type for the NdMnO_3 (FM in the plane and AFM between the planes), G-type for the CaMnO_3 (completely AFM) and C-type for the $\text{Nd}_{0.5}\text{Ca}_{0.5}\text{MnO}_3$ (AFM in the plane and FM between the planes.) Note that in a single cell only Mn are present and we cannot describe the whole spin configuration in all cases.	117
5.6	CaMnO_3 : the orbital-decomposed partial electronic density of state of Mn 3d components, in CaMnO_3 : $d_{x^2-y^2}$ and d_{z^2} for e_g , and d_{xy} , d_{xz} and d_{yz} for t_{2g}	119
5.7	NdMnO_3 : the orbital-decomposed partial electronic density of state of Mn 3d components: $d_{x^2-y^2}$ and d_{z^2} for e_g , and d_{xy} , d_{xz} and d_{yz} for t_{2g} , in the NdMnO_3 system.	121
5.8	$\text{Nd}_{0.5}\text{Ca}_{0.5}\text{MnO}_3$: the orbital-decomposed partial electronic density of state of Mn 3d components: $d_{x^2-y^2}$ and d_{z^2} for e_g , and d_{xy} , d_{xz} and d_{yz} for t_{2g} , calculated for $\text{Nd}_{0.5}\text{Ca}_{0.5}\text{MnO}_3$	122
5.9	The total and partial DOS for $\text{Nd}_{0.5}\text{Ca}_{0.5}\text{MnO}_3$ in FM and AFM CE-type magnetic structure.	125
5.10	The total and partial DOS for $\text{Lu}_{0.5}\text{Ca}_{0.5}\text{MnO}_3$ in FM and AFM CE-type magnetic structure.	126
A.1	The mean-field magnetization as function of temperature, performed for different values of J.	145
B.1	Pattern of $\text{Dy}_{0.5}\text{Ca}_{0.5}\text{MnO}_3$ at $T = 300$ K and $\lambda = 1.9 \text{ \AA}$	150
B.2	Pattern of $\text{Ho}_{0.5}\text{Ca}_{0.5}\text{MnO}_3$ at $T = 300$ K and $\lambda = 1.9 \text{ \AA}$	150
B.3	Pattern of $\text{Er}_{0.5}\text{Ca}_{0.5}\text{MnO}_3$ at $T = 300$ K and $\lambda = 1.9 \text{ \AA}$	151
B.4	Pattern of $\text{Tm}_{0.5}\text{Ca}_{0.5}\text{MnO}_3$ at $T = 300$ K and $\lambda = 1.9 \text{ \AA}$	151

Introduction

The study of manganites started in 1950 with Jonker and Van Santen [1], which demonstrated the existence of ferromagnetism in mixed crystals of LaMnO_3 - CaMnO_3 , LaMnO_3 - SrMnO_3 . Systems with general formula $\text{Ln}_{0.5}\text{B}_{0.5}\text{MnO}_3$, where Ln corresponds to the tri-valent lanthanide atoms, for example lanthanum, neodymium or praseodymium, and B to the divalent alkali metals, such as calcium, strontium or barium, show particularly interesting magnetic behavior. Manganese, with its five 3d and two 4s electrons, is a transition metal. As such, it exhibits variable valence and forms stable compounds in several formal oxidation states. Jonker and Van Santen were the first to crystallize mixed-valence manganites [1]. They referred to these compounds as 'manganites', somewhat of a misnomer however, since the term should only apply to compounds containing tetravalent manganese, like $\text{MnO}(\text{OH})$ for example. They realized that the manganites crystallized in a perovskite structure, where every manganese ion is surrounded by an octahedron of oxygens. The Ln-site of the perovskite structure contains the largest ion. Manganese, on the other hand, is the smallest ion involved. Jonker and Van Santen obtained the Curie temperature of $\text{La}_{1-x}\text{Ca}_x\text{MnO}_3$ as a function of calcium content x .

At this point, it is interesting to note what this parameter x does in the composition. In the $(\text{La,Ca})\text{MnO}_3$ case, for example, calcium is in an oxidation state 2+, while lanthanum is 3+. Accordingly, every time a lanthanum ion is replaced by calcium, a manganese is forced into oxidation state 4+ to preserve charge neutrality. In other words, introducing one calcium removes one electron from the manganese. Condensed matter physicists like to call this process 'doping with holes'. The relative fraction of Mn^{+3} and Mn^{+4} is regulated by x percentage composition.

The ideal perovskite structure is cubic: the rare-earth cations occupy the corners of the unit cell and the small manganese cation is in the centre and is octahedrally coordinated by oxygen, in the perovskite structure, as illustrated in figure 1, by Wollan [2] and Koehler [3]. They described also the charge ordering state (CO)

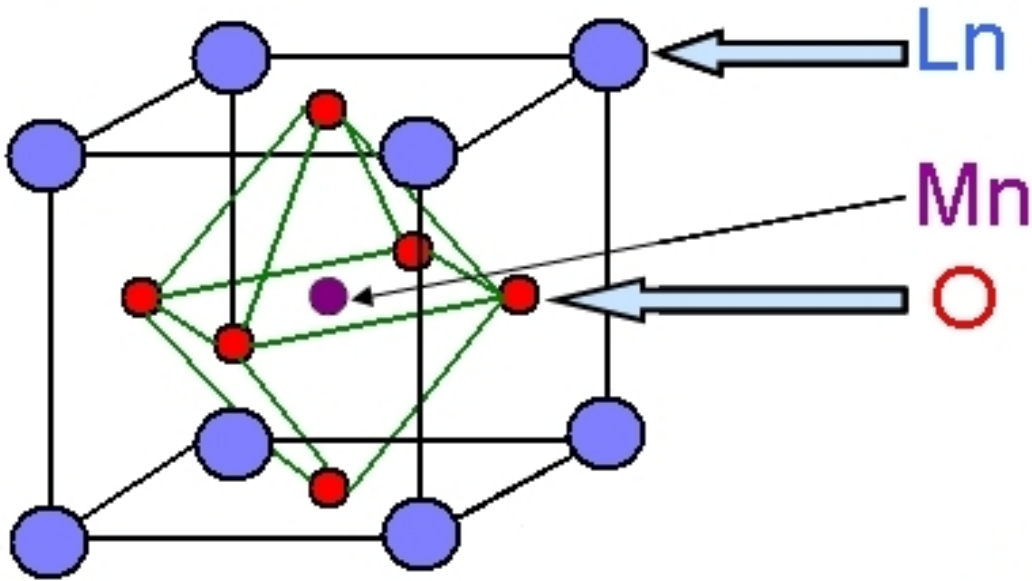


Figure 1: Typical perovskite structures of manganites ([4]).

at $x = 0.50$ as a CE-type [3], which corresponds to a mixture of the C- and E-type magnetic unit cells. There are seven possible arrangements for the spin of manganese atoms in the unit cell (A, B, C, D, E, F, and G), as illustrated in figure 2 [5].

Antiferromagnetism is a form of magnetic order where local moments (such as the

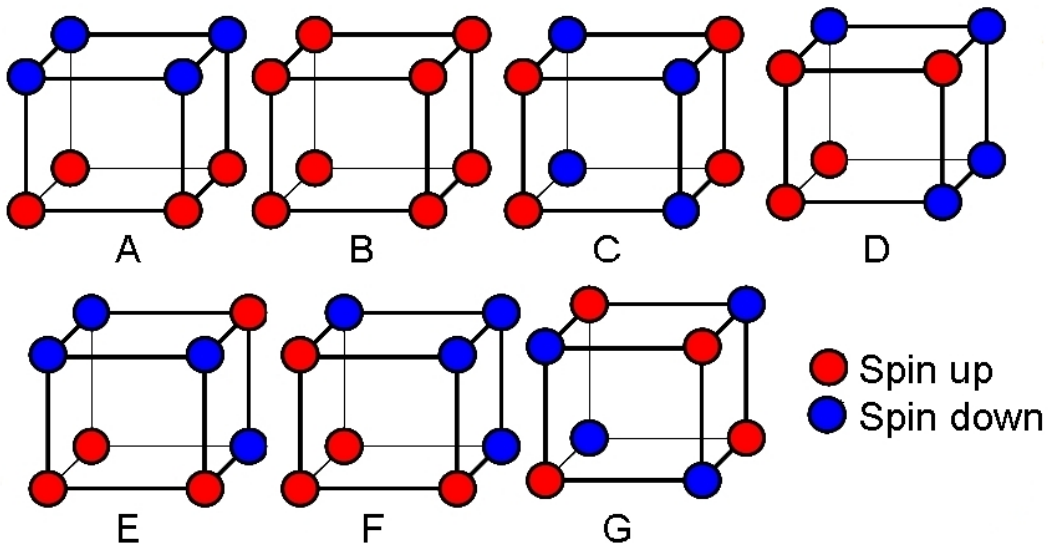


Figure 2: Possible magnetic spin configuration in manganitic compounds [5].

one caused in manganese ions by aligning the electrons in the unfilled d-shell) can be divided into two equivalent *interpenetrating sublattices*.

Until 1949, the only available methods of detecting antiferromagnetism were indirect, e.g., susceptibility or anomalies in specific heat measurements. The situation changed when it occurred to J. Samuel Smart that neutron diffraction experiments might provide a direct means of detecting antiferromagnetism' [6]. Few years after Jonker and van Santen's studies, Wollan and Koehler used neutron scattering to study the spin structure of manganites [3]. Not only did they observe the antiferromagnetism expected from MnO, but they also discovered a few possible different spin arrangements as a function of x , such as the A, C and G types of magnetic order shown in figure 2. In the paper immediately following Wollan and Koehler's, John Goodenough [5] put forward a theory attributing this variety of structures to covalence.

Surprisingly enough, the field of manganites received very little attention from the experimental community after this initial effort. Theoretical work went on for another couple of years. All these early theoretical studies, which will be reviewed later, suffered from the same limitation: the electronic states considered were always taken to be uniform.

Experimental interest was finally revived in 1989 with the observation of a large magnetoresistance (MR) effect in $\text{Nd}_{0.5}\text{Pb}_{0.5}\text{MnO}_3$ by Kusters et al. [7] and in $\text{La}_{2/3}\text{Ba}_{1/3}\text{MnO}_3$ by von Helmolt et al. [8]. As a matter of fact, Searle and Wang had reported large magnetoresistance in single crystals of $\text{Pr}_{1-x}\text{Ca}_x\text{MnO}_3$ as early as 1969 [9]. In simple terms, the magnetoresistance effect refers to the change in transport behavior under the application of a magnetic field. $\text{Pr}_{0.7}\text{Ca}_{0.3}\text{MnO}_3$, for example, is an insulator in zero field. Application of a one Tesla magnetic field changes the low temperature behavior, turning it into a conductor.

The interesting feature in the manganites is the phenomenology arising from the d-orbitals of the manganese atom. In the cubic lattice environment, the five-fold degenerate, 3d-orbitals of an isolated atom or ion are split into a manifold of three lower energy levels (d_{xy} , d_{xz} , and d_{yz} , see fig. 3), usually referred to as t_{2g} once mixing with the surrounding oxygens is included, and two higher energy states ($d_{x^2-y^2}$ and d_{z^2} , see fig. 3) called e_g (see figure 3). The valence of the Mn-ions in this context is either four (Mn^{3+}) or three (Mn^{4+}), and their relative fraction is controlled through chemical doping. In the low-bandwidth compounds, i.e. the $e_g(\text{Mn})$ - $2p\sigma(\text{O})$ - $e_g(\text{Mn})$ orbital overlap determined by the Mn-O distance ($d_{\text{Mn-O}}$) and the Mn-O-Mn angle (ω), like $\text{Pr}_{0.5}\text{Ca}_{0.5}\text{MnO}_3$, a charge-order state

of Mn^{3+} and Mn^{4+} is stabilized in the vicinity of $x = 0.5$. The charge ordering (CO) is considered as the ordering of cations with different formal valencies, e.g. $\text{Mn}^{3+}/\text{Mn}^{4+}$ in mixed-valence manganites.

The aim of this work is to realize a systematic study of the structural, electronic

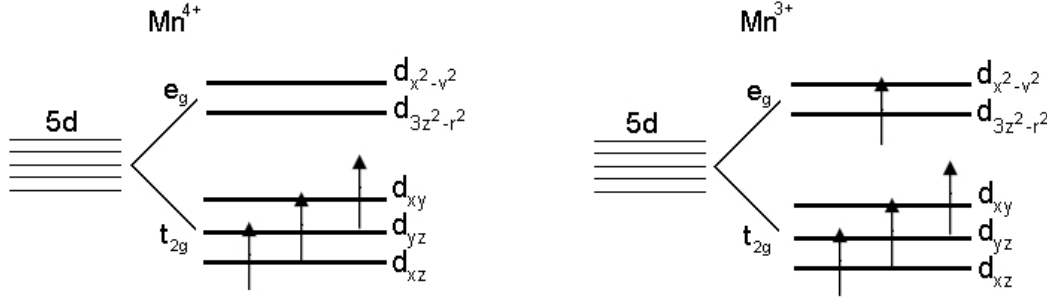


Figure 3: 5d-Mn level split into t_{2g} (d_{xy} , d_{xz} , and d_{yz}) and e_g ($d_{x^2-y^2}$, d_{z^2}) sublevels.

and magnetic properties of Ca half-doped manganite family: $\text{Ln}_{0.50}\text{Ca}_{0.50}\text{MnO}_3$ (Ln = Rare Earth). In particular we focused our attention on charge ordering and orbital ordering phenomena that are generally present at this composition. We derived a microscopic model of nuclear and magnetic structure using both neutron powder diffraction techniques and ab-initio calculations in order to compare experimental results and numerical models and to understand the role of chemical and magnetic in-homogeneity in these systems.

The change in the electronic and spin state of the transition metal by doping, is associated to a structural modification of the geometry of the legands around the transition metal. That induces cooperative structural modifications that are observable by neutron diffraction. In contrast with this order induced by doping, an intrinsic chemical disorder is associated with the doping element on the A site of the perovskite (general formula ABO_3) on which the trivalent (Ln^{3+}) and divalent ions (Ca^{2+}) reside. This disorder is due to the difference of the ionic radius and chemical affinity between these ions. In order to study systematically the effect of the A site substitution and the relation between the structural properties (structural and magnetic) and the macroscopic magnetic properties, several samples have been synthesised and characterised by macroscopic magnetic measurements. Neutron diffraction is a fundamental step towards understanding the relation between the structural and macroscopic properties. The resulting structures represent a good starting point for ab-initio calculations in the study of magnetic structure and CO/OO phenomena, which can possibly validate the diffraction results and give

access to the underlying electronic structure.

In chapter one of this thesis, after a description of the phase diagram of the most studied manganites ($\text{La}_{1-x}\text{Ca}_x\text{MnO}_3$), the physical properties of manganites and the most important concepts and models to understand them are described: Jahn-Teller effect, super-exchange interaction, double exchange and the Zener model.

In the second chapter a brief introduction to all experimental techniques used in this study will be presented. The macroscopic magnetic properties have been measured as a function of temperature by using a SQUID magnetometer described in this chapter. The principal microscopic technique used for this thesis was neutron powder diffraction. The technique and the layout of the instruments - D20 and D1A at the Institute Laue Langevin, Grenoble - are described together with details of the Rietveld method used to refine this data to extract all structural informations.

In chapter three, experimental results from the systematic study of the $\text{Ln}_{0.50}\text{Ca}_{0.50}\text{MnO}_3$ ($\text{Ln} = \text{Pr}, \text{Nd}, \text{Tb}, \text{Dy}, \text{Ho}, \text{Tm}, \text{Yb}$ and Lu) manganites, are presented, following a description of sample preparation by solid state reaction. The magnetic susceptibility, measured up to 530 K for our samples, presents a broad peak at high temperatures corresponding to the onset of the CO (T_{CO}). From these results we define the nature of the magnetic correlations above and below this temperature in the framework of the Zener polarons model, as proposed by Daoud-Aladine [10]. In this chapter we also present the details of the nuclear and magnetic structure for all samples versus temperature. All our samples present a pseudo-CE magnetic configuration at the lowest temperatures, corresponding to a CE-type ground state with canting. The distortions due to the doping and the effect of the ionic radius of the cations are analysed.

In chapter four we describe the ab-initio methods using the density functional theory (DFT) that have been used to model the $\text{Ln}_{0.50}\text{Ca}_{0.50}\text{MnO}_3$ series. The characteristics of these materials are derived from the results obtained by solving the Schrodinger equation for the electrons of the system under study. We present DFT and we discuss the most important features (spin polarisation), approximations (pseudo-potentials and exchange-correlation functional) and (Hubbard) corrections in these methods in their application to half-doped manganites. We include a brief presentation of the code used for the DFT calculations, VASP, with the corresponding input files.

In chapter five, the results of simulations are reported and compared with the

experimental results. These calculations have been performed to confirm the experimental results and to access other significant quantities such as the electronic density of states. The calculations were performed with spin-polarised DFT, and, when needed, a Hubbard correction has been applied to take into account the strong electronic correlations in manganites. The computational approach has been tested on two pure systems, studied previously: CaMnO_3 and NdMnO_3 . Two, half-doped systems have been chosen for this study: $\text{Nd}_{0.50}\text{Ca}_{0.50}\text{MnO}_3$ and $\text{Lu}_{0.50}\text{Ca}_{0.50}\text{MnO}_3$. The first because the La and Pr compound were already studied [11, 12] so we continued the series with the Nd compound. We chose the second system because Lu has the smallest ionic radius in the lanthanides series, its 4f shell is full and Lu is therefore comparable with La. Finally the thesis ends with a general conclusion for this work and perspectives for future work.

Introduction

Les premières études sur les manganites ont commencé dès 1950 avec les travaux seminaux de Jonker et Van Santen [1], qui ont montré l'existence du ferromagnétisme dans les mélanges de cristaux $\text{LaMnO}_3\text{-CaMnO}_3$, $\text{LaMnO}_3\text{-SrMnO}_3$ etc... Les systèmes de formule générale $\text{Ln}_{0.5}\text{B}_{0.5}\text{MnO}_3$ (où Ln correspond aux atomes de lanthanide et B aux métal alcalin) montrent un comportement magnétique très important.

Jonker et Van Santen furent les premiers à cristalliser les manganites à valence mixte [1] (c'est-à-dire des matériaux de la forme $\text{Ln}_{0.5}\text{B}_{0.5}\text{MnO}_3$ où Ln représente une terre rare trivalente, habituellement lanthane, néodyme ou praséodyme et B est un métal alcalin bivalent comme calcium, strontium ou baryum). Ces composés ont été baptisés manganites bien que ce terme soit mal approprié dans la mesure où il devrait seulement s'appliquer aux composés contenant un manganèse tétravalent tel que $\text{MnO}(\text{OH})$. Leur étude a montré que les manganites cristallisent dans une structure de perovskite où chaque ion de manganèse est entouré par un octaèdre d'oxygènes.

Le site Ln de la structure de perovskite contient l'ion le plus grand. Le manganèse, quant à lui, est l'ion le plus petit ion du système. Jonker et Van Santen ont mesuré la température de Curie du $\text{La}_{1-x}\text{Ca}_x\text{MnO}_3$ en fonction du dopage x en calcium.

Il est intéressant de noter l'influence du paramètre x dans la composition. Dans le cas $(\text{La,Ca})\text{MnO}_3$, par exemple, le calcium est dans un état d'oxydation 2+, alors que le lanthane est 3+. Par conséquent, chaque fois qu'un ion de lanthane est remplacé par le calcium, un manganèse est contraint à l'état d'oxydation 4+ afin de préserver la neutralité de charge. En d'autres termes, l'introduction d'un calcium ôte un électron du manganèse, processus que les physiciens de la matière condensés appellent 'doping with holes'. L'atome Ln est un ion trivalent, B est un ion bivalent à la fois terre rare et métal alcalin, l'oxygène en O^{2-} , et la fraction relative de Mn^{+3} et Mn^{+4} est réglée par pourcentage de composition x.

La structure idéale d'un perovskite est cubique: les charge des cations de terres

rare occupent les sommets de la maille élémentaire et le cation de manganèse, situé en son centre, est coordonné de manière octaédrique avec les oxygènes comme illustré dans la figure 1, par Wollan [2] et Koehler [3].

Ces mêmes auteurs ont également décrit l'état d'ordre de charge à $x = 0.50$ comme l'état de type CE [3] correspondant au mélange du type C- et E de la maille élémentaire magnétique. Il y a sept type d'arrangements possibles pour le spin des atomes du manganèse dans la maille élémentaire (A, B, C, D, E, F, et G), comme illustré dans la figure 2 [5].

Le manganèse, avec ses cinq orbitales 3d et deux électrons 4s, est un métal de transition. En tant que tel, il est de valence variable et peut former des composés stables avec différents états d'oxydation. L'antiferromagnétisme est une forme d'ordre magnétique où les moments locaux (comme celui provoqué dans les ions de manganèse en alignant les électrons dans couche d vide) peuvent être divisés en deux sous-mailles équivalentes.

Jusqu'en 1949, les seules méthodes disponibles pour détecter l'antiferromagnétisme étaient basées sur des mesures indirectes telles que l'anomalie de susceptibilité ou de chaleur spécifique. La situation a changé lorsqu'il est venu à l'esprit de J. Samuel Smart que les expériences de diffraction de neutrons pourraient fournir des moyens directs de détecter l'antiferromagnétisme [6]. Peu d'années après les études de Jonker et Van Santen, Wollan et Koehler ont employé la diffusion de neutrons pour étudier la structure de spin des manganites [3]. Non seulement ils ont observé l'antiferromagnétisme prévu du MnO, mais ils ont également découvert quelques arrangements possibles de spin en fonction de x , tel que les ordres magnétiques de types A, C et G (cf schéma 2).

Dans un article paru juste après Wollan et Koehler, John Goodenough [5] propose alors une théorie attribuant cette variété de structures à la covalence. De manière surprenante, ce travail n'a suscité que peu d'attention de la part de la communauté expérimentale. De leur côté, les études théoriques se sont poursuivies. Toutes ces études théoriques, qui seront décrites plus tard, ont souffert de la même limitation : les états électroniques considérés ont toujours été considérés comme étant uniformes.

L'intérêt expérimental n'a été finalement établi qu'en 1989 avec l'observation d'un effet de magnétorésistance géante (MR) dans les composés de $\text{Nd}_{0.5}\text{Pb}_{0.5}\text{MnO}_3$ par Kusters et al. [7] et de $\text{La}_{2/3}\text{Ba}_{1/3}\text{MnO}_3$ par von Helmlot et al. [8]. Searle et Wang avaient déjà rapporté l'effet de magnétorésistance géante dans les monocristaux de $\text{Pr}_{1-x}\text{Ca}_x\text{MnO}_3$ dès 1969 [9]. L'effet de magnétorésistance peut être décrit

de manière succincte comme le changement de comportement de transport sous l'application d'un champ magnétique. Par exemple, le composé $\text{Pr}_{0.7}\text{Ca}_{0.3}\text{MnO}_3$ est un isolant en l'absence de champ magnétique mais celui-ci devient un conducteur à basse température en présence d'un champ de un Tesla.

Une caractéristique intéressante avec les manganites est la phénoménologie qu'implique les orbitales de l'atome de manganèse. Dans un réseau cubique, les orbitales 3d d'un atome isolé ou d'ion sont dégénérées en trois niveaux de basse énergie (d_{xy} , d_{xz} , et d_{yz}), habituellement désignés sous le nom de t_{2g} une fois hybridées aux orbitales des atomes d'oxygène environnants et deux niveaux de plus haute énergie ($d_{x^2-y^2}$) et (d_{z^2}) appelés e_g . Dans ce contexte, la valence des ions manganèse est de quatre (Mn^{3+}) ou de trois (Mn^{4+}), et leur fraction relative est dictée par le dopage chimique. Dans les composés à faible largeur de bande, comme $\text{Pr}_{0.5}\text{Ca}_{0.5}\text{MnO}_3$ un état *d'ordre de charge* de (Mn^{3+}) et (Mn^{4+}) est stabilisé à proximité de $x = 0.5$.

La valeur particulière de $x = 0.5$ pour le dopage produit des effets intéressants au niveau de la structure orthorhombic dus à l'atome de manganèse. En effet, le rôle joué par les électrons de valence de $\text{Ca}^{2+}/\text{Ln}^{3+}$ sur les électrons de valence du manganèse ($\text{Mn}^{3+}/\text{Mn}^{4+}$) est crucial pour la compréhension des propriétés des manganites semi-dopés. Le but de ce travail était de réaliser une étude systématique de la structure électronique et magnétique de la famille des manganites semi-dopés du Ca: $\text{Ln}_{0.50}\text{Ca}_{0.50}\text{MnO}_3$ ($\text{Ln} =$ terre rare). Nous avons particulièrement focalisé notre attention sur l'ordre de charge et l'ordre orbital généralement présents à cette composition. Nous avons dérivé un modèle microscopique de structure nucléaire et magnétique à partir de techniques de diffraction neutronique sur les poudres et de calculs ab-initio afin de comparer les résultats expérimentaux et les modèles numériques et comprendre ainsi le rôle de l'inhomogénéité chimique et magnétique dans ces systèmes.

La modification de l'état de spin électronique et du métal de transition par le dopage correspond à une modification structurale de la géométrie du polyèdre de coordination des atomes autour du métal de transition. Ceci induit des modifications structurales coopératives observables par diffraction de neutrons. En contraste avec l'ordre induit par le dopage chimique, un désordre chimique intrinsèque est associé à l'élément de dopage sur le site A du perovskite (formule générale ABO_3) où sont placés les ions trivalents (RE^{3+}) et bivalents (Ca^{2+}). Ce désordre est dû à la différence de rayon ionique et d'affinité chimique entre ces ions. Afin d'étudier

systematiquement l'effet de la substitution au niveau du site A et la relation entre les propriétés structurales et magnétiques) et les propriétés magnétiques macroscopiques, plusieurs échantillons (spécifiés auparavant) ont été synthétisés et caractérisés par des mesures magnétiques macroscopiques. Les résultats de diffraction de neutrons sont une étape fondamentale vers la compréhension de la relation entre les propriétés structurales et macroscopiques et représentent de fait une source de motivation pour l'étude de la structure magnétique et des phénomènes de CO/OO par des simulations ab-initio.

Dans le premier chapitre de cette thèse, suite à la description du diagramme de phase des manganites les plus étudiés ($\text{La}_{1-x}\text{Ca}_x\text{MnO}_3$), leurs propriétés physiques, les concepts de base et les modèles les plus importants tels que l'effet Jahn-Teller, l'interaction de super-échange, le double-échange et le modèle de Zener seront introduits.

Dans le deuxième chapitre, une brève introduction à toutes les techniques expérimentales utilisées dans cette étude sera présentée. Les propriétés magnétiques macroscopiques ont été mesurées en fonction de la température à l'aide d'un SQUID qui sera également décrit au cours de ce chapitre. La technique microscopique principale utilisée pour cette thèse a été la diffraction neutronique sur poudre. Celle-ci, ainsi que les instruments utilisés à l'institut Laue Langevin à Grenoble, D20 et D1A, seront décrits ainsi que la méthode de Rietveld utilisée pour affiner les données expérimentales et en extraire les informations structurales sous-jacentes.

Dans le troisième chapitre, les résultats expérimentaux correspondant à l'étude systématique sur les échantillons de manganites de $\text{Ln}_{0.50}\text{Ca}_{0.50}\text{MnO}_3$ ($\text{Ln} = \text{P.R.}, \text{ND}, \text{TB}, \text{Dy}, \text{Ho}, \text{TM}, \text{Yb}$ et Lu), seront présentés suite à une description de leur préparation par réaction à l'état solide. La susceptibilité magnétique mesurée jusqu'à 530 K présente un pic large à températures élevées correspondant à la températures d'ordre de charge (T_{CO}). A partir de ces résultats, nous définissons la nature des corrélations magnétiques au-dessus et en-dessous de cette température dans le cadre du modèle des polarons de Zener comme proposé par Daoud-Aladine [10]. Nous présenterons également dans ce chapitre les détails de la structure nucléaire et magnétique pour tous les échantillons en fonction de la température. Tous nos échantillons présentent une configuration magnétique de type pseudo-CE à la plus basse température correspondant à un état fondamental de type CE avec un effet de canting. Les déformations dues au dopage et à l'effet du rayon ionique seront également analysées.

Dans le quatrième chapitre, nous décrivons les calculs ab-initio réalisés à l'aide de la théorie de la DFT pour modéliser la série des $\text{Ln}_{0.50}\text{Ca}_{0.50}\text{MnO}_3$. Les caractéristiques de ces matériaux sont obtenues à partir de la résolution de l'équation de Schrodinger pour les électrons du système. La théorie de la DFT sera présentée ainsi qu'une discussion sur l'interprétation de l'énergie d'échange-corrélation et des approximations nécessaires à son évaluation. A cet effet, le programme VASP, utilisé pour les calculs, sera présenté ainsi que ses différents fichiers d'entrée et de sortie.

Dans le cinquième chapitre, les résultats des simulations seront décrits et comparés aux résultats expérimentaux. En effet, ces calculs ont été effectués pour confirmer les résultats expérimentaux mais également pour accéder à d'autres quantités significatives comme la densité d'états électroniques. Les simulations ont été effectuées avec la DFT spin-polarisée, la fonctionnelle d'échange-corrélation GGA-PBE, et, quand nécessaire, avec une correction d'Hubbard dans l'approche GGA+U, pour prendre en considération la corrélation électronique forte dans les manganites. Nous avons choisi comme système deux manganites purs: CaMnO_3 et NdMnO_3 , ayant déjà fait l'objet d'études précédentes [13, 11], afin de valider notre protocole de simulation. Deux systèmes semi-dopés – $\text{Nd}_{0.5}\text{Ca}_{0.5}\text{MnO}_3$ et $\text{Lu}_{0.5}\text{Ca}_{0.5}\text{MnO}_3$ – ont ensuite été considérés. Nous avons choisi ces systèmes pour deux raisons: (i) les composés semi-dopés contenant le La et le Pr ont déjà fait l'objet de travaux antérieurs [11, 12], et il nous a donc semblé naturel de poursuivre la série de lanthanide avec le système Nd-Ca; (ii) nous avons choisi les composés de LuCa parce que le Lu, à l'instar de La, est saturé au niveau de ses orbitales 4f et qu'il présente de surcroît le plus petit rayon ionique dans la série de lanthanides. Enfin, le chapitre final est consacré à une conclusions générale et aux perspectives possibles à ce travail.

1 Propriétés physiques des manganites

$\text{Ln}_{1-x}\text{Ca}_x\text{MnO}_3$ est un membre de la famille des perovskites dont la formule chimique générale est ABO_3 . Les ions de manganèse occupent le site B, comme dans la figure 1.1 au centre de la maille et sont coordonnés de manière octaédrique par les ions de l'oxygène qui occupent les sommets de l'octaèdre. Les ions Ln^{3+} et Ca^{2+} sont répartis sur les sites A dans le cristal. Une maille cubique est montrée dans la figure 1.1.

La structure cubique est observée seulement à température élevée, au-dessus de ≈ 1000 K, là où la plupart des perovskites sont cubiques. Pour des températures plus basses, les MnO_6 octaédriques se déforment par torsion autour des liaisons avec les oxygènes, réduisant de ce fait la symétrie du système de $\text{Ln}_{1-x}\text{Ca}_x\text{MnO}_3$.

La structure des manganites dopés aux pérovskites, et les propriétés intéressantes qu'il en résulte, a fait l'objet d'études dès 1950.

En effet, Jonker et Van Santen [14, 1] ont présenté les premiers travaux sur les composés $\text{La}_{1-x}\text{B}_x\text{MnO}_3$ avec $\text{B}=\text{Ca}$, Sr et Ba , constatant que pour les valeurs de x extrêmes ($x=0$ et à $x=1$), les composés devenaient des isolants antiferromagnétiques.

Dans ce chapitre, nous montrerons le diagramme de phase des composés La-Ca et Pr-Ca, en fonction du pourcentage de l'élément dopant, Ca, et de la température, ainsi que leurs propriétés structurales, électroniques et magnétiques: l'effet Jahn-Teller, structure électronique de l'orbital d-Mn, les mécanismes de double-échange, super-échange et le modèle de Zener.

1

Physical properties of manganites

$\text{Ln}_{1-x}\text{Ca}_x\text{MnO}_3$ is a member of the perovskite family which has the general chemical formula ABO_3 . The Mn ions occupy the B-site, as in figure 1.1 at the center of the unit cell and are octahedrally coordinated by the oxygen ions.

Adjacent MnO_6 octahedra are linked at their vertices. The Ln^{3+} and Ca^{2+} ions are

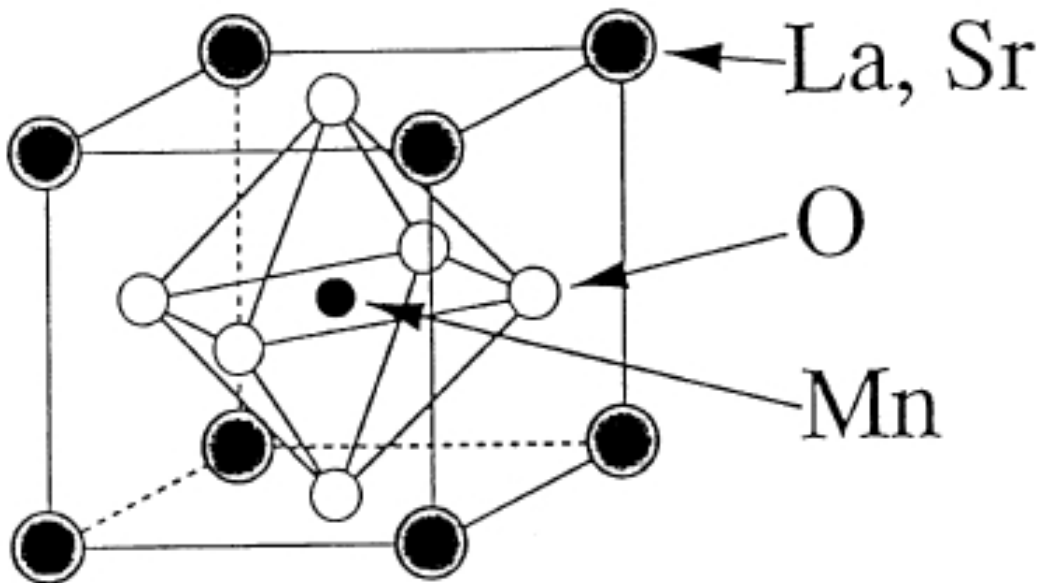


Figure 1.1: Typical perovskite structures of manganites [4]

then distributed randomly over the A-sites in the crystal. A cubic unit cell is shown in Fig. 1.1.

This cubic structure is observed only at high temperature, above ≈ 1000 K, where most perovskites are cubic. As the temperature is lowered, the MnO_6 octahedra distort and rotate around the oxygen links, thereby reducing the symmetry of the $\text{Ln}_{1-x}\text{Ca}_x\text{MnO}_3$ system.

Jonker and Van Santen [14, 1] carried out early work on the compounds $\text{La}_{1-x}\text{B}_x\text{MnO}_3$ with B = Ca, Sr and Ba. They found that the end members of the series, corresponding to $x=0$ and $x=1$, were antiferromagnetic insulators.

1.1 Phase diagram

In order to understand the structural, electronic and magnetic properties, we need to introduce the phase diagram of lanthanide manganites. The most studied system is $\text{La}_{1-x}\text{Ca}_x\text{MnO}_3$.

In order to have an idea of the reasons that pushed us to study the half-doped compounds, we described in details this complex phase diagram.

Figure 1.2 shows a phase diagram as a function of x and temperature for a bulk

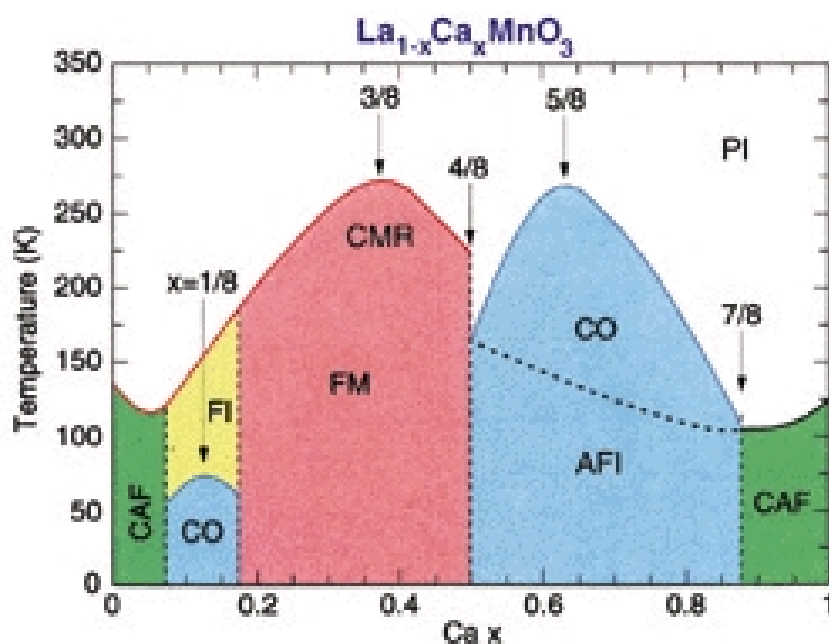


Figure 1.2: $\text{La}_{1-x}\text{Ca}_x\text{MnO}_3$ phase diagram for polycrystalline samples reproduced from Tomioka et al. [15].

of $\text{La}_{1-x}\text{Ca}_x\text{MnO}_3$, and the characteristic regions that we will explain below. The diagram shown in Figure 1.2 refers to the bulk polycrystalline material.

Figure 1.2 also presents an idealised picture by depicting the phase boundaries as sharp lines and omitting any coexistence regions. From just considering the symmetry requirements of each phase, there is no reason why both the ferromagnetic and charge-ordered phases cannot coexist in equilibrium. This was observed in 2000 by Levy et al. in the bulk polycrystalline of $\text{La}_{1-x}\text{Ca}_x\text{MnO}_3$ with varying grain sizes [16].

Then in 2002, Loudon, Mathur and Midgley reported a phase that was both ferromagnetic and charge-ordered in a bulk sample of $\text{La}_{0.50}\text{Ca}_{0.50}\text{MnO}_3$ at 90 K, which added further complexity to the $x = 0.5$ low-temperature boundary [17].

As the level of calcium doping x is increased a wide variety of electronic and magnetic phases is encountered, and these are summarised in this chapter. By the state of art, we will show the physical characteristics as a function of x -doping of alkaline metal 'Ca', in particular for $x = 0.5$, and the temperature. Therefore, starting with $x = 0$ with the LaMnO_3 up to $x = 1$ with CaMnO_3 .

In LaMnO_3 ($x = 0$) there are four 3d electrons on every manganese ion. The hopping of the itinerant e_g electron is restricted by the on-site Coulomb repulsion and the strong Hund coupling. The e_g electrons interact with each other by virtual hopping onto neighboring atoms when their spins are antiparallel. This kind of interaction is known as super-exchange and it will be describe in the section 1.3.2; it leads to antiferromagnetic order and LaMnO_3 is therefore an antiferromagnetic insulator.

Wollan and Koehler found the antiferromagnet lattice was A-type [2], fig. 2, in which the spins are ferromagnetically aligned within each ab-plane and long z-planes are coupled antiferromagnetically. When x is different to zero, the magnetic moment increases slightly.

In the range $0.1 < x \lesssim 0.2$, two transitions are observed on cooling.

The first transition, at about $130 \div 170$ K, is into a ferromagnetic insulating state. The fact that it is insulating means that the ferromagnetism is condensed by superexchange interaction, where the exchange interaction between non-neighboring magnetic ions is mediated by a non-magnetic ion, for example Mn-O-Mn in manganitic compounds.

The second transition, which occurs at 80 K, is ascribed to charge ordering (CO) [18]. However, CO does not necessarily means a magnetic transition and the anomaly at 80 K has also been linked to domain wall pinning effects [19].

X-ray measurements on single crystals have shown that, as x increases towards 0.2, the coherent Jahn-Teller distortions, originating from d-orbital ordering (OO), become suppressed and an orbitally disordered state is entered [20]. OO is not compatible with metallicity so the ferromagnetic insulating phase is bounded by the limit of coherent Jahn-Teller distortions. This limit occurs at lower levels of Ca-doping as the temperature is increased and therefore the phase boundary is not vertical on a plot of temperature versus calcium doping, but presents a certain zone of superposition.

For $0.2 \lesssim x < 0.5$, the low-temperature ground state in the bulk material is a ferromagnetic metal (FM).

If the crystal structure is close enough to the ideal cubic perovskite structure then the Mn-O-Mn bonds will be sufficiently linear. This leads to good orbital overlap and a high probability of hopping therefore the charge carriers become a delocalised electron gas. The distinction between Mn^{3+} and Mn^{4+} ions is lost, and the Jahn-Teller distortions are reduced, where the JT distortion is related to the bond lengths between manganese and oxygen atoms in the orthorhombic structure.

For the bulk material at $x=0.5$ two transitions are observed cooling down in the temperature. A FM state is initially entered at around 230 K. At lower temperatures, there is a transition to an antiferromagnetic state. The Néel temperature (T_N) is approximately 135 K on cooling and 185 K on warming [21]. Phase coexistence between FM and CO phases has been observed in a bulk samples of $\text{La}_{1-x}\text{Ca}_x\text{MnO}_3$ [16].

The low-temperature boundary between the FM and AFM phases is not sharp and there is a mixed-phase region around $x = 0.5$.

For the bulk material, values of x in the range $0.5 < x < 0.9$ give a charge-ordered insulator ground state at low-temperature. It was originally thought that in a CO state the Mn^{3+} and Mn^{4+} ions arranged themselves into two distinct sub-lattices and this resulted in a series of 'stripes' of the two types of ions [22]. The theory predicted a regular arrangement of Mn^{3+} and Mn^{4+} ions where the superlattice periodicity would be an integer multiple of the crystal lattice. Instead, there could be a small-amplitude charge density wave throughout the crystal.

There is an additional transition on further cooling down in temperature, in which the manganese spins align themselves in an anti-parallel arrangement to form an antiferromagnet. This occurs in the range 100÷150 K and the T_N depends on the level of Ca-doping. Neutron studies suggest that this phase is a CE-type, as show in Fig. 1.3 antiferromagnet with a checkerboard arrangement of spins [2].

It is possible to have the charge ordered phase by applying an external magnetic field. That is the case of another system: $\text{Pr}_{1-x}\text{Ca}_x\text{MnO}_3$, in fact a 25 T field was required to melt fully the charge-ordered state present in this system and induce metallic behavior [23].

In addition, the $\text{Pr}_{1-x}\text{Ca}_x\text{MnO}_3$ presents a very small bandwidth of e_g sublevel as compared to other compounds that have a behavior more in line with the standard

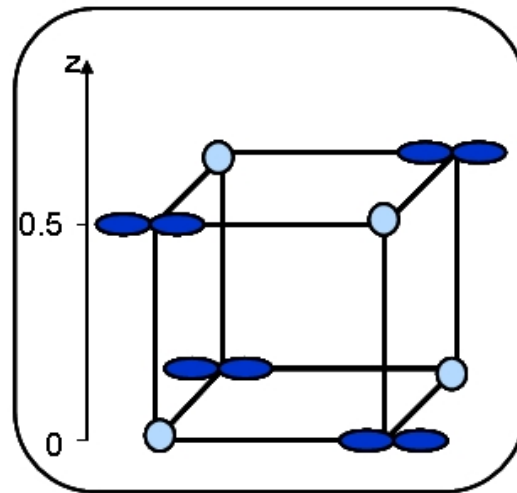


Figure 1.3: The charge and orbital ordering configurations for $\text{Ln}_{1-x}\text{Ca}_x\text{MnO}_3$, $x = 0.5$. Circles are Mn^{+4} and the lobes show the orbital ordering of the e_g -electrons of Mn^{+3} .

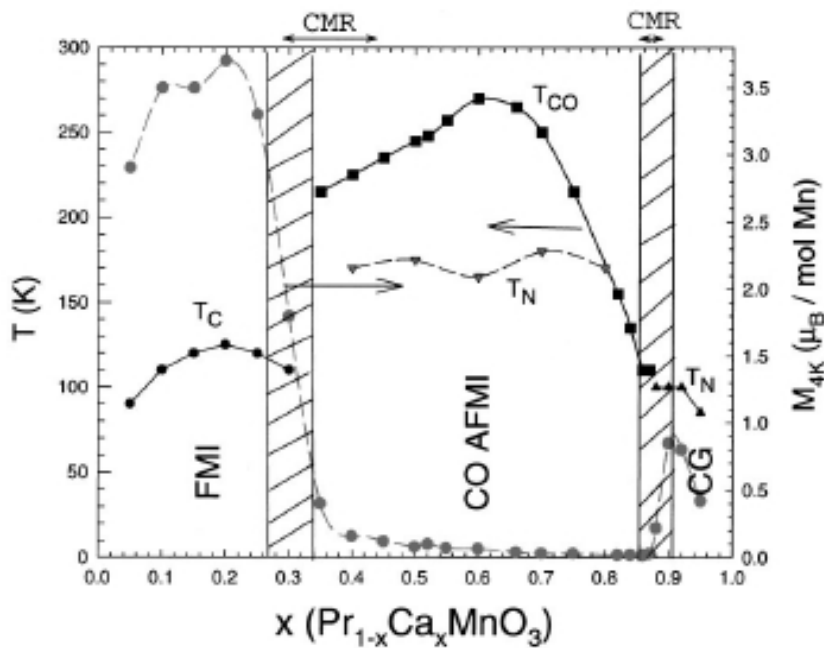


Figure 1.4: Phase diagrams of $\text{Pr}_{1-x}\text{Ca}_x\text{MnO}_3$ reproduced by C. Martin et al. [24]

double-exchange ideas. The bandwidth W [25] of e_g sublevel in the d-Mn orbitals

can be described empirically by the following equation:

$$W \propto \frac{\cos(\pi - \omega)}{d_{Mn-O}^{3.5}} \quad (1.1)$$

where ω is the Mn-O-Mn angle and d_{Mn-O} is the bond length between Mn and O atoms. In the low-bandwidth compounds, for example $\text{Pr}_{1-x}\text{Ca}_x\text{MnO}_3$, a charge-order state is stabilized in the vicinity of $x = 0.5$.

A particularly stable CO-state, for $\text{Pr}_{1-x}\text{Ca}_x\text{MnO}_3$, is found in a wide region between $x = 0.3$ and $x = 0.75$, as Jirak et al. [26] showed in Fig. 1.4. Note that a metallic ferromagnetic phase is not stabilized at zero magnetic field and ambient pressure in this low-bandwidth compound. This ferromagnetic state has not been fully explored to the best of our knowledge, and it may itself present charge ordering as some recent theoretical studies have suggested [27].

Neutron diffraction studies [26] showed that at all densities between 0.30 and 0.75, the arrangement of charge/spin/orbital order of this state is similar to the CE-state.

In the end-part of phase diagram, we have the CaMnO_3 ($x=1$) system; it is an antiferromagnetic insulator.

Wollan and Koehler found that the CaMnO_3 was a G-type antiferromagnet [2], (Fig. 2) in which every spin is antiparallel to its nearest neighbors. There is uncertainty as to whether there is phase separation or canted spins for values of x just below 1. Note that all the manganese ions at $x = 1$ are Mn^{4+} and, as such, there will be no Jahn-Teller distortions.

1.2 Rare earth manganites

The crystal lattice of most Ln-manganites is perovskite-like and nearly cubic (Fig. 1.1); the orthorhombic structure is inside the perovskite cubic. Rhombohedral, orthorhombic or other lattice distortions result either from tilting or from stretching (Jahn-Teller distortion) of the oxygen octahedral around the Mn ions. The distortions appear both for structural (ionic radii mismatch) and electronic (Jahn-Teller effect of Mn^{3+} and Mn^{4+}) reasons. In general, chemical substitution in LaMnO_3 is possible at all lattice sites. La^{3+} can be replaced, in general, by the rare earth elements, Y and Bi, as well as by divalent (Sr, Ca, Ba, Pb) alkaline metals, tetravalent (Ce, Te, Sn) and monovalent (K, Na) elements. Non-trivalent substitutions act as dopants: they induce a mixed Mn valence and, thereby, charge

carriers.

The size mismatch of the ions substituted into the perovskite lattice (the so-called chemical pressure effect) causes a reduction of the Mn-O-Mn bond angles from 180° down to 160° and below. The Mn-O-Mn angle is linked to the conduction bandwidth (W), that is reduced due to the smaller orbital overlap between Mn and O ions.

Most manganites, with general formula ABO_3 have a tolerance factor $t < 1$, defined in eq.(1.2), i.e. the ions of the A site are too small. With increasing $r(A)$, one observes both an increasing average bond angle (enhanced W) and also an increasing bond length (reduced W, for a range of larger r_A [28]. The Goldschmidt tolerance factor [29] calculated from ionic radii for any ABO_3 perovskite lattice, is:

$$t = \frac{(r_A + r_O)}{\sqrt{2}(r_{Mn} + r_O)} \quad (1.2)$$

where r_A, r_{Mn}, r_O are the average ionic radius of the lanthanide site, Mn - and O - atoms respectively; a value of $t = 1$ is characteristic of the cubic structure. Distorted perovskite-like lattices exist approximately in the range of $0.89 < t < 1.02$. Most manganites represent the case $t < 1$, it means the ions on the A site are too small for a cubic lattice.

1.3 Electronic structure and magnetic exchange

In order to explain the different interactions involving Mn ions it is useful to visualize the scheme in figure 1.5. The Mn^{3+} and Mn^{4+} valence states of Mn found in manganites have 4 or 3 electrons in the 3d level, respectively. All 3d electrons have parallel spins according to Hund's first rule. The Hund's rule coupling energy U_H is particularly large for Mn, about 2 eV [30]. The three lower-lying t_{2g} levels resulting from the crystal field splitting in the octahedral oxygen environment form a core magnetic moment of $3 \mu_B$. These t_{2g} electrons are always localized in the manganites.

The remaining electron, in the case of Mn^{3+} , occupies the e_g level and it can be delocalised or localized ($NdMnO_3$) depending on the case. Delocalization occurs via hybridization with the intermediate O - 2p orbitals and is most pronounced for Mn-O-Mn bond angles of 180° (i.e. in the cubic structure). Due to their parallel coupling to the Mn core moments, electrons moving with conserved

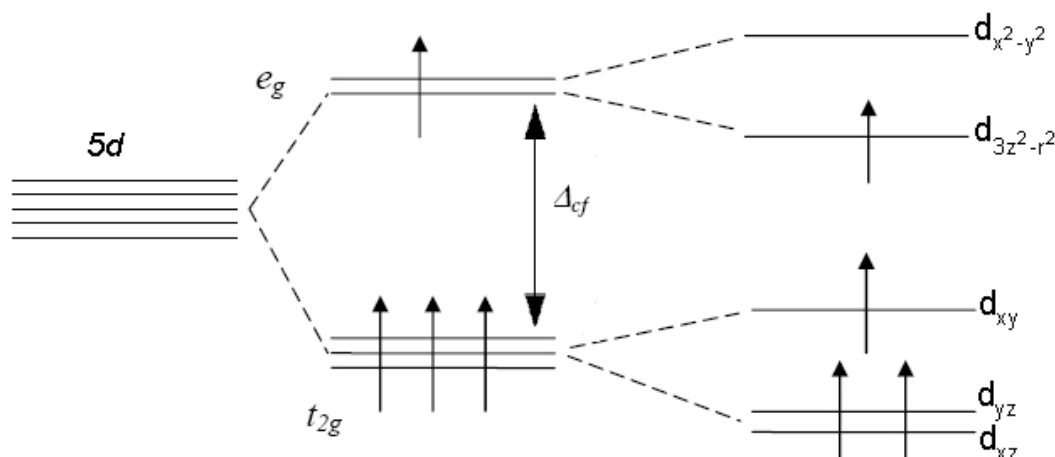


Figure 1.5: Field splitting of the five-fold degenerate atomic 5d levels into lower t_{2g} and higher e_g levels.

spin are the origin of a ferromagnetic exchange interaction. Zener introduced the concept of the ferromagnetic double exchange [31, 32] for manganites, assuming two simultaneous electron transfers: one electron from Mn^{3+} to a neighboring O - 2p orbital, and a second electron from this O - 2p orbital to an adjacent Mn^{4+} ion. Final and initial state of this process are degenerate and, thus, coexist and couple the two Mn core moments ferromagnetically. More generally, double exchange means a magnetic interaction mediated by itinerant spin polarized d-electrons which couple according to Hund's rule to localized magnetic moments [33]. Itinerancy of electrons is energetically favorable for the gain of kinetic energy.

1.3.1 Jahn-Teller effect

A typical definition of the Jahn-Teller (JT) effect is that for any non-linear molecule in a degenerate electronic state, there exists a displacement of the nuclei along at least one non-totally symmetric normal coordinate, that gives rise to a distortion of the molecular geometry with a concomitant lowering of the energy.

Two possible distortions of the cubic phase are associated with the Jahn-Teller effect. In the orthorhombic distortion there are in-plane bonds that can be one longer and one shorter. In the tetragonal distortion there are in-plane bond lengths shortening and the out-of-plane bonds extending, or vice versa [34, 35]. The main result of both distortions is that the Mn-O distances become different from one

another, (Fig. 1.6), and the degeneracy of the t_{2g} and e_g levels is lifted.

In the figure 1.6 the orthorhombic distortion is shown. For LaMnO_3 , the orbital splitting is such that z^2 -like orbitals are occupied, alternatingly oriented along the $x+z$ and $x-z$ axis [5, 36], yielding the orthorhombic distortion. The O_z fractional co-ordinate and this orthorhombic distortion are intimately related. For a tetragonal distortion, only the ratio between the b lattice parameter and the a and c parameter has to change.

The strong Jahn-Teller effect of Mn^{3+} is another important microscopic

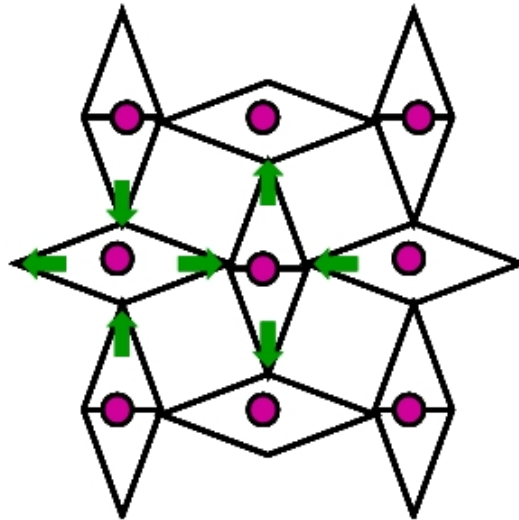


Figure 1.6: Sketch of the Q2 JT distortion in the ab plane, obeying $Pbnm$ symmetry. Mn atoms are represented by the circles. Closed arrows indicate the movement associated with the JT distortion.

mechanism of 'manganites' physics [37]. Elongation of the O-octahedron favors the occupation of the elongated e_g $d_{3z^2-r^2}$ orbital, while compression favors the square e_g $d_{x^2-y^2}$ orbital. The JT splitting energy is about $\Delta_{JT} = 1 - 1.5$ eV [38]. As a first consequence, moving e_g electron the 'trapping' (localization) of charge carriers by the elastic distortions may occur.

For the manganites, the JT distortion is dynamic, resulting in an average distortion of all O_6 octahedra. On the other hand, Jahn-Teller deformations of O_6 octahedra can be long-range ordered (OO), as found in LaMnO_3 . In the case of OO, two or three distinct Mn-O bond lengths are detectable experimentally [28], and the crystal structure is of lower symmetry (orthorhombic, monoclinic).

In manganites, superstructures of the localized charge carriers (CO) usually accompany OO even though the idea of integer charge patterns of $\text{Mn}^{3+}/\text{Mn}^{4+}$ has

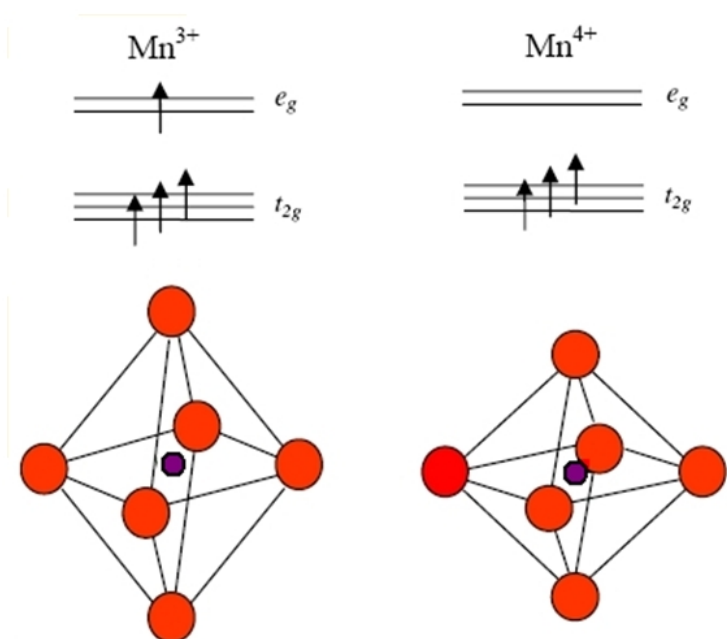


Figure 1.7: Field splitting of Mn-5d orbital, t_{2g} and e_g , in particular Jahn-Teller distortion shown in the figure further lifts each degeneracy.

been questioned [39, 40].

The magnetic and electronic properties in these compounds have traditionally been examined with the double exchange (DE) model (and JT effect), which considers the transfer of an electron between neighboring Mn³⁺ and Mn⁴⁺ ions through the Mn-O-Mn path [41, 42]. The electron transfer depends on the relative alignment of the electron spin and localized Mn⁴⁺ spin. When the two spins are aligned, the carrier avoids the strong on-site Hund exchange energy and hops easily. Thus the DE model provides an explanation for a strong coupling between the charge carriers and the localized manganese moments. The strong electron-phonon coupling is expected because the electronic ground state of the Mn³⁺ ions is degenerate, and this degeneracy is removed by a spontaneous distortion of the surrounding lattice, known as the Jahn-Teller (JT) effect [43].

For the whole class of manganites under study, polaron-like transport behavior of Mn-O distance observed for $T > T_C$ (e.g. $\text{La}_{0.7}\text{Ca}_{0.3}\text{MnO}_3$, [44, 45]) indicated that polarons are the predominant high-temperature type of charge carriers in manganites. While earlier work proposed magnetic polarons, i.e. a magnetic polarization of the Mn spins surrounding a moving electron [42], elastic lattice polarons originating from the JT effect of Mn³⁺ ions were recognized as essential

mechanism later [37, 44]. For localized e_g electrons, the Jahn-Teller distortions of oxygen octahedra around Mn^{3+} are static and typically collective (orbital order). These distortions become dynamic when e_g electrons move. Then, charge carriers might be trapped by the local lattice distortion they produce, forming localized lattice polarons.

1.3.2 Superexchange interaction

The exchange interaction is normally very short-ranged so that the longer-ranged that is operating in the case of manganites must be in same sense 'super'. The exchange mechanism which is operative here is in fact known as 'superexchange' (Fig. 1.8). It can be defined as an indirect exchange interaction between non-neighboring magnetic ions which are mediated by a non-magnetic ion which is placed between them.

The superexchange interactions via 2p-orbitals of oxygen are present, which involve both Mn t_{2g} and e_g orbitals; they have been analysed by Goodenough [5]. The superexchange can be ferromagnetic or antiferromagnetic. For instance in the case of $Mn^{3+}(e_g)$ - O - $Mn^{4+}(e_g)$, it depends on the orientation of the $Mn^{3+}(e_g)$ orbital.

One prominent example is $LaMnO_3$ that contains only Mn^{3+} ions. The $LaMnO_3$ has an A-type antiferromagnetic structure (see figure 2) where ferromagnetic Mn^{3+} - O - Mn^{3+} superexchange dominates within parallel lattice planes and produces a well-defined ordering of the orientation of the occupied e_g orbitals, with neighboring planes coupled antiferromagnetically.

1.3.3 Double exchange and Zener model

Most of the early theoretical work on manganites focused on the qualitative aspects of the experimentally discovered relation between transport and magnetic properties, namely the increase in conductivity upon the polarization of the spins [13, 11, 46, 47].

The states of manganites were assumed to be uniform, i.e. the formation of coexisting clusters of competing phases does not included in the these considerations. The 'double exchange' (DE) was proposed by Zener [32] as a way to allow for charge to move in manganites by the generation of a spin polarized state. The DE process has been historically explained in two somewhat different ways.

Originally, Zener considered the explicit movement of electrons schematically

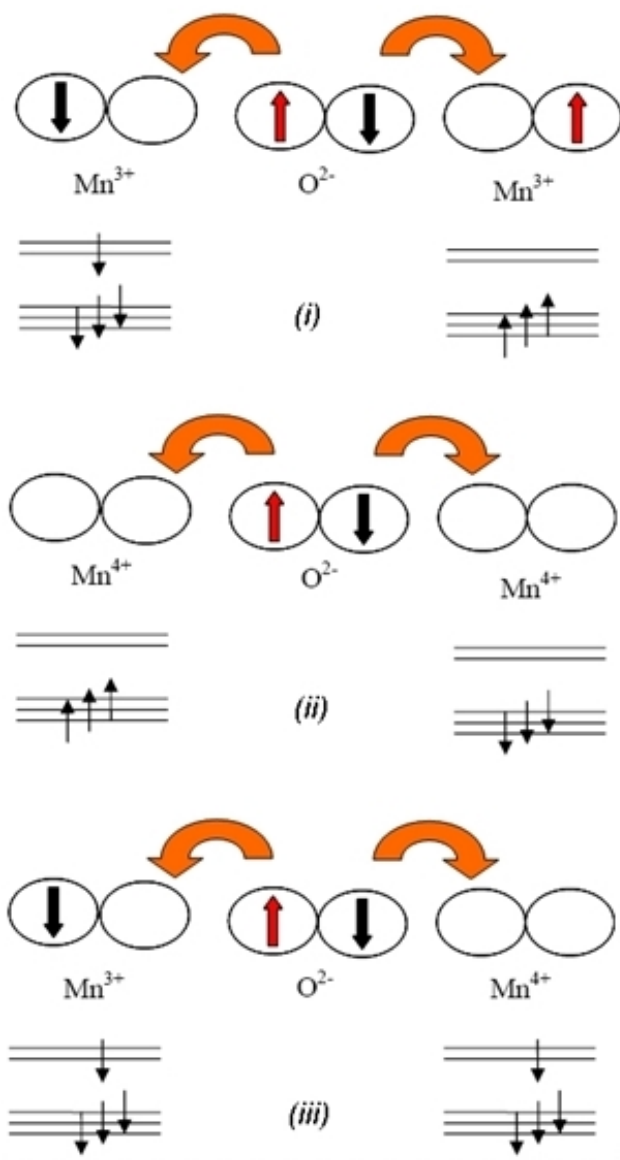
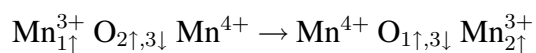


Figure 1.8: Superexchange interaction between manganese and oxygen atoms. The three panels result in an (i) antiferromagnetic, (ii) antiferromagnetic and (iii) ferromagnetic arrangement of the core manganese spins respectively.

written [48] as:



where 1, 2, and 3 label electrons that belong either to the oxygen between manganese, or to the e_g -level of the Mn-ions. In this process there are two

simultaneous motions (thus the name DE) involving electron 2 moving from the oxygen to the right Mn-ion, and electron 1 from the left Mn-ion to the oxygen (see figure 1.9).

The second way to visualize DE processes was presented in detail by Anderson

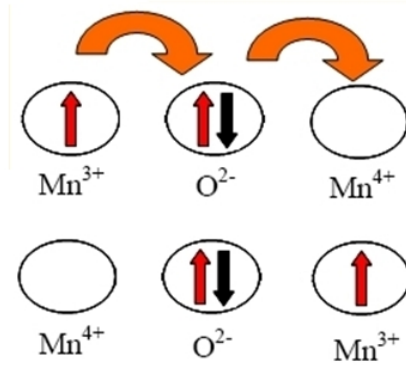


Figure 1.9: Draw of the double-exchange mechanism which involves two Mn ions and one O ion.

and Hasegawa [49] and it involves a second-order process in which the two states described above go from one to the other using an intermediate state $\text{Mn}_{1\uparrow}^{3+} \text{O}_{3\downarrow} \text{Mn}_{2\uparrow}^{3+}$. In this context the effective hopping for the electron to move from one Mn-site to the next is proportional to the square of the hopping involving the p-oxygen and d-manganese orbitals (t_{pd}). In addition, if the localized spins are considered classical and with an angle ϑ between nearest-neighbor ones, the effective hopping becomes proportional to $\cos(\vartheta/2)$, as shown by Anderson and Hasegawa [49].

If $\vartheta = 0$ the hopping is the largest, while if $\vartheta = \pi$, corresponding to an antiferromagnetic background, then the hopping cancels. The quantum version of this process has been described by Kubo et al. [50].

Note that the oxygen linking the Mn-ions is crucial to understand the origin of the word 'double' in this process. It is interesting to observe that ferromagnetic states appear in this context even without the oxygen. It is clear that the electrons simply need a polarized background decrease their kinetic energy. This tendency to optimize the kinetic energy is at work in a variety of models and the term double exchange appears unnecessary. However, in spite of this fact it has become customary to refer to virtually any ferromagnetic phase found in manganese models as 'DE induced' or 'DE generated', forgetting the historical origin of the term.

1.3.4 Magnetic and electronic properties in phase diagrams: conclusions

The essential contributions to the electronic energy in manganites have been outlined. To summarize, they are:

- (i) the kinetic energy of e_g electrons;
- (ii) the Hund on site magnetic coupling between e_g and t_{2g} electron spins;
- (iii) the coupling of e_g electrons and elastic distortions of MnO_6 octahedral (Jahn-Teller effect);
- (iv) the crystal field splitting energy in the octahedral coordination;
- (v) the Heisenberg magnetic coupling between nearest neighbour localized electron spins;
- and (vi) the Coulomb interaction among e_g electrons [33].

Dominance of one or the other mechanism results in a multitude of different ground states. With respect to the chemical composition, the ground state of $\text{Ln}_{1-x}\text{B}_x\text{MnO}_3$ depends on (i) the number of doped charge carriers x , (ii) the average ionic radii on Ln and Mn lattice sites and (iii) the distribution of ionic radii on Ln site measured by a disorder parameter σ that can be defined as the standard deviation of ionic radii [15].

Ground states observed for manganites include ferromagnetic metals (frequent), antiferromagnetic insulators (very frequent), ferromagnetic insulators (rare), antiferromagnetic metals (rare), glassy insulators, more complex canted magnetic structures and even mixed-phase states (see below) [51]. Almost all metallic manganites are ferromagnetic, since electron transfer caused by double exchange interaction.

In particular, the most studied system is $\text{La}_{1-x}\text{Ca}_x\text{MnO}_3$, but in this thesis we want to understand how the Ln influence the physics of the manganites. The Pr-Ca system has been studied quite extensively. In that case the quite different ionic radius r_A , leads an increased distortion of the orthorhombic structure respect to the La-Ca system, resulting in the suppression of the electron transfer.

General features of the phase diagrams of the Ln manganites are the appearance of a metallic ferromagnetic (FMM) phase around $x = 0.33$ in compounds like

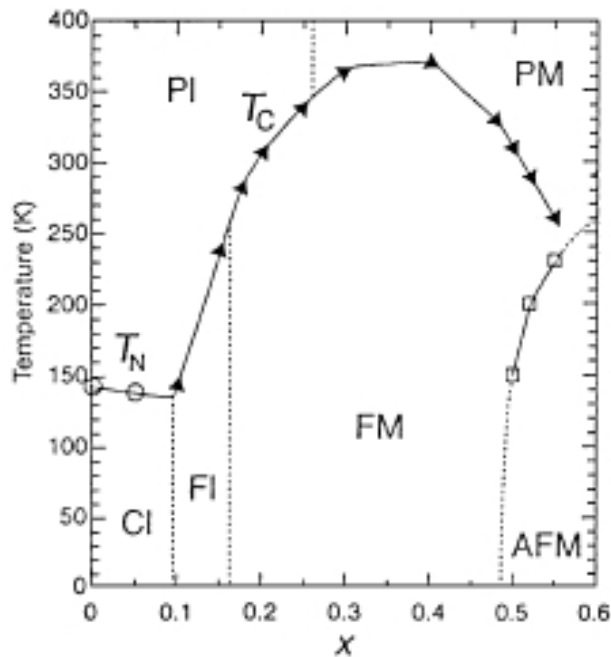


Figure 1.10: Phase diagram of $\text{La}_{1-x}\text{Sr}_x\text{MnO}_3$ (by Y. Tokura and Y. Tomioka) prepared with data from Urushibara et al. [52] and Fujishiro et al. [53].

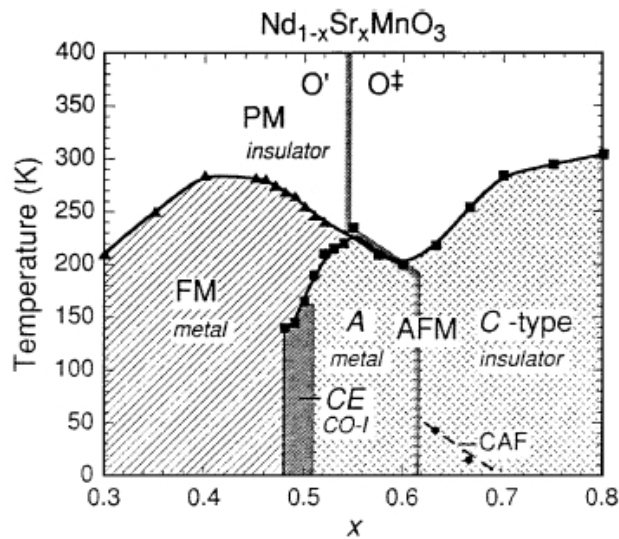


Figure 1.11: Phase diagram of $\text{Nd}_{1-x}\text{Sr}_x\text{MnO}_3$, reproduced from Kajimoto et al. [54].

$\text{La}_{1-x}\text{Sr}_x\text{MnO}_3$ (see figure 1.10) and completely absent for Pr-Ca compounds. This metal phase is interesting for applications in spintronics since it is characterized by

a high spin polarization of charge carriers.

Near $x \sim 0.5$, for the La-Sr compound, the ground state changes to antiferromagnetic insulating (AFI) and charge ordered (CO). At high temperatures, a paramagnetic (PM) and (almost always) insulating phase is found. Between these three fundamental phases (FMM, AFI-CO, PM) there are regions of more complex character. Originally, spin-canted magnetic structures have been proposed to exist between FMM and AFI phase regions, in particular for low doping [42].

Recent theoretical models indicate a coexistence of two phases with either different electron densities (electronic phase separation) or different structural distortions [33, 55].

Experimental evidence for mixed-phase states has been collected in many ways although an unambiguous interpretation of some of these experiments is still difficult. Exclusion of nano-scale chemical inhomogeneity as the origin of the phase separation is naturally complicated [56]. Surprisingly, the observed length scale of the extension of phase regions for phase-separated manganites varies from 1 nm to nearly 1 mm. A large extension excludes the different electronic density of the phases for reasons of electrostatic energy.

2 Approche expérimentale et méthodes

Dans ce chapitre, les principales techniques et méthodes utilisées au cours de ce travail sont présentées. Des mesures de susceptibilité à basse et haute températures ont été réalisées à l'aide d'un SQUID pour évaluer l'intensité des interactions magnétiques et la température d'ordre de charge T_{CO} .

La diffraction de neutrons à haute résolution a été utilisée pour déterminer les structures nucléaires et magnétiques en fonction de la température.

Des mesures de diffraction par neutrons sur nos échantillons ont été faites sur les instruments D20 et D1A (ILL). La méthode de Rietveld nous a permis d'affiner nos données afin d'en extraire les structures nucléaires et magnétiques. Pour cela, nous avons utilisé le programme FullProf Suite.

2

Experimental approach and methods

In this chapter the techniques and methods utilized in this thesis to characterize and study our systems are presented. Macroscopic measurements of susceptibility at high and low temperature were performed, using a SQUID, to have a first idea about the strength of the magnetic interactions and the temperature of the spin freezing occurring at low temperature. Neutron powder technique was used to investigate the crystal and magnetic structure, therefore the neutron diffraction technique and its implementations to refine crystal structure from powders will be presented.

2.1 Static magnetic properties: magnetization and uniform susceptibility

The focus of this work was to characterize samples of $\text{Ln}_{0.5}\text{Ca}_{0.5}\text{MnO}_3$, $\text{Nd}_{0.5}$ (Ln = Pr, Nd, Dy, Ho, Er, Tm, Yb and Lu) and studying their structural and magnetic features. In order to do this, it is of great aid to start from the susceptibility of these samples. Therefore, it is needed to understand the information derived from the susceptibility.

At high temperature, the magnetic susceptibility, i.e., the degree of magnetism of a material (χ_m) in a magnetic field, is dominated by the thermal contributions, and it increases slowly upon cooling, generally following a Curie-Weiss behavior, in the case of antiferromagnetic coupling.

If the temperature is lowered enough a maximum appears at T_N (the Néel point), below which the susceptibility decreases rapidly with temperature. This occurs because above T_N the thermal energy available to the system is sufficient to overcome the aligning forces due to the spin-spin interaction. At T_N there is a balance between these two effects, and below this critical temperature the anti-parallel spin coupling predominates and the magnetic susceptibility decreases. So at high temperature the magnetic system is paramagnetic following a Curie or Curie-Weiss behavior and only at low temperature one can observe the differences in susceptibility, depending on the kind of interactions between the spins.

In the case of antiferromagnetism it is generally accepted that the mechanism of the exchange interaction involves the mutual pairing of electronic spins via some form of orbital overlap. Two mechanisms of interaction are usually used to describe the AFM exchange: the direct interaction and the superexchange.

A first step to characterize a magnetic material is to measure its macroscopic susceptibility versus temperature. Low temperature behavior of the susceptibility provides information about the magnetic interactions involved (see figure 2.1) and about the presence of critical transition temperatures. It is often very interesting to investigate the temperature region where the energy of thermal fluctuations becomes small compared with the energy scale of the magnetic interactions (i.e. $\frac{J}{k_B T} \gg 1$).

The molar magnetic susceptibility χ_m of a sample, expressed in terms of electromagnetic units (emu) per mole, is given by:

$$\chi_m[\text{emu}] = \frac{m[\text{emu}]}{H[\text{G}]n[\text{mol}]} \quad (2.1)$$

The development of the Superconducting Quantum Interference Device (SQUID) technique, which is one of the most sensitive method for measuring the magnetisation, makes possible to determine the magnetisation in a very small applied field, in our case it was 550 G. We used a constant-field of 500 G in order to obtain dc-susceptibility (χ_{dc}). The measure of χ_{dc} is a good technique in the study of systems in which a freezing phenomenon occurs at a particular temperature T_f , as is the case of spin glasses.

Actually, there are two different ways to measure susceptibility in a small field. The first one is to apply the field far above T_f and cool the sample in the field down to $T \ll T_f$, recording simultaneously the magnetisation. This is called *field cooling* (FC). The second one is to cool the sample in zero field to $T \ll T_f$ and at this lowest temperature apply a constant field, and heat the sample while measuring M to $T \gg T_f$. This is called *zero field cooling* (ZFC).

For a spin glass at T_f the dc susceptibility become constant and its value quasi time independent, meaning that if we switch off the field we have to wait for a long time to observe a drift of the susceptibility for a given value of $T < T_f$. Moreover, the magnetisation in the FC process is reversible upon changing the temperature at constant field. The value of the ZFC at given T is less than the corresponding value in the FC process. In this case the process is irreversible and results $\chi_{ZFC}(T \rightarrow \infty) = \chi_{FC}$ at any $T > T_f$.

Shortly, the dc field (small), if applied below T_f creates a metastable state, so the T_f may be defined by the onset of these irreversibility, i.e., by the difference between FC and ZFC curves (see figure 2.1).

2.1.1 DC SQUID magnetometry

The SQUID is based on a circuit of superconducting material interrupted at two levels by very thin layers of an insulating material, which is called Josephson junction. A supercurrent flows through the SQUID, via the Josephson junctions. If a magnetic field is applied at one junction, the last one detects the phase of the supercurrent wavefunction tunneling through it. When the supercurrents are recombined they have a different phase and an interference results. An applied magnetic field changes the phase angle across the Josephson junction and creates an interference pattern very sensitive to the magnitude of the magnetic field in the junction coupled with the sample by the pickup coils.

The SQUID amplifier converts this pattern into an output voltage which is directly proportional to the applied magnetic field. The dc Squid used was the MPMS-5S

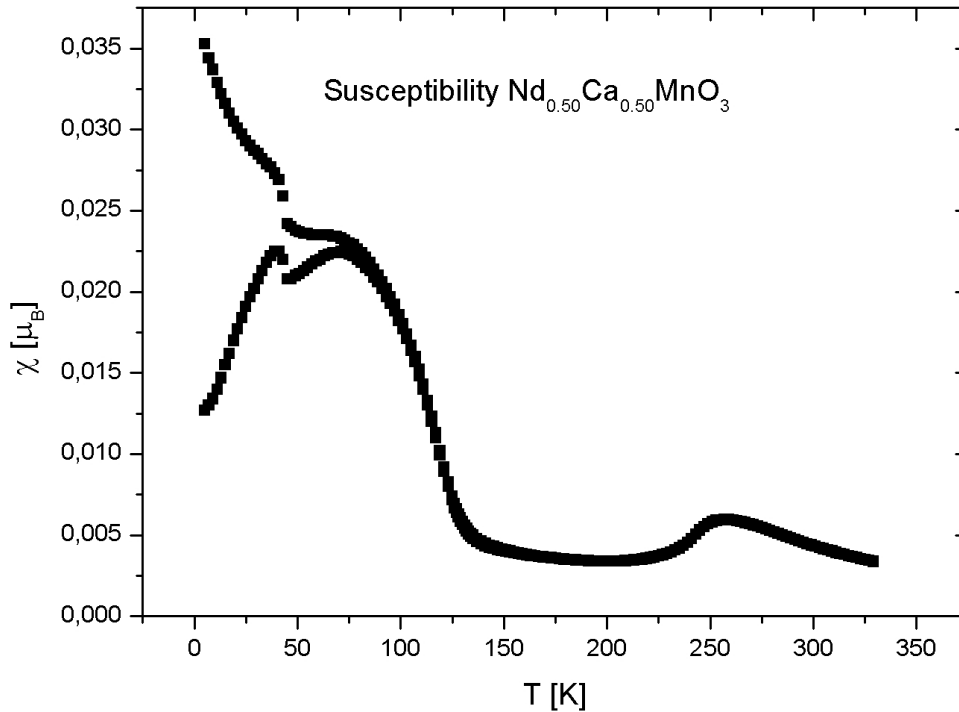


Figure 2.1: Susceptibility of $\text{Nd}_{0.5}\text{Ca}_{0.5}\text{MnO}_3$ obtained by SQUID measurement.

(Magnetic Properties Measurement System) manufactured by Quantum Design [57]. Its detection coils consist of a superconducting wire in a second-derivative configuration: the upper and lower single turns are counterwound with respect to a two turn center coil, see figure 2.2(a).

This detector configuration is used in conjunction with an environmental shield to reduce the noise from nearby magnetic sources. The detection coils are a part of a superconducting loop around one of the Josephson junctions of the SQUID. As the sample is moved through the detection coils, the currents induce changes in the loop. During a scan, the sample is stopped in different positions and the voltage is recorded. The response corresponds to an output voltage as a function of the sample position and is fitted to a theoretical expression to give a very accurate value of the magnetisation.

The sample magnetisation is induced by an applied field of up to 5 Tesla. The temperature range was 5 ÷ 530 K.

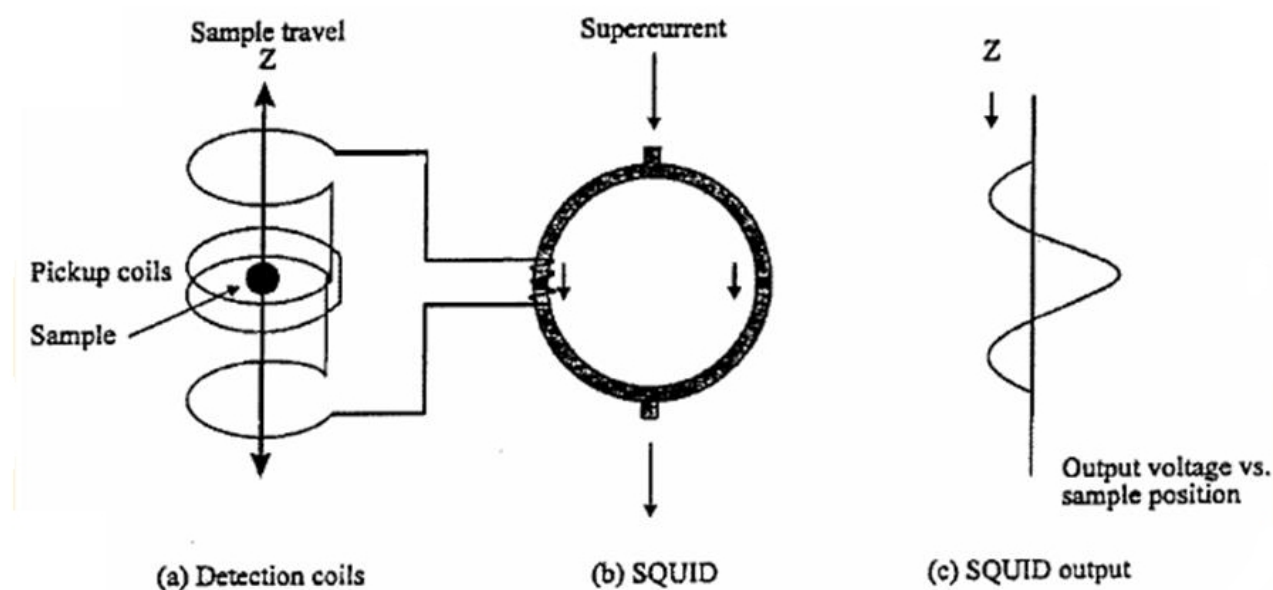


Figure 2.2: Scheme of the MPMS-5S Squid magnetometer showing: (a) second-derivative coil; (b) the Squid loop; (c) the response signal.

2.2 Neutron scattering

Neutrons are, together with protons, the constituents of atomic nuclei. They are not electrically charged but possess a magnetic spin. These two characteristics make neutrons interact with both atomic nuclei and magnetic fields created by unpaired electrons, consequently they are regarded as a useful probe for both structure and magnetic order in crystals.

When a beam of neutrons strikes a material several things can happen. Some will be absorbed, others will emerge in a new direction with or without a change in energy, and the rest will pass through the material unaffected. Those that emerge in a new direction are described as "scattered" neutrons, and the investigation of materials by measuring how they scatter neutrons is known as neutron scattering.

Scattering can be elastic or inelastic according to the exchange of the neutron energy during the collision with the nuclei: for no change in energy, the scattering is elastic, while it is inelastic when a change in the energy occurs.

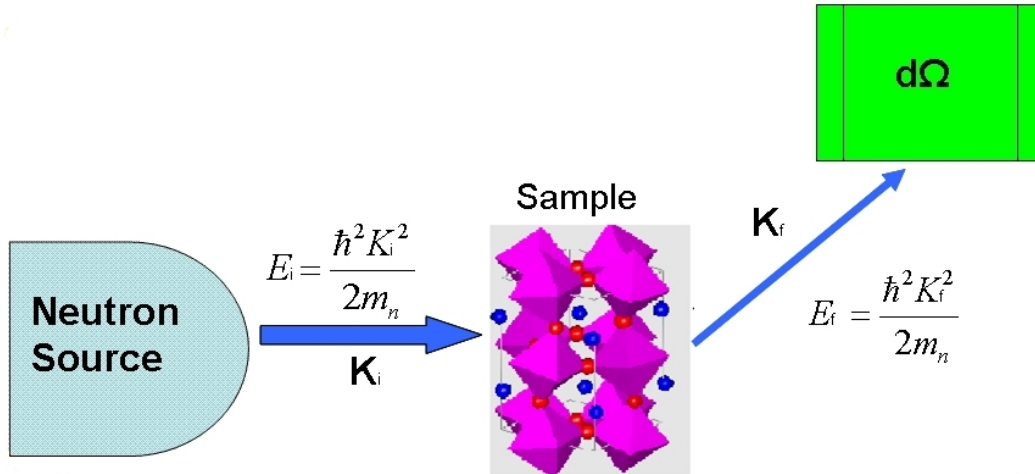


Figure 2.3: Sketch of a neutron scattering experiment

2.2.1 Neutron properties

A low energy (non-relativistic) neutron has energy E , wave vector k , velocity v , and wavelength λ . These quantities are related as follows:

$$k = 2\pi/\lambda, \lambda = h/(mv); E = \frac{1}{2}m_n v^2 = \frac{h^2}{2m_n \lambda^2}, \quad (2.2)$$

where h is Planck's constant and m_n is the mass of the neutron. In a scattering event

Table 2.1: Neutron properties

Mass	≤ 1.008665 [u.m.a.] = 1.675×10^{-27} [Kg]
Charge	$2.2 \times 10^{-20} e$
Spin	1/2
Magnetic moment	-1.913 [μ_B]
Mean life time	888 ± 3 [sec]

(Fig. 2.3, Fig. 2.4 (a)) the energy of the incident neutron is E_i and that of the scattered neutron is E_f . Similarly the incident and scattered neutron wave vectors are k_i and k_f . The "energy transfer": $\hbar\omega = E_i - E_f$ is the energy transferred to the sample by the neutron when it is scattered. Similarly the "wave vector transfer", or "scattering vector", is $\mathbf{Q} = \mathbf{K}_i - \mathbf{K}_f$. The cosine rule, applied to the $(\mathbf{Q}, \mathbf{K}_i, \mathbf{K}_f)$ scattering triangle (Fig. 2.4(b)), gives:

$$Q^2 = K_i^2 + K_f^2 - 2K_i K_f \cos 2\theta \quad (2.3)$$

where 2θ is the "scattering angle" (the angle between the incident and scattered neutron beam directions). For the special case of "elastic scattering", i.e. scattering in which the energy of the neutron does not change, $E_i = E_f$, $\hbar\omega = 0$, $k_i = k_f$, and $Q = 2k_i \sin \theta = 4\pi \sin \theta / \lambda$ where λ_i is the incident wavelength.

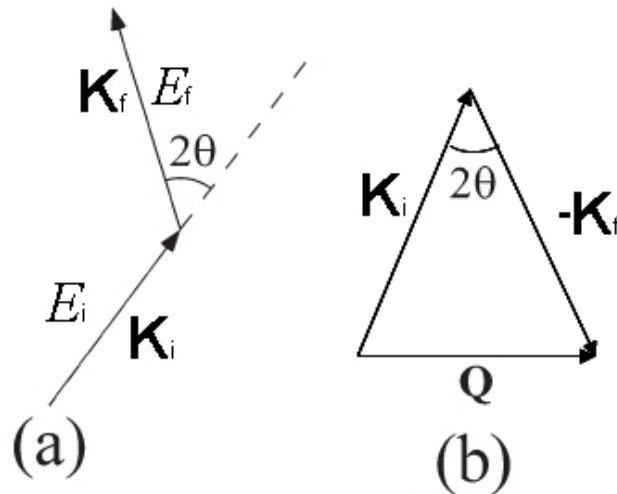


Figure 2.4: A scattering event in real space (a); the corresponding triangle scattering (b)

2.2.2 Neutron diffraction

Neutron diffraction [58] is a powerful technique, based on the elastic scattering of neutrons, which is primarily used to determine the structures and the magnetic ordering in materials. It is also used to study pair distribution functions in non-crystalline solids, liquids and gases.

Scattering can be coherent and incoherent. In the coherent scattering the neutron wave interacts with the whole sample as a unit, so that the scattered waves from different nuclei interfere with each other. This type of scattering depends on the relative distances between the atoms of the sample and thus gives information about the structure of materials. Elastic coherent scattering gives information about the equilibrium structure, whereas inelastic coherent scattering provides information about the collective motion of the atoms.

In order to understand neutron diffraction, we shall discuss the basic theory of the method. Detailed treatments are found in books by Bacon and Squires [58, 59]. The atoms in a crystalline material are periodically arranged. Their positions can be generated by specifying the size and shape of a "unit cell" and the positions of the

atoms within the unit cell. The complete structure is obtained by repeating the unit cell many times in 3 perpendicular directions. This is illustrated in figure 2.5.

The crystal structure is described by three real space basis vectors a , b and c , that

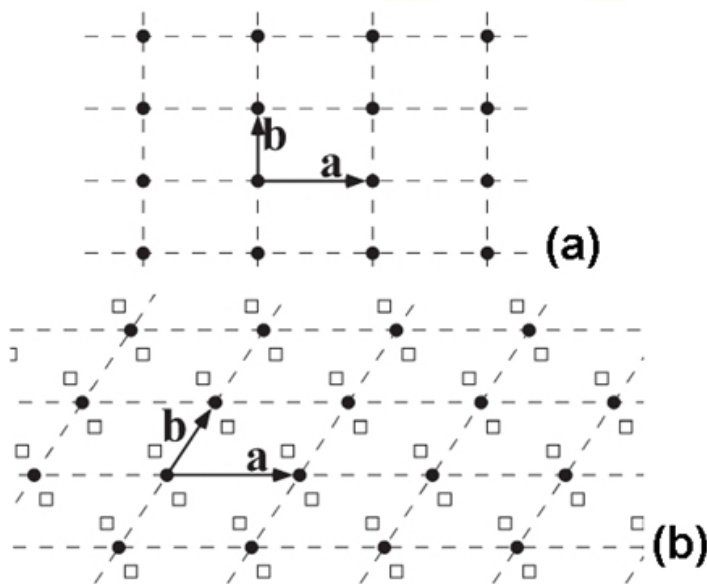


Figure 2.5: Sketch of two-dimensional unit cells, without a basis (a) and with basis (b).

define the size and shape of the unit cell and by the (equilibrium) positions of the atoms within the cell, which are generally expressed in fractional coordinates.

Neutrons are scattered by nuclei, and by atomic magnetic moments due to unpaired electrons. For now we shall only consider the nuclear scattering. We shall also assume (for the time being) that all unit cells are identical (even to the extent that the atoms do not move), and that complicating effects, such as extinction, absorption, inelastic scattering and multiple scattering, can be ignored.

The scattered intensity in a neutron diffraction experiment is proportional to $I_0 N S(\mathbf{Q})$ where I_0 is the incident beam intensity and N is the total number of atoms in the crystal.

The structure factor $S(\mathbf{Q})$ is given by:

$$S(\mathbf{Q}) = 1/N \left| \sum_i^N b_i \exp(i\mathbf{Q} \cdot \mathbf{r}_i) \right|, \quad (2.4)$$

where the sum is over all atoms, \mathbf{r}_i is the position of atom i , and b_i is the "scattering length" or "scattering amplitude" for atom i , which is a measure of the strength of

the interaction between the incident radiation and the atom.

In a crystalline material the periodicity of the lattice implies that $S(\mathbf{Q})$ is zero except at specific values of \mathbf{Q} , such that the phase factors: $\exp(i\mathbf{Q} \cdot \mathbf{r}_i)$ constructively interfere. These special values of \mathbf{Q} , plotted in a 3-dimensional space called "reciprocal space", form a regular grid of points known as the reciprocal lattice. Vectors among these points, called "reciprocal lattice vectors", may be written in terms of three reciprocal space basis vectors \mathbf{a}^* , \mathbf{b}^* and \mathbf{c}^* : $\mathbf{G}_{hkl} = h\mathbf{a}^* + k\mathbf{b}^* + l\mathbf{c}^*$. The "Miller indices" h , k and l are integers which characterize the reflection that occurs when $\mathbf{Q} = \mathbf{G}_{hkl}$. These reflections are known as Bragg reflections, and the peaks observed in diffraction experiments (both with crystals and with powders) are generally called Bragg peaks.

In a single crystal measurement using a mono-directional monochromatic (single wavelength) incident beam, the incident wave vector \mathbf{k}_i is well defined. Since scattering only occurs when $\mathbf{Q} = \mathbf{G}_{hkl}$, and since $\mathbf{k}_f = \mathbf{k}_i - \mathbf{Q}$ (Fig. 2.4 (b)), the scattered neutrons leave from the sample in discrete directions.

In the case of a powder the structure factor must be averaged over all possible crystallite orientations. As long as the dimensions of all crystallites are much greater than those of the unit cell we obtain a simple function of scalar Q , which vanishes except when Q is equal to the magnitude of one of the reciprocal lattice vectors \mathbf{G}_{hkl} .

The scattering from a sample in an idealized experiment with a mono-directional monochromatic incident beam only occurs at scattering angles 2θ such that:

$$\sin \theta = G_{hkl} \lambda_i / 4\pi, \quad i.e. \quad \lambda_i = 2d_{hkl} \sin \theta \quad (2.5)$$

the last one is the Bragg equation [60, 61], where the distance between diffracting planes is $d_{hkl} = 2\pi / G_{hkl}$. Because all crystallite orientations are present the scattered neutrons leave from the sample in "Debye-Scherrer" cones. In other words, for a powder or polycrystalline sample, it is not possible to define the orientation of microcrystal. The random orientation of the axis will generate a pattern corresponding to all possible orientations of the crystal.

The diffraction event can be described in reciprocal space by the Ewald sphere construction. A sphere with radius $1/\lambda$ is drawn through the origin of the reciprocal lattice. Now, for each reciprocal lattice point that is located on the Ewald sphere of reflection, the Bragg condition is satisfied and diffraction arises.

For a fixed incident \mathbf{k} vector, the reciprocal lattice will rotate through all possible angles about the origin, generating Ewald spheres of radius K about the origin.

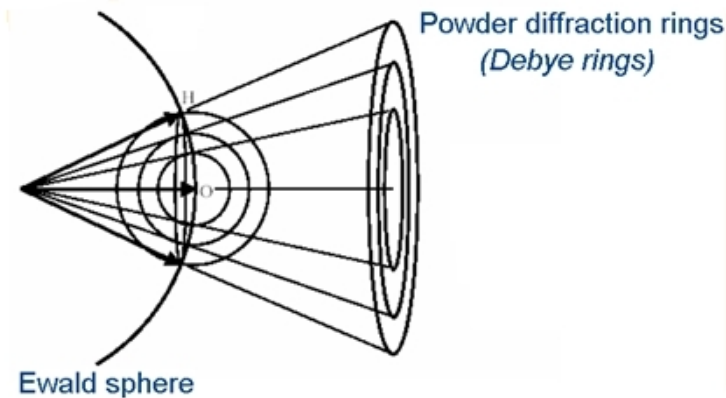


Figure 2.6: The Ewald construction for the powder diffraction method.

For $K < 2k$, each reciprocal lattice intersection with Ewald sphere will result in cones of scattered radiation at an angle ϑ to the forward direction (Fig. 2.6). But not all points in the reciprocal lattice will have Bragg reflections associated with them. The intensity of a Bragg peak is related to condition of constructive interference. The geometrical structure factor gives the possibility of having a Bragg peak or not:

$$S_K = \sum_{j=0}^n e^{iK \cdot d_j}$$

When the structure factor has zero value, no Bragg peak appears. For a zero value of S_K , the interference is destructive.

2.3 Refinement of neutron powder diffraction data

The standard method of analyzing the results of a neutron powder diffraction experiment, known as "Rietveld profile refinement" [62], is to fit the parameters of a model to the measured "profile", which is the intensity of scattered neutron measured as a function of scattering angle 2θ . A typical experimental pattern and the fitted profile are shown in figure 2.7.

2.3.1 Rietveld method

Given a measured neutron powder diffractogram, the Rietveld method allows to:

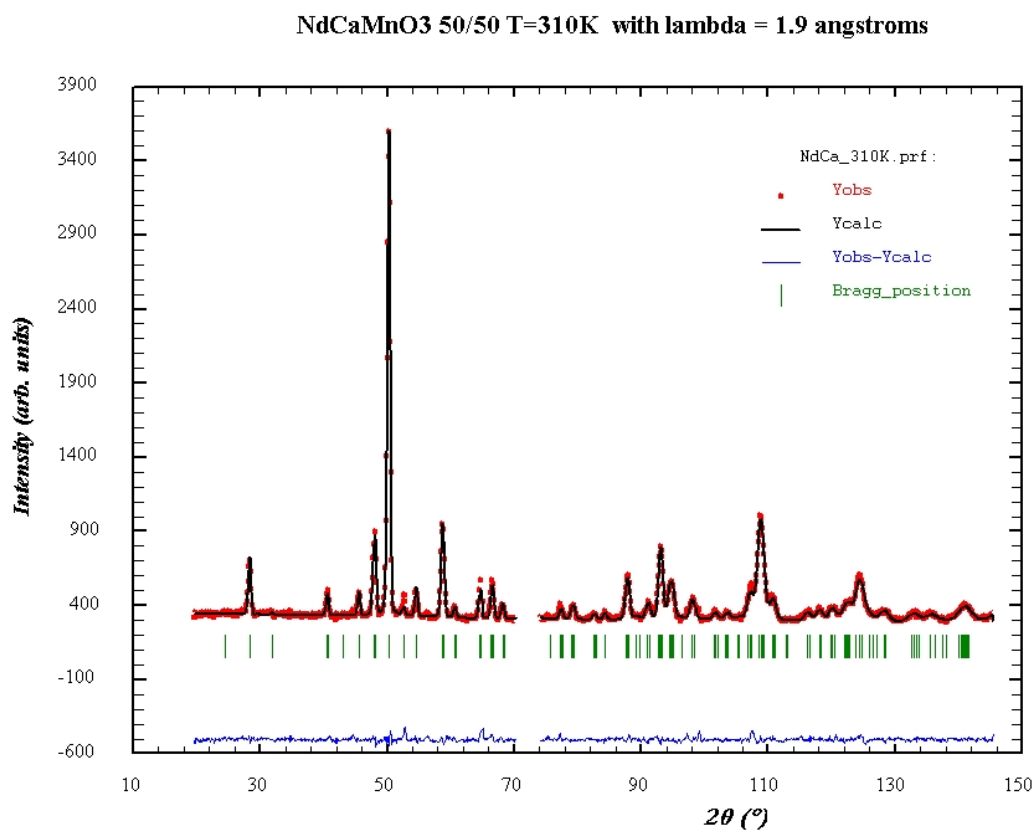


Figure 2.7: Pattern of Nd_{0.50}Ca_{0.50}MnO₃ obtained by Rietveld method refinement.

1. build a model of the crystal structures in terms of cell dimensions, and atomic position;
2. calculate a model diffraction pattern to be compared with the experimental one;
3. minimize the differences between experimental and calculated patterns by least-squares refinement of the model parameters;

The model parameters in a Rietveld refinement can be divided into several categories, according to which aspect of the diffraction pattern they describe. First of all, and most importantly, there are the parameters that determine the positions and the integrated intensities of the Bragg peaks.

Unit cell parameters determine peak positions whereas atom positions within

the unit cell, site occupancies and thermal displacement parameters collectively determine integrated intensities.

Next there are parameters that describe the so-called "background", which is the relatively smooth scattering that lies between and below the Bragg peaks. This can include "Thermal Diffuse Scattering" (TDS) and inelastic and/or incoherent scattering from the sample and its environment, plus the "true" background, which includes contributions due to air scattering, electronic noise, and other unwanted sources.

The Bragg peaks, which correspond to elastic scattering that occurs at well-defined scattering angles, can usually be quite well separated from the background because the background scattering varies rather slowly with scattering angle whereas the Bragg scattering is highly structured.

A third set of parameters describes the shapes of the Bragg peaks. Line broadening is in part due to the resolution of the instrument itself, which is generally a well-parameterized function of 2θ for a given instrumental configuration. There may also be contributions to the broadening due to crystalline size and strain effects.

We refined the neutron powder data by Fullprof program [63], in which we used the part concerning the Rietveld method, explained above.

Fullprof is a program in the FullProf Suite, which is a set of crystallographic programs: FullProf, WinPLOTR, EdPCR, etc..., mainly developed for Rietveld analysis (structure profile refinement) of neutron (constant wavelength, time of flight, nuclear and magnetic scattering) or X-ray powder diffraction data.

Additionally, we used WinPLOTR, which is a program to plot powder diffraction patterns. It can be used to plot raw or normalized data files coming from neutron and X-ray diffractometers (conventional or synchrotron radiation) as well as Rietveld files created by the FullProf refinement program.

The theory of Rietveld method implemented in the Fullprof program will be outlined.

In the kinematic theory (first Born approximation), the amplitude of the wave scattered by an object is the Fourier transform (FT) of its scattering density (SD) $\rho(\mathbf{r})$ measured in cm^{-2} .

The SD means different things for each kind of scattered radiation (X-rays, neutrons and electrons). Any object can be considered as constituted by atoms of SD $\rho_{aj}(\mathbf{r})$ centered at positions \mathbf{R}_j ; the SD and the corresponding scattered

amplitude and intensity can be written as:

$$A(\mathbf{s}) = \sum_j f_j(\mathbf{s}) \exp(2\pi i \mathbf{s} \cdot \mathbf{R}_j) \quad (2.6)$$

$$I(\mathbf{s}) = A(\mathbf{s})A(\mathbf{s})^* = \sum_i \sum_j f_i(\mathbf{s}) f_j(\mathbf{s})^* \exp(2\pi i \mathbf{s} \cdot (\mathbf{R}_i - \mathbf{R}_j)) \quad (2.7)$$

The last two formulae are the basis for the structural study of any kind of material by elastic scattering. The scattering factor of the atoms $f_j(\mathbf{s}) = \text{FT}[\rho_{aj}(\mathbf{r})]$, given in units of length, is the link between the fundamental interaction of each particular radiation with matter. The different ways of writing the equation 2.7 provide specific and simplified formulae for each kind of idealized or defective structure and for different experimental conditions.

For powders, we have to average the intensity for all possible orientations of an object with respect to the incident beam. The intensity depends on the length, s , of \mathbf{s} and the whole set of interatomic distances $R_{ij} = |\mathbf{R}_i - \mathbf{R}_j|$; and is given by the Debye formula in terms of $Q = 2\pi s$:

$$I(Q) = \sum_i \sum_j f_i f_j \sin(QR_{ij})/QR_{ij} \quad (2.8)$$

If we consider the thermal motion of the atoms it is easy to show that the equations 2.6 and 2.7 hold by substituting the scattering factors by $f_i(\mathbf{s}) \exp(-W_i(\mathbf{s}))$. Here the exponential function is called the temperature or Debye-Waller factor.

For simplicity, if not given explicitly, the temperature factors are considered to be included in the scattering factor.

Other kinds of scattering due to thermal motion, e.g. thermal diffuse scattering (TDS), have to be added to equations 2.7 and 2.8 but will not be considered here.

For a powder, the Bragg reflections can be resolved

$$y_i = \sum_{\mathbf{H}} I_{\mathbf{H}} \Omega(T_i - T_{\mathbf{H}}) + D_i + B_i \quad (2.9)$$

where y_i is the number of counts, the subscript "i" represents a discrete observation at the scattering variable T_i . Here we adopt the variable T to describe either, the scattering angle 2θ . \mathbf{H} corresponds to Bragg peaks contributing to the channel "i". $I_{\mathbf{H}}$ is the integrated intensity of the reflection \mathbf{H} , $\Omega(T_i - T_{\mathbf{H}})$ is the value of the normalized profile function of the Bragg reflection at the position T_i due to the reflection \mathbf{H} at the position $T_{\mathbf{H}}$. D_i , is the diffuse scattering due to defects. Finally, B_i is the background coming from other sources (TDS, incoherent

scattering, inelastic, sample environment, etc.).

The information about the average crystal structure is contained in $I_{\mathbf{H}}(\sim F^2)$ and $T_{\mathbf{H}}$ (through the cell parameters). The size and shape of the reflection domains as well as the strains produced by the defects contribute to the profile function $\Omega(T)$.

In the Rietveld method [62], the weighted sum of squared difference between y_{iobs} and y_{ical} 2.9 is minimized. If the set of model parameters is $\beta = (\beta_1, \beta_2, \dots, \beta_n)$, the Rietveld method tries to optimize the chi-square function:

$$\chi_p^2 = \sum_i w_i (y_{iobs} - y_{ical}(\beta))^2 \quad (2.10)$$

where w_i is the inverse of the variance associated to the observation "i" ($\sigma^2(y_{iobs})$).

The integrated intensity for a Bragg reflection is given by:

$$I_{\mathbf{H}} = \{jL A O E F^2\} \quad (2.11)$$

where j is the multiplicity, $L = 1/(2\sin^2 \theta \cos \theta)$ is the Lorentz factor for constant wavelength neutrons, A is the absorption correction, O is a function to correct, if needed, for preferred orientation, E is the primary extinction correction and F is the structure factor of the average unit cell.

2.3.2 Layout of neutron diffractometers

Neutron powder diffraction measurements were carried out at the Institute Laue Langevin (ILL), using the D1A and D20 diffractometers.

On D1A we measured the samples containing Ho, Dy, Er, Tm and Lu, with $\lambda = 1.91 \text{ \AA}$ in the 2θ -range of $8^\circ \div 157^\circ$, with a step of $0.050^\circ 2\theta$. We swept the temperature range 10 and 300K with 1h of measure for each T.

D1A is a reliable instrument for standard crystallographic problems. It gives excellent results with the Rietveld method owing to its near perfect Gaussian peak-shape in the 2θ -range 30° to 150° . The high resolution over a wide range of scattering angles permits the refinement of up to 150 structural parameters by the Rietveld method.

For Pr and Nd compounds the diffraction patterns were collected on D20 high-flux diffractometer at $\lambda = 1.87$ for both.

This instrument is equipped with a large microstrip detector. The complete diffraction pattern at 1536 positions, covering a scattering range of 153.6° , can be obtained in a few seconds. The variable monochromator take-off angle (up to 120°) increases flexibility, providing high-resolution over the complete diffraction pattern

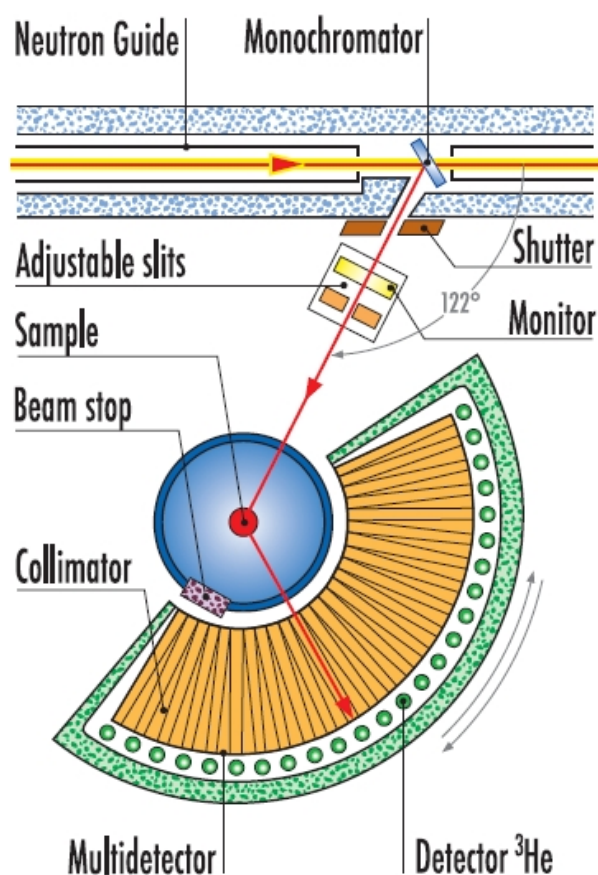


Figure 2.8: High-resolution diffractometer D1A at ILL

at the highest take-off angle. In our case, we used the high-resolution configuration, with take off angle of .

Before Rietveld analysis, diffraction data need several corrections and normalizations. We avoid the subtraction of empty cell signal using a sample holder made in vanadium; this material is a good choice for the diffraction measurements because its signal is mainly incoherent.

For the same reason a measurement of vanadium allow us to calibrate the detector efficiency. A vanadium in the same geometry of the sample and in the same experimental set up is measured for this normalization.

The wavelength is determined with precision using a standard Si sample.

Finally, we took into account the resolution function of the instrument, fixing the profile shape parameters, determined by a refinement of peak shape obtained from a standard sample.

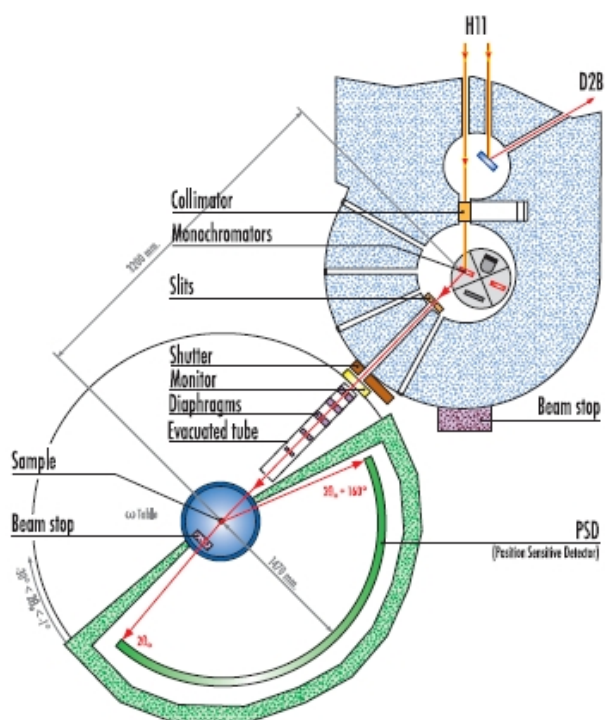


Figure 2.9: High-resolution diffractometer D20 at ILL

Results from SQUID and neutron diffraction measurements will be presented in the next chapter.

3 Résultats expérimentaux et discussion

Le but de cette étude était d'étudier la série des manganites 'half-doped' $\text{Ln}_{0.5}\text{Ca}_{0.5}\text{MnO}_3$ ($\text{Ln} = \text{Ce}, \text{Pr}, \text{Nd}, \text{Tb}, \text{Dy}, \text{Ho}, \text{Er}, \text{Tm}, \text{Yb}$ and Lu) afin d'en extraire leurs propriétés nucléaires et magnétiques.

Dans ce chapitre, nous avons décrit les méthodes de synthèse de nos échantillons expérimentaux ainsi que les résultats obtenus lors des expériences de magnétisme et de diffraction de neutron. Les expériences de magnétisme nous ont notamment permis de détecter la température d'ordre de charge (T_{CO}) de ces composés et de définir la nature des corrélations magnétiques en-dessous et en-dessus de cette température dans le cadre de la théorie des polarons développée par Zener comme proposé par Daoud-Aladine [39].

Les mesures de structures ont été réalisées par diffraction de neutron sur poudre (DNP) à haute résolution à différentes températures afin d'obtenir la structure nucléaire et magnétique et d'observer l'ordre de charge et l'ordre orbital en fonction de la température et du rayon ionique du lanthanide.

Les données obtenus par DNP ont été analysées avec la méthode de Rietveld afin de déterminer des paramètres tels que les paramètres de maille, le volume de la maille, les coordonnées atomiques, les longueurs et angles de liaison, la distorsion de Jahn-Teller, les effets de tilt et la structure magnétique (module et direction angulaire des vecteurs de spin). La variation de certains de ces paramètres en fonction de la température montrent des variations importantes à T_{CO} et cela, même si les pics de Bragg issus de la structure magnétique ne sont observables qu'en dessous de 100K. Ceci est dû au fait que la majorité des pics d'origine magnétique sont confondus avec les pics d'origine nucléaire. De plus, les pics antiferromagnétiques, du fait de leur faible intensité aux petits angles, ont un rapport signal/bruit qui les rend difficile à distinguer.

Les données obtenus par DNP sont également présentées en fonction du rayon ionique du lanthanide afin d'observer l'effet de ce paramètre sur les propriétés magnétiques et nucléaires des composés. La structure nucléaire est obtenue à température ambiante tandis que la structure magnétique est obtenue à la température minimale observée. Nous avons analysé les paramètres de maille, le facteur de Jahn-Teller, l'effet de tilt et la longueur de bande de e_g -Mn en fonction du rayon ionique du lanthanide. Nous avons également étudié la variation en pourcentage du moment magnétique associé à Mn^{3+} et Mn^{4+} due à l'ordre de charge et à l'ordre orbital.

3

Experimental results and discussion

The focus of this work was to study the half-doped manganites of the series $\text{Ln}_{0.5}\text{Ca}_{0.5}\text{MnO}_3$ ($\text{Ln} = \text{Ce}, \text{Pr}, \text{Nd}, \text{Tb}, \text{Dy}, \text{Ho}, \text{Er}, \text{Tm}, \text{Yb}$ and Lu), in order to determine the structural and magnetic properties of these compounds.

In this chapter we describe the method of synthesis of our samples, the results obtained from macroscopic magnetic measurement and from neutron diffraction. In particular, the magnetic measurements allowed us to detect the charge ordering temperature (T_{CO}) of the systems and to define the nature of magnetic correlations above and below T_{CO} in the framework of Zener polarons as proposed by Daoud-Aladine [39].

The structural measurements performed by neutron powder diffraction (NPD) have been carried out at high resolution as a function of temperature, in order to obtain the nuclear and magnetic structure and to observe the charge ordering (CO) and orbital ordering (OO), as a function of temperature and lanthanide ionic radius.

The data obtained by NPD have been analysed by Rietveld method in order to determine the cell parameters, volume cell, atomic fractional coordinates, bond lengths and angles, Jahn-Teller distortion, tilting effect, magnetic structure (module and direction of spin vectors). The variation of different parameters as a function of temperature shows strong changes at T_{CO} , even if the magnetic Bragg peaks are observables only below 100 K. That is because the majority of magnetic peaks are merged with nuclear ones and the AFM peaks, at low angles, have low intensity.

The results from NPD show the effect of decreasing Ln ionic radius on the magnetic and structural features. The ionic structure is obtained at room temperature and the magnetic structure is obtained at the lowest temperature measured. We analysed the cell parameters, Jahn-Teller factor, tilting effect and bandwidth of e_g -Mn as a function of Ln ionic radius. Furthermore, we studied the percentage

variation of magnetic moment associated Mn^{3+} and Mn^{4+} due to the charge ordering and orbital ordering.

3.1 Half-doped manganites series: synthesis

In this section we report the details of the synthesis of our samples in the family of $\text{Ln}_{0.5}\text{Ca}_{0.5}\text{MnO}_3$ ($\text{Ln} = \text{Ce}, \text{Pr}, \text{Nd}, \text{Tb}, \text{Dy}, \text{Ho}, \text{Er}, \text{Tm}, \text{Yb}$ and Lu). Note that the series is not complete. The compounds with $\text{Ln} = \text{Sm}, \text{Eu}$ and Gd were not synthesized because they have a very strong absorption cross-section for neutrons, as reported in the figure 3.1: samples containing this elements can be obtained for neutron measurements using non-absorbing isotopes, but they were too expensive. For the other compounds, polycrystalline samples were synthesized

ZSymbA	σ_{abs}	ZSymbA	σ_{abs}	ZSymbA	σ_{abs}	ZSymbA	σ_{abs}
57-La	8.97(2)	61-Pm-147	168.4(3.5)	65-Tb-159	23.4(4)	69-Tm-169	100.0(2.0)
57-La-138	57.0(6.0)	62-Sm	5922.0(56.0)	66-Dy	994.0(13.0)	70-Yb	34.8(8)
57-La-139	8.93(4)	62-Sm-144	0.7(3)	66-Dy-156	33.0(3.0)	70-Yb-168	2230.0(40.0)
58-Ce	0.63(4)	62-Sm-147	57.0(3.0)	66-Dy-158	43.0(6.0)	70-Yb-170	11.4(1.0)
58-Ce-136	7.3(1.5)	62-Sm-148	2.4(6)	66-Dy-160	56.0(5.0)	70-Yb-171	48.6(2.5)
58-Ce-138	1.1(3)	62-Sm-149	42080.0(400.0)	66-Dy-161	600.0(25.0)	70-Yb-172	0.8(4)
58-Ce-140	0.57(4)	62-Sm-150	104.0(4.0)	66-Dy-162	194.0(10.0)	70-Yb-173	17.1(1.3)
58-Ce-142	0.95(5)	62-Sm-152	206.0(6.0)	66-Dy-163	124.0(7.0)	70-Yb-174	69.4(5.0)
59-Pr-141	11.5(3)	62-Sm-154	8.4(5)	66-Dy-164	2840.0(40.0)	70-Yb-176	2.85(5)
60-Nd	50.5(1.2)	63-Eu	4530.0(40.0)	67-Ho-165	64.7(1.2)	71-Lu	74.0(2.0)
60-Nd-142	18.7(7)	63-Eu-151	9100.0(100.0)	68-Er	159.0(4.0)	71-Lu-175	21.0(3.0)
60-Nd-143	337.0(10.0)	63-Eu-153	312.0(7.0)	68-Er-162	19.0(2.0)	71-Lu-176	2065.(35.)
60-Nd-144	3.6(3)	64-Gd	49700.0(125.0)	68-Er-164	13.0(2.0)		
60-Nd-145	42.0(2.0)	64-Gd-152	735.0(20.0)	68-Er-166	19.6(1.5)		
60-Nd-146	1.4(1)	64-Gd-154	85.0(12.0)	68-Er-167	659.0(16.0)		
60-Nd-148	2.5(2)	64-Gd-155	61100.0(400.0)	68-Er-168	2.74(8)		
60-Nd-150	1.2(2)	64-Gd-156	1.5(1.2)	68-Er-170	5.8(3)		
		64-Gd-157	259000.0(700.0)				

Figure 3.1: Lanthanide atoms and correspondingly neutron scattering absorption cross section in barn for 0.0253 eV stands for estimated values [64].

by means of a solid state reaction: binary oxides of high purity (La_2O_3 (99.99%) Aldrich; Pr_2O_3 (99.9%) Aldrich; Nd_2O_3 (99.9%) Aldrich; Tb_2O_3 (99.9%) Aldrich; Dy_2O_3 (99.9%) Aldrich; Ho_2O_3 (99.9%) Aldrich; Er_2O_3 (99.9%) Aldrich; Tm_2O_3 (99.9%) Aldrich; Yb_2O_3 (99.9%) Aldrich; Lu_2O_3 (99.9%) Aldrich ; Ca (99.9%) Aldrich; MnO_2 (99.999%) Alfa Aesar) were firstly sieved (50 mesh), a mixed in

stoichiometric amounts and finally reacted at high temperature in air. Four thermal treatments with intermediate grinding were carried out, the first at 1523 K for 15 h and the remaining at 1603 K for 18 h. This procedure is necessary to ensure complete reaction and a homogeneous distribution of cations. Phase identification was performed by means of X-ray powder diffraction analysis (XRPD; Philips PW1830; Bragg-Brentano geometry; $\text{CuK}\alpha$; secondary monochromator; 2θ range: 20 - 110°; step: 0.020° 2θ ; sampling time: 15 sec). From literature we know that the compounds with a large ion radius of the element Ln (La, Pr, Nd, Tb and Dy) are crystallized in the orthorhombic structure with the space group $Pbnm$. Compounds with a smaller ionic radius of the element Ln (Ho, Er, Tm, Yb, Lu) exhibit generally the hexagonal crystal structure with the space group $P63cm$ if the calcium content is zero or less than 50% but crystallize in the orthorhombic form in the half-doped composition. All our samples crystallised in the orthorhombic form. An attempt for synthesizing $\text{Ce}_{0.5}\text{Ca}_{0.5}\text{MnO}_3$ seemed to lead to the separation of Ce-rich oxide and CaMnO_3 . However the formation of this phase cannot be excluded because the CeMnO_3 crystal structure does not exist in the database but a study of the Ce-doped LaMnO_3 in the whole series of $\text{La}_{1-x}\text{Ce}_x\text{MnO}_3$ has been reported in literature [65] and the related Ca-doped compounds could be synthesized. In this case, by analogy with the hole-doped systems one could also have double exchange between Mn^{2+} and Mn^{3+} ; such a system would be an interesting electron doped system.

The sample containing Tb resulted (by XRPD measurements) to be not well synthesised.

The samples were studied by magnetic measurements using a Quantum Design SQUID magnetometer and by neutron diffraction analysis. In table 3.1, we report the samples, the instruments used for measurements, and the corresponding temperatures.

3.2 Bulk magnetic properties: susceptibility measurements

The samples were characterized, first of all, by macroscopic magnetic measurements on a SQUID magnetometer, see chapter 2.1. The macroscopic susceptibility were measured in the temperature range 5 ÷ 530 K, both *field-cooling* (FC), with an applied magnetic field of 500 G, and *zero field-cooling* (ZFC). The measurements have been corrected for the mass of each sample.

Samples	Elec. Conf.	R_{ion} Ln	Instruments
$Ce_{0.5}Ca_{0.5}MnO_3$	$4f^6$	1.034	XRPD
$Pr_{0.5}Ca_{0.5}MnO_3$	$4f^3$	1.013	D20
$Nd_{0.5}Ca_{0.5}MnO_3$	$4f^4$	0.995	D20
$Tb_{0.5}Ca_{0.5}MnO_3$	$4f^9$	0.923	XRPD
$Dy_{0.5}Ca_{0.5}MnO_3$	$4f^{10}$	0.912	D1A
$Ho_{0.5}Ca_{0.5}MnO_3$	$4f^{11}$	0.901	D1A
$Er_{0.5}Ca_{0.5}MnO_3$	$4f^{12}$	0.881	D1A
$Tm_{0.5}Ca_{0.5}MnO_3$	$4f^{13}$	0.869	D1A
$Yb_{0.5}Ca_{0.5}MnO_3$	$4f^{14}$	0.858	XRPD
$Lu_{0.5}Ca_{0.5}MnO_3$	$4f^{14} 5d^1$	0.848	D1A

Table 3.1: Table of samples, electronic configuration of the atoms, ionic radius in \AA of Ln and the instruments used.

We can observe in figure 3.2 that in the magnetic susceptibilities a broad peak is present corresponding to the temperature where CO occurs. Only for the compounds containing Pr and Nd this CO-peak is clearly evident. In the all other samples, it is not so evident. We reported in figure 3.2, as an example, the case of $Lu_{0.5}Ca_{0.5}MnO_3$, for which the CO peak is shown in the in-set where we plot the inverse of susceptibility, see in-set in figure 3.2.

The presence of the peak in the susceptibility at charge ordering temperature corresponds to a change in the nature of the magnetic correlations above and below T_{CO} .

The magnetic susceptibility at high temperature, follows the Curie-Weiss law with a positive Weiss constant θ in the equation:

$$\chi = \frac{C}{T - \theta} \quad (3.1)$$

Above T_{CO} , the electronic localization is associated with ferromagnetic correlations (double exchange) and below T_{CO} with antiferromagnetic correlations of super exchange following a Curie-Weiss law with a negative Weiss constant θ (Néel temperature T_N).

This behavior may be explained by the hypothesis of the presence of a Zener polarons order [39], the paramagnetic states, above and below T_{CO} are different because the elementary magnetic unit changes. The change of the magnetic

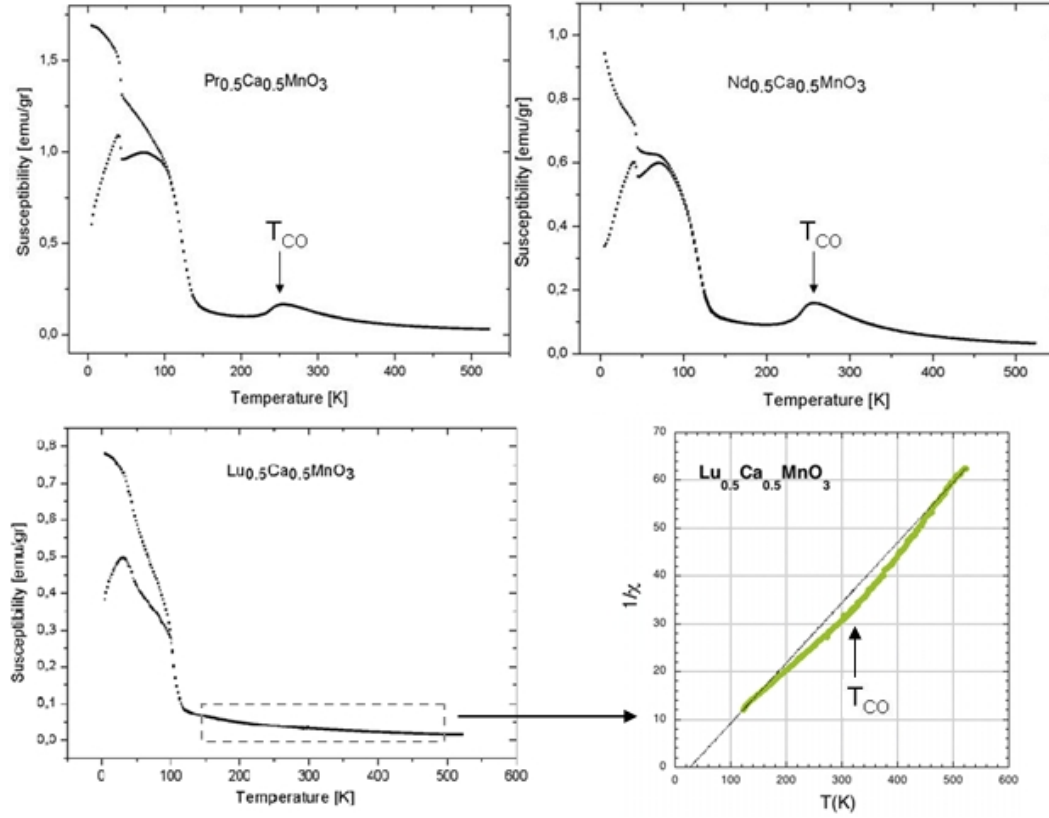


Figure 3.2: Susceptibility measurement, by SQUID, of $\text{Pr}_{0.5}\text{Ca}_{0.5}\text{MnO}_3$, $\text{Nd}_{0.5}\text{Ca}_{0.5}\text{MnO}_3$, and $\text{Lu}_{0.5}\text{Ca}_{0.5}\text{MnO}_3$ in FC and ZFC, in the temperature range 5 ÷ 530 K.

correlations explains the presence of localized electrons, produced by the local double exchange process between confined electrons. The system changes from paramagnetic order to AFM phase between Zener polarons, therefore the magnetic interactions must be described by super-exchange theory.

In the Zener polarons model, the Curie constant changes through the charge ordering temperature and it depends on the paramagnetic unit moment μ_{eff} of the system.

Far above T_{CO} the Zener polarons do not exist. Then, in order to explain the behavior of the susceptibility above T_{CO} , we considered the system as a semi-conductor with mixed valence of $\text{Mn}^{3+}/\text{Mn}^{4+}$. The total effective moment $\bar{\mu}_{eff}$ is:

$$\bar{\mu}_{eff} = \sqrt{1/2\mu_{\text{Mn}^{3+}}^2 + 1/2\mu_{\text{Mn}^{4+}}^2} \cong 4.4\mu_B \quad (3.2)$$

where

$$\mu_{\text{Mn}^{3+}} = 2\sqrt{S(S+1)}$$

with $S = 2$ and

$$\mu_{Mn^{4+}} = 2\sqrt{S(S+1)}$$

with $S = 3/2$.

Below T_{CO} the Zener polarons are formed; in this case, we consider the total effective moment $\bar{\mu}_{eff,pol}$ of Mn-Mn ferromagnetic pair as the total moment of Mn-O-Mn unit, where the anisotropic redistribution of charge is analogous to the OO establishment of d_{z^2} type; hence, we can consider that the Mn-Mn pair has fixed orbital moment. The effective moment of Mn-Mn pair contains the localized magnetic moment for each Mn ion, with $S = 3/2$, due to the localized t_{2g} electrons. The magnetic moments are coupled by an electron that has $s = 1/2$ and the hybrid orbital symmetry: $Mnd_{z^2} - O_{2p\sigma} - Mnd_{z^2}$. Therefore, the total magnetic moment associated to the Mn-O-Mn is $S = 7/2$ ($S[Mn] = 3/2 - S[Mn] = 3/2 - s=1/2$), supposing that the electronic state comes out from the electron and the magnetic moment, strong Hund coupling.

The total effective moment $\bar{\mu}_{eff,pol}$ is:

$$\bar{\mu}_{eff,pol} = \sqrt{1/2\mu_{Mn^{3+}}^2 + 1/2\mu_{Mn^{4+}}^2} = 7.9\mu_B \quad (3.3)$$

where

$$\mu_{Mn^{3+}} = 2\sqrt{S(S+1)}$$

with $S = 7/2$ and

$$\mu_{Mn^{4+}} = 2\sqrt{S(S+1)}$$

with $S = 7/2$.

In the ideal half-doped system, where below T_{CO} Mn-Mn pairs are present and perfectly ordered at long range, the system is formed by $N/2$ Mn-Mn pairs of $\mu_{eff,pol}$. This suggests that the Curie constant decrease by a factor:

$$C_{LT}/C_{HT} = \frac{1}{2} \frac{\mu_{eff,pol}}{\bar{\mu}_{eff}} = 1.62. \quad (3.4)$$

where C_{LT} and C_{HT} are the Curie constants at low and high temperature, respectively.

We performed a linear fit of the inverse susceptibility in the paramagnetic range (see figure 3.3), below and above T_{CO} for $Pr_{0.5}Ca_{0.5}MnO_3$, $Nd_{0.5}Ca_{0.5}MnO_3$, $Er_{0.5}Ca_{0.5}MnO_3$, $Yb_{0.5}Ca_{0.5}MnO_3$ and $Lu_{0.5}Ca_{0.5}MnO_3$, in order to obtain the

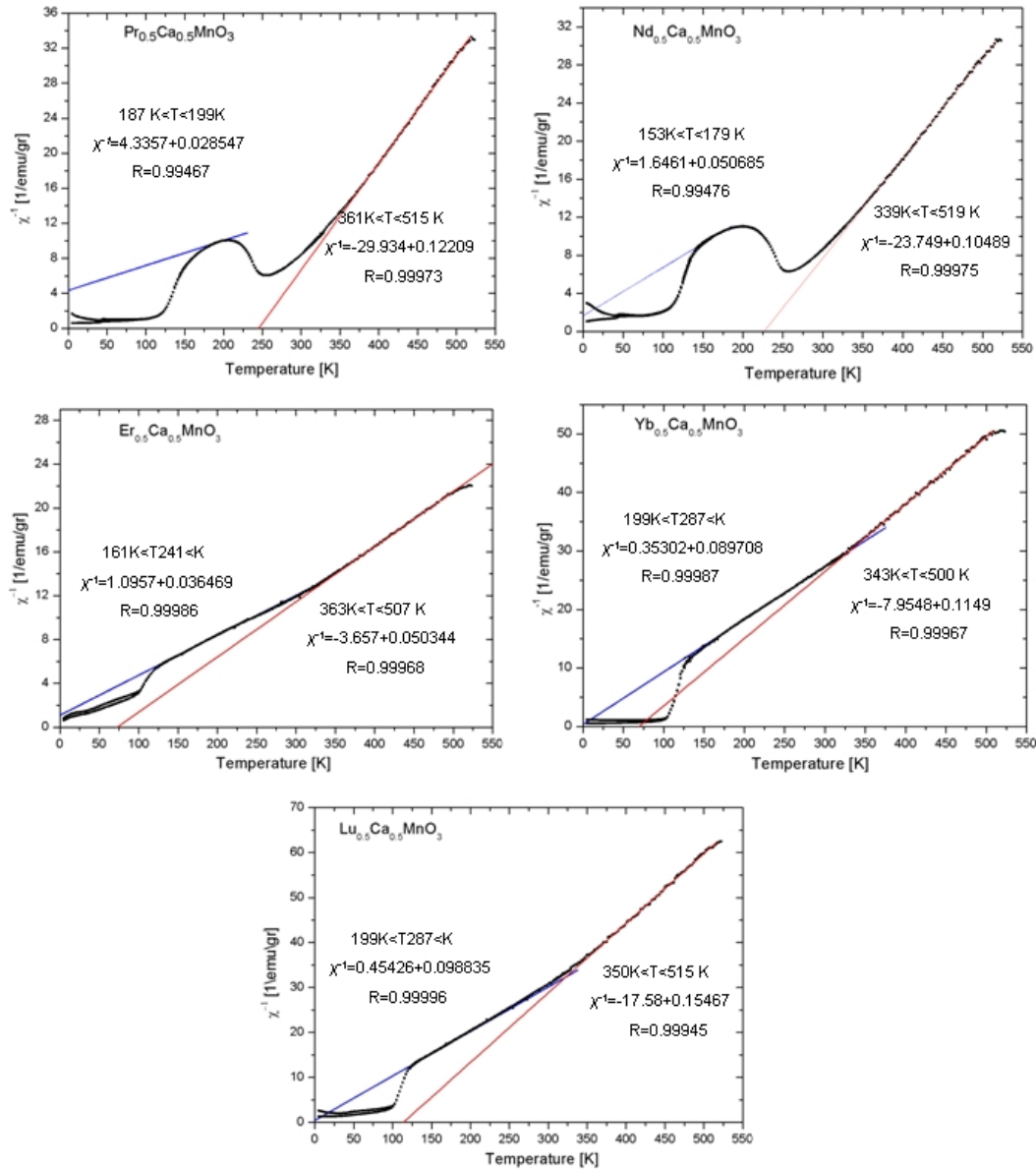


Figure 3.3: Inverse susceptibility of $\text{Pr}_{0.5}\text{Ca}_{0.5}\text{MnO}_3$, $\text{Nd}_{0.5}\text{Ca}_{0.5}\text{MnO}_3$, $\text{Yb}_{0.5}\text{Ca}_{0.5}\text{MnO}_3$, $\text{Er}_{0.5}\text{Ca}_{0.5}\text{MnO}_3$ and $\text{Lu}_{0.5}\text{Ca}_{0.5}\text{MnO}_3$, in the temperature range 0 ÷ 530 K.

Curie-Weiss temperature Θ_{CW} and the Curie constant C_{LT}/C_{HT} , below and above T_{CO} , respectively. We chose these samples for this analysis because for the other sample high temperature susceptibility is not either available and we cannot determine the Curie region and T_{CO} .

The calculated ratio between the Curie-Weiss constant below and above the T_{CO}

Samples	T_C [K]	T_N [K]	T_{CO} [K]	C_{LT}/C_{HT}
$\text{Pr}_{0.5}\text{Ca}_{0.5}\text{MnO}_3$	245	-150	250	4.23
$\text{Nd}_{0.5}\text{Ca}_{0.5}\text{MnO}_3$	226	-32	245	2.35
$\text{Er}_{0.5}\text{Ca}_{0.5}\text{MnO}_3$	72	-32	300	1.39
$\text{Yb}_{0.5}\text{Ca}_{0.5}\text{MnO}_3$	69	-4	330	1.31
$\text{Lu}_{0.5}\text{Ca}_{0.5}\text{MnO}_3$	113	-4.3	315	1.55

Table 3.2: Table of Néel temperature T_N , charge ordering temperature T_{CO} and C_{LT}/C_{HT} obtained by inverse susceptibility analysis.

are reported in table 3.2. The values for $\text{Er}_{0.5}\text{Ca}_{0.5}\text{MnO}_3$, $\text{Yb}_{0.5}\text{Ca}_{0.5}\text{MnO}_3$ and $\text{Lu}_{0.5}\text{Ca}_{0.5}\text{MnO}_3$ are in good agreement with the theoretical ratio C_{LT}/C_{HT} of 1.62 calculated.

In the case of compounds containing Pr and Nd, these values seem to be quite high. In fact, the temperature range on which we performed the linear Curie-Weiss fit is very tight, and the regression coefficient R is low compared to the R of other samples and the results are less reliable.

3.3 Nuclear and magnetic structure of $\text{Ln}_{0.5}\text{Ca}_{0.5}\text{MnO}_3$ compounds

Using the high-flux powder diffractometer D20 and the high-resolution powder diffractometer D1A, at ILL, we performed crystallographic measurements (see in table 3.1) as a function of temperature, in the range 10 ÷ 300 K. The neutron diffraction patterns have been treated with the FullProf suite program [63], in order to obtain the crystal and the magnetic structures of our compounds.

The choice of temperatures was made following the change in the SQUID measurements of susceptibility.

We decided to take the diffraction diagram:

- at room temperature, in order to obtain a well defined nuclear structure;
- close to the charge ordering temperature, in order to see any structural change due to the CO event;
- below T_{CO} down to 10 K in order to determine the magnetic ordering and the magnetic structure.

We performed the Rietveld refinement in the $Pbnm$ description, using as starting points the data present in literature, for the $\text{Pr}_{0.5}\text{Ca}_{0.5}\text{MnO}_3$ [66, 67, 39], $\text{Nd}_{0.5}\text{Ca}_{0.5}\text{MnO}_3$ [68, 69] and $\text{Ho}_{0.5}\text{Ca}_{0.5}\text{MnO}_3$ [70], which have an *ICSD* [71] table with coordinates and cell parameters, available.

We have used the following procedure and the refinement in order to obtain: cell parameters, atomic coordinates, bond lengths and angles, Jahn-Teller distortion effect, tilting of orthorhombic structure, magnetic moment (module, φ and ϑ angle) and the magnetic phase-type.

Firstly, we refined the scale factor and zero point of detector. The scale factor value well done is very important to analyze both, ionic and magnetic structure; in fact, the scale factor of the nuclear structure is related to the magnetic phase and we have to know correctly this value in order to get reliable values of magnetic moments.

Next, we refined lattice parameters and atomic coordinates; then, we refined the occupancy in order to verify that the x-doping equal 0.5. For the case of $\text{Pr}_{0.5}\text{Ca}_{0.5}\text{MnO}_3$ we could not refine the occupancy because there is not enough difference of absorption cross-section for neutrons between Ca and Pr. From the Rietveld analysis we found that Pr, Nd, Ho and Lu are single phase samples with an occupancy of 0.5. The other samples resulted composed principally of $\text{Ln}_{0.5}\text{Ca}_{0.5}\text{MnO}_3$ but with a presence of a second phase with composition very closed to 0.5 (see table B.1 in annex 2).

For each temperature, we refined the Debye-Waller factor, that describes the attenuation of coherent neutron scattering caused by thermal motion; this parameter is also related to the topological disorder of the system.

Finally, we refined the background.

In figure 3.4, we show, as example, the pattern of $\text{Pr}_{0.5}\text{Ca}_{0.5}\text{MnO}_3$ at room temperature and at 20 K. The structure is orthorhombic in the $Pbnm$ symmetry group across the measured temperature range; the monoclinic refinement was tested and we did not observe any structural phase transition between 10 and 310 K, as observed by others groups before us in similar samples with a slight different content of Pr, where an orthorhombic to monoclinic phase transition occurs [67, 39]. We have the same results for all our samples.

The quality of our refinements can be seen in the spectra-difference as well the values of Bragg-factor, R_{wp} and χ^2 reported in table 3.3.

The room temperature spectrum provides the ionic structure, which is the starting point to follow the temperature evolution of the structural parameters as the temperature decreases.

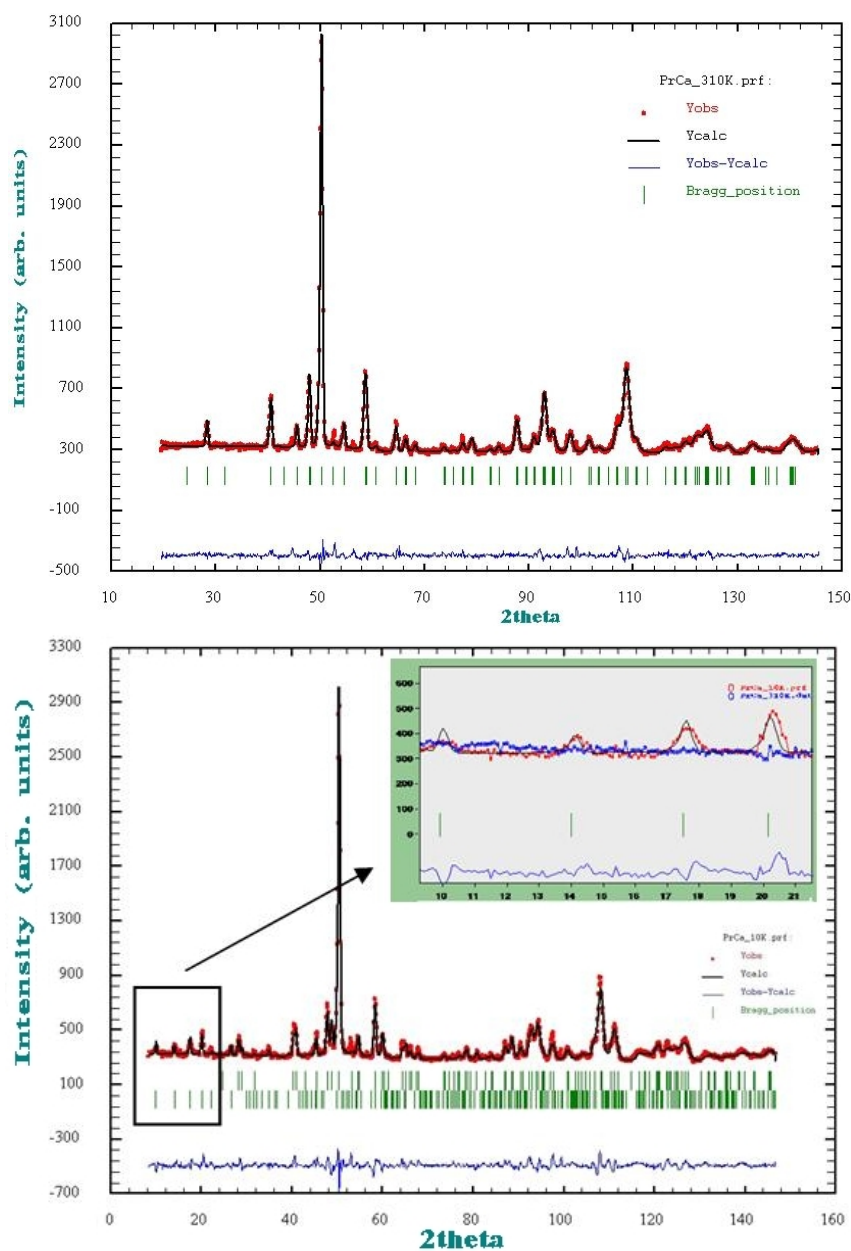


Figure 3.4: Diffraction pattern of $\text{Pr}_{0.5}\text{Ca}_{0.5}\text{MnO}_3$ at $T = 300\text{K}$, and $\text{Pr}_{0.5}\text{Ca}_{0.5}\text{MnO}_3$ at $T = 20\text{K}$, $D_{20}, \lambda = 1,9 [\text{\AA}]$. The lower solid lines show the difference profiles and the tick marks show the reflection positions.

The magnetic correlations, in the diffraction patterns, appear only below $T \sim 100\text{K}$ in all our systems. In fact, below this temperature magnetic peaks appear in the low angle region, that do not coincide with crystal structure Bragg peaks, indicating a magnetic structure. Therefore, we introduce the magnetic phase as a second

structural phase.

Generally the magnetic structure is a CE-type, which is quite complex: it entails

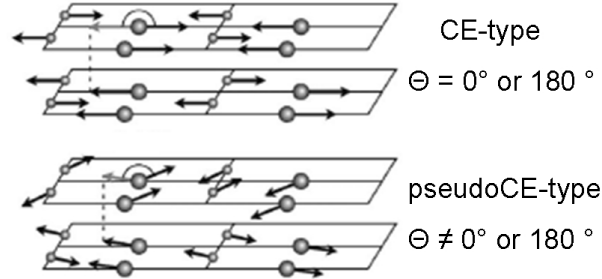


Figure 3.5: Scheme of CE and *pseudo*-CE magnetic structure. The arrows in gray of the upper planes correspond to the translation of the magnetic moment of the Mn placed must below, in order to visualize the angle θ between the two magnetic moment [68].

a quadrupling of the volume of the original orthorhombic unit cell and consists of two magnetic sublattices with independent propagation vectors. This observation confirms the hypothesis, formulated by Goodenough [5] and developed by others [72, 73] that two sublattices resulting from charge ordering between Mn^{3+} and Mn^{4+} are present. In Goodenough's model, charge ordering is associated with an orbital ordering forming ferromagnetic *zigzag chains* in the xy -plane (d_{z^2} Mn^{3+} orbitals associated with the long Mn^{3+} - O bonds in the Jahn-Teller distorted Mn^{3+} - O_6 octahedra, see figure 3.5) CE-type. These ferromagnetic chains are connected antiferromagnetically to each other in the xy -plane and along z -direction.

The magnetic structures of the two sublattices have different propagation vectors: $\mathbf{k}_1 = (0, 0, 1/2)$ for Mn^{3+} and $\mathbf{k}_2 = (1/2, 0, 1/2)$ for Mn^{4+} . This model gives the presence of two peaks at low angles. In all our samples, we observed four magnetic peaks in the low angle region, around $2\Theta \sim 10^\circ, 14^\circ, 18^\circ$ and 20° , respectively, (see in-set in figure 3.4 for the Pr compound). In this case, the structure is described using the *pseudo*-CE model, instead of CE model, which means that the propagation vectors change to $\mathbf{k}_1 = (1/2, 0, 0)$ and $\mathbf{k}_2 = (1/2, 1/2, 0)$, and the θ angle differs from the standard values 0° and 180° . Their refined values are presented in table 3.3.

Furthermore in table 3.3, we report the lattice parameters, the atomic coordinates, bond angles and lengths, the module, φ -angle and ϑ -angle of spin vector obtained by Rietveld refinement. Only the results of $\text{Pr}_{0.5}\text{Ca}_{0.5}\text{MnO}_3$, $\text{Nd}_{0.5}\text{Ca}_{0.5}\text{MnO}_3$ and

$\text{Lu}_{0.5}\text{Ca}_{0.5}\text{MnO}_3$ are reported, as examples, for the all systems studied. For the other samples the results are reported in the annex B.2.

Here, we choose to present the results for the samples containing Pr and Nd because they are comparable with the literature results and for the compound containing Lu as representative for the other samples. In addition, in the fig. 3.6 is shown the pattern for the LuCa compound at room temperature.

We analyzed the bond lengths in order to understand the distortion of the

Parameters	$\text{Pr}_{0.5}\text{Ca}_{0.5}\text{MnO}_3$		$\text{Nd}_{0.5}\text{Ca}_{0.5}\text{MnO}_3$			$\text{Lu}_{0.5}\text{Ca}_{0.5}\text{MnO}_3$		
	300 [K]	10 [K]	310 [K]	20 [K]	10 [K] (Millange [69])	300 [K]	10 [K]	
a[Å]	5.3951(7)	5.4206(7)	5.3829(3)	5.4132(3)	5.4157(1)	5.2647(3)	5.3143(1)	
b[Å]	5.3977(7)	5.4256(6)	5.4007(4)	5.4336(3)	5.4354(1)	5.5044(2)	5.4667(1)	
c[Å]	7.6055(8)	7.4779(5)	7.5932(5)	7.4858(3)	7.4832(1)	7.4145(4)	7.4026(1)	
V[Å ³]	221.4798(7)	219.9240(6)	220.7446(4)	220.1801(3)	220.2791(1)	214.8645(3)	215.0576(1)	
Ln/Ca	x	0.0020(1)	-0.0139(1)	-0.0026(1)	-0.00924(1)	-0.0057(4)	-0.0187(1)	-0.0153(1)
	y	0.0269(1)	0.0214(1)	0.0314(1)	0.02927(1)	0.0349(2)	0.0648(1)	0.0668(1)
O ₁	x	0.2821(1)	0.2781(1)	0.7149(1)	0.71865(1)	0.0722(4)	0.3051(1)	0.3007(1)
	y	0.7147(1)	0.7181(1)	0.2861(1)	0.28360(1)	0.4862(3)	0.6996(1)	0.6995(1)
	z	-0.0339(1)	-0.0348(1)	0.0358(1)	0.03696(1)	0.0375(2)	-0.0492(1)	-0.0494(1)
O ₂	x	0.4321(2)	0.4281(1)	0.0713(2)	0.07564(1)	-0.2859(2)	0.4065(1)	0.4091(1)
	y	-0.0117(1)	-0.0089(1)	0.4856(1)	0.48695(1)	0.2886(2)	-0.0291(1)	-0.0279(1)
Mn-O _{eq} [Å]	1.937(6)	1.934(6)	1.941(4)	1.944(3)	1.953(1)	1.979(4)	1.961(3)	
Mn-O _{eq} [Å]	1.955(6)	1.964(6)	1.951(4)	1.963(3)	1.960(1)	1.981(5)	1.993(3)	
Mn-O _{ap} [Å]	1.931(2)	1.911(2)	1.938(1)	1.917(1)	1.911(1)	1.924(2)	1.912(1)	
Mn-O _{eq} -Mn[deg]	158.4°(3)	159.4°(4)	157.2°(2)	158.1°(2)	157.3°(2)	148.2(2)	148.9(1)	
Mn-O _{ap} -Mn[deg]	157.9°(1)	156.3°(1)	156.7°(1)	154.9°(1)	156.3°(1)	148.8(1)	149.5(1)	
μ_{Mn}^{3+}	-	2.25(5)	-	2.45(5)	2.6	-	1.09(6)	
μ_{Mn}^{4+}	-	2.05(5)	-	2.25(5)	2.4	-	0.89(6)	
φ	-	104°	-	127°	-	-	229°	
ϑ	-	61°	-	61°	-	-	50°	
Bragg-f	3.4	5.8	3.4	5.02	4.14	3.8	4.5	
R _{wp}	2.6	4.2	2.6	3.6	5.37	5.02	2.57	
χ^2	5	7	5	8	2.03	2.8	3.1	

Table 3.3: $\text{Pr}_{0.5}\text{Ca}_{0.5}\text{MnO}_3$, $\text{Nd}_{0.5}\text{Ca}_{0.5}\text{MnO}_3$ and $\text{Lu}_{0.5}\text{Ca}_{0.5}\text{MnO}_3$ structural parameters determined at room and low T temperature; the manganese atom is in high symmetry site (1/2, 0, 0). We have compared $\text{Nd}_{0.5}\text{Ca}_{0.5}\text{MnO}_3$ structural and magnetic parameters, at low temperature, with available results in lecture [69]. We found the pseudo-CE magnetic phase; we reported the modules of μ_{Mn}^{3+} and μ_{Mn}^{4+} , plane-angle of φ , space-angle of ϑ associated at spin vector of Mn atom.

orthorhombic structure inside the perovskite. We found that an inverse Jahn-Teller effect occurs: i.e. the Mn-O_{eq} bond lengths (distances between Mn atom and O atom in the ab plane) are greater than Mn-O_{ap} bond lengths (distances between Mn atom and O atom along z-direction), inducing a compression effect along the

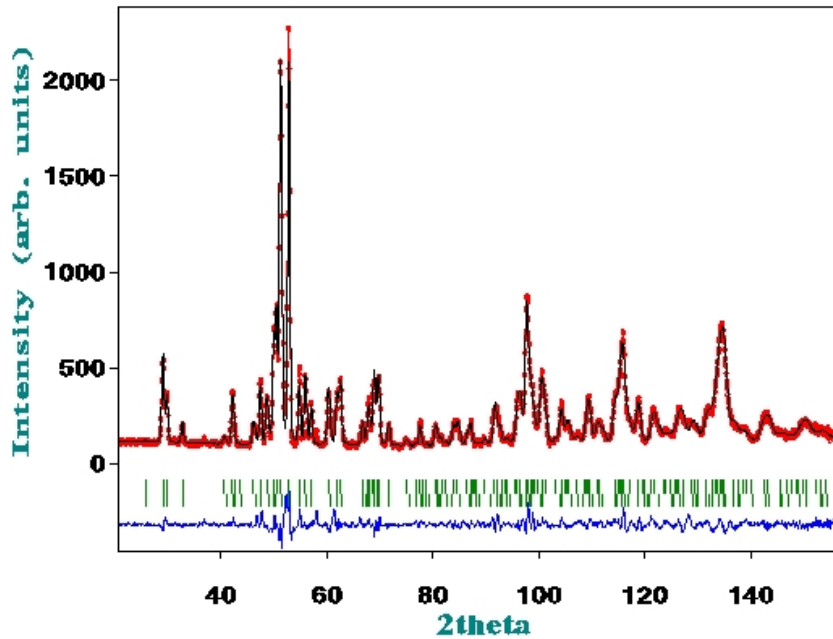


Figure 3.6: Pattern of $\text{Lu}_{0.5}\text{Ca}_{0.5}\text{MnO}_3$ at $T = 300 \text{ K}$ and $\lambda = 1.9 \text{ \AA}$

z-axis. A similar effect was observed for the same compound by Millange et al., see table 3.3, but in our case the difference between Mn-O_{eq} distances is more pronounced.

From the analysis of the cell parameters, the Jahn-Teller factor and Mn-O-Mn

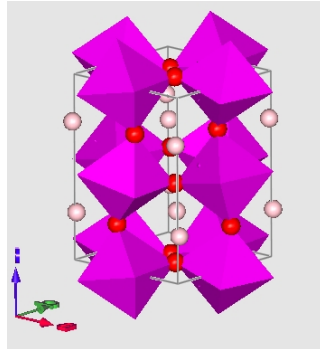


Figure 3.7: $\text{Pr}_{0.5}\text{Ca}_{0.5}\text{MnO}_3$ with the orthorhombic polyhedron MnO_6 . The Pr/Ca atoms are represented with silver color, the O atoms in red color and the Mn atoms, inside the polyhedron, in magenta color.

bond angles are shown in figure 3.8 and compared with susceptibility, where the T_{CO} is evident. We observe clearly that at T_{CO} the samples present a strong distortion of the structure. At T_{CO} , the Mn-O-Mn bond angles in Mn-O_{ap} direction

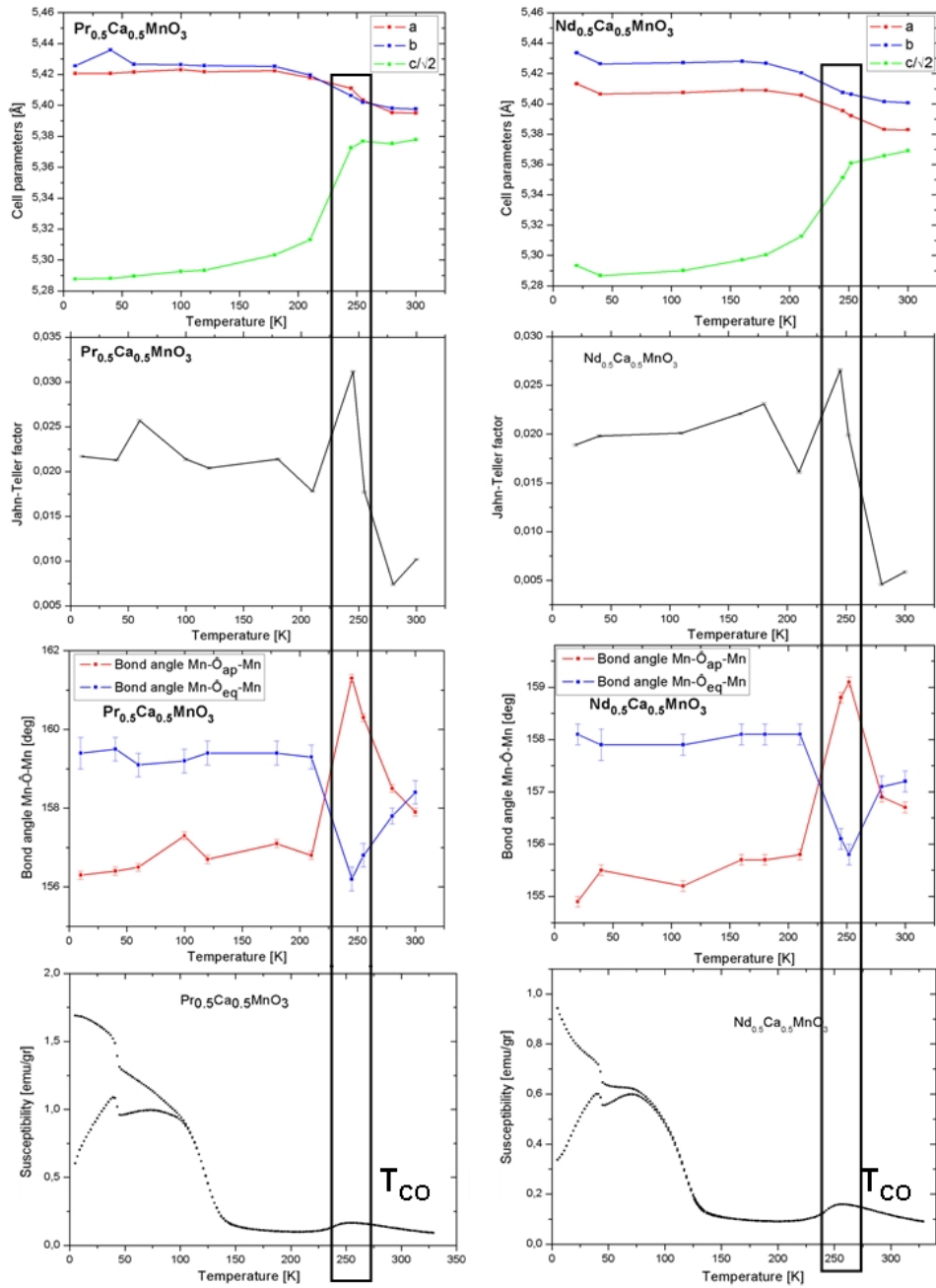


Figure 3.8: Cell parameters, Jahn-Teller effect, Tilting of octahedra and susceptibility of $\text{Pr}_{0.5}\text{Ca}_{0.5}\text{MnO}_3$ and $\text{Nd}_{0.5}\text{Ca}_{0.5}\text{MnO}_3$. In the square, we emphasize the charge ordering region.

is bigger than the bond angles in the Mn-O_{eq} direction and the bandwidth in the xy -plane is smaller than the bandwidth in the z -direction (see figure 3.9). This means that at T_{CO} the carrier mobility is reduced in the xy -plane. Above T_{CO} , the

nature of magnetic correlations is FM with an increasing of the double exchange interactions. Under T_{CO} , the bandwidths decrease indicating a localization of the carriers which will stabilize orbital and charge ordering corresponding to an augmentation of the magnetic moment at low temperature, see figure 3.10.

All other samples present similar features consistent with results presented for Pr

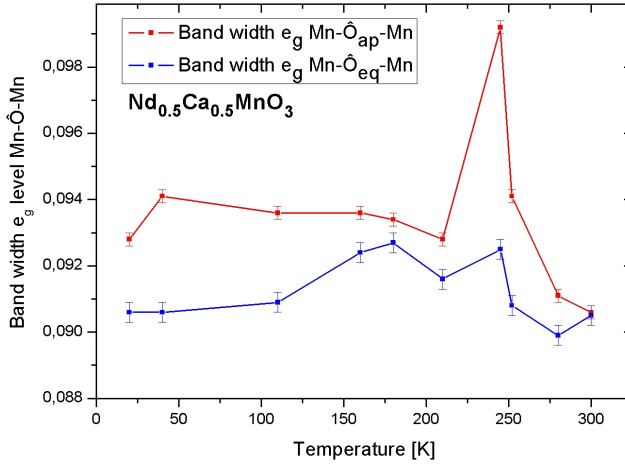


Figure 3.9: Bandwidth of e_g -Mn calculated for $\text{Nd}_{0.5}\text{Ca}_{0.5}\text{MnO}_3$ on the basis of eq.(1.1).

and Nd compounds. We report in figure 3.11 cell parameters, Jahn-Teller factor, tilting effect and the bandwidth for $\text{Lu}_{0.5}\text{Ca}_{0.5}\text{MnO}_3$. Because NPD spectra were acquired in the range $20 < T < 300$ K and T_{CO} is at $T = 530$ K, we can observe only the beginning of the changes in all structural parameters.

For all samples the magnetic peaks at low temperature $T < 100$ K have been associated with the *pseudo*-CE-type AFM structure. The ordered moments reported in figure 3.10 are well below the expected values for perfectly ordered moments which are $4 \mu_B$ and $3 \mu_B$ for Mn^{3+} and Mn^{4+} , respectively. This is due to out-of-plane components of the magnetic moments present in this structure.

In particular, in the xy -plane the Mn ions are ferromagnetically coupled following a zigzag line, with FM-coupled zig-zag AFM chains running along the x or y axes. The main difference between the CE-type and *pseudo*-CE-type magnetic structure is the way in which the layers are coupled along the z -direction: the coupling is AFM in the CE structure and FM in the *pseudo*-CE structure. Following the Goodenough model [5], the orbital ordering is the same for the two structures (CE and *pseudo*-CE) in the xy -plane, but the *pseudo*-CE accommodates a significant number of long Mn-O bonds directed along the z axis, yielding a net FM interlayer

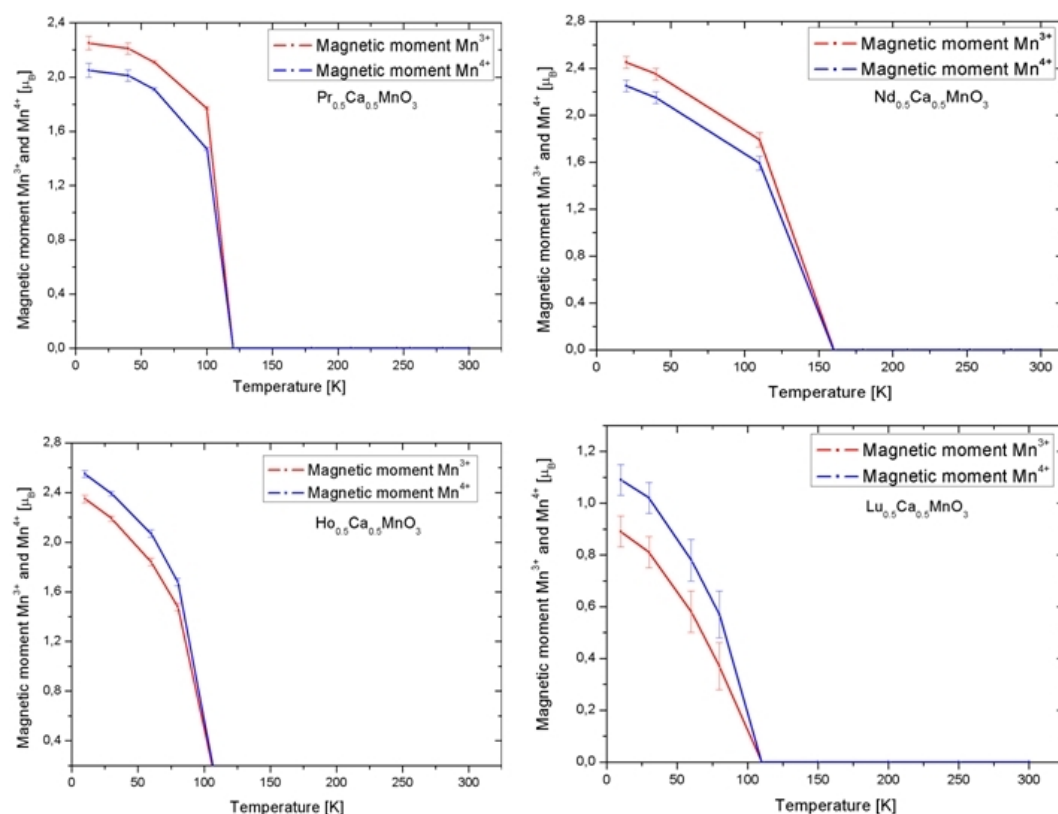


Figure 3.10: Magnetic moment Mn^{3+} and Mn^{4+} as a function of temperature for $\text{Ln}_{0.5}\text{Ca}_{0.5}\text{MnO}_3$, where $\text{Ln} = \text{Pr}, \text{Nd}, \text{Ho}$ and Lu .

coupling. Therefore, the FM super-exchange interactions between $\text{Mn}^{3+}/\text{Mn}^{4+}$ compete with the AFM interactions between $\text{Mn}^{3+}/\text{Mn}^{3+}$ and $\text{Mn}^{4+}/\text{Mn}^{4+}$ pairs, which form the layers of ideal charge order. This competition gives the *canting* of the *pseudo-CE* magnetic structure.

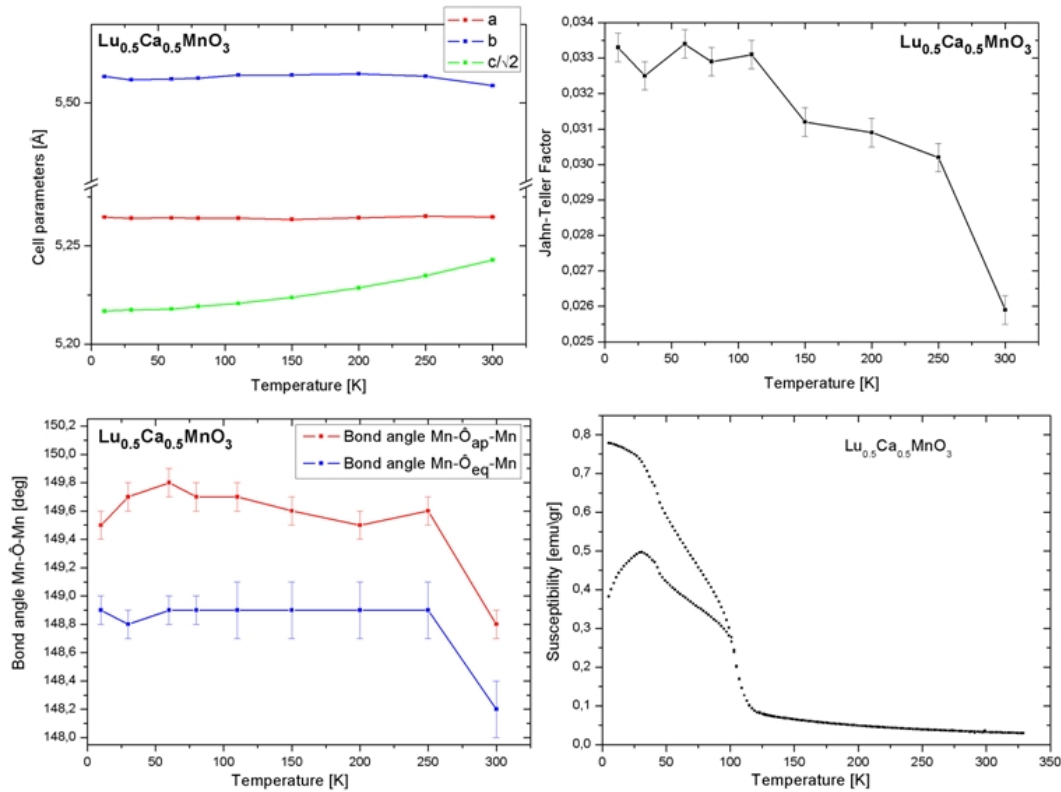


Figure 3.11: Cell parameters, Jahn-Teller effect, Mn-O-Mn bond angles and susceptibility of $\text{Lu}_{0.5}\text{Ca}_{0.5}\text{MnO}_3$.

3.4 Systematic study as a function of Ln ionic radius

In this section, we studied the effect of radius size of the lanthanide on the magnetic interactions and on the localized nature (or not) of the charges.

We report also the data of $\text{La}_{0.5}\text{Ca}_{0.5}\text{MnO}_3$ studied by Radaelli et al. [28] to complete the series. In figure 3.12, we report all parameters as a function of Ln ionic radius at room temperature. A continuous change with ionic radius is observed for all parameters. The sensitivity that these compounds display for small changes in lanthanide radius is generally attributed to the increasing of the tilting in MnO_6 octahedra as the radius decreases. The octahedra remain essentially rigid while the Mn-O-Mn angles distort [74]. The nearest neighbor Ca-O distances decrease without perturbing Mn-O distances. So the structure optimizes the ionic Ca-O bonding without diminishing the more strongly covalent Mn-O bonding.

Decreasing Ln radius leads to a decrease in the Mn-O-Mn angle, see figure 3.12,

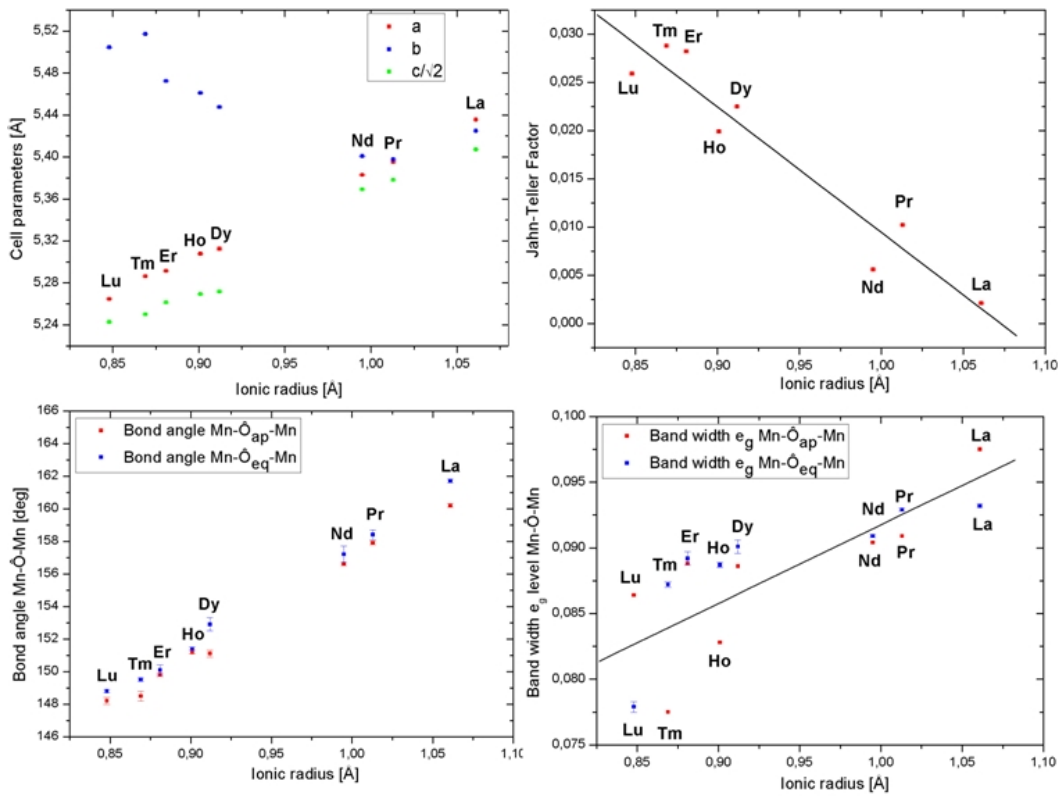


Figure 3.12: Cell parameters, Jahn-Teller distortion and tilting effect as a function of lanthanide ionic radius, at room temperature.

that corresponds to a decreasing of the spatial overlap on the Mn- e_g and O-2p σ orbitals with the consequence that σ^* bandwidth is reduced. Decreasing of the bandwidth reduces the carrier mobility, encouraging carrier localization, which stabilises orbital and charge ordering.

The Mn-O_{eq}-Mn angles are consistently larger than their Mn-O_{ap}-Mn. So that, the σ^* bandwidth Mn-O_{eq}-Mn layers is larger than the bandwidth in apical direction, which increases in plane carrier mobility and magnetic super exchange interaction. The Mn-O_{eq} layers is preferentially populated compared to the e_g orbitals directed along the apical direction, which results in an expansion of the Mn-O_{eq} bonds with the respect to the Mn-O_{ap} bonds.

We underline that this model is not valid for the extremes of the series, La [28] and Lu compound, because for these two samples the apical bandwidth is considerably bigger than to the equatorial one. That is probably due to the fact their f shells are completely full. (Figure 3.13 study of the effect of Ln magnetic moment on the results.)

In the analysis of the magnetic moment as a function of Ln ionic radius at the lowest temperatures reached, we considered the percentage variation of the magnetic moments associate to Mn^{3+} - Mn^{4+} as a function of Ln ionic radius contraction, see figure 3.13. We can note in this picture that changing the radius, this percentage follows a discontinuous curve. In particular, at the extremes of the series (La, Lu compounds), we found the highest percentage variation of the moments and for the other compounds the values seem to be distributed in groups. This fact suggests that perturbative effects like crystal field on the $4f$ orbitals of the lanthanides occur. Classical calculations of the energy levels of the $4f$ electronic configurations could be part of a feature work on this subject.

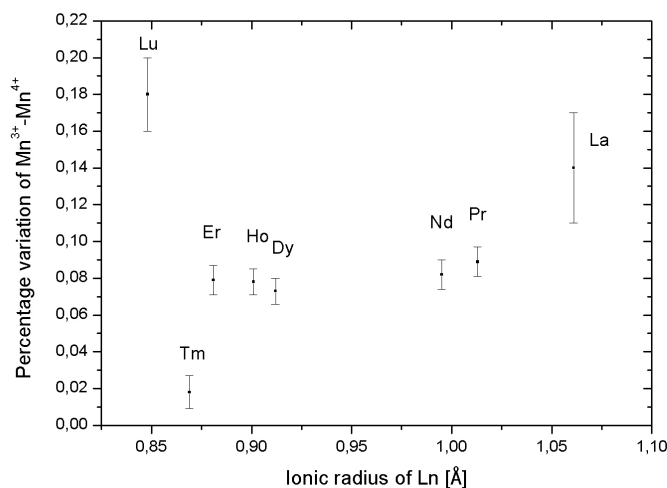


Figure 3.13: Percentage variation of the magnetic moments associate to Mn^{3+} - Mn^{4+} as a function of Ln ionic radius at lowest temperature. The percentage variation of the magnetic moments for the LaCa compounds is obtained by Radaelli et al. [28].

3.5 Conclusions

In this chapter, we have reported the structural and magnetic results coming from macroscopic magnetic measurements and from NPD.

Macroscopic magnetic measurements of susceptibility in the range $5 \div 530$ K, allowed us to determine the nature of the magnetic correlations at above and under T_{CO} , in the framework of Zener polarons model.

The inverse of susceptibility follows a Curie behavior above T_{CO} associated with FM correlations with enhancement of double exchange. Below T_{CO} , there is a region where the inverse susceptibility follows a Curie-Weiss law associated with AFM correlations (with an augmentation of super exchange). In the hypothesis of presence of Zener polarons the change of paramagnetic state above and below T_{CO} is explained by the change of these elementary magnetic units.

Finally, below ~ 150 K, the long range AFM correlations take place and we distinguish two magnetic sublattices corresponding to the moments associated to Mn^{3+} and Mn^{4+} ions.

We have investigated the nuclear and magnetic structure of the samples containing Pr, Nd, Dy, Ho, Er, Tm and Lu by NPD measurements as a function of temperature ($10 \div 300$ K) and we analysed the effect of the change of ionic radius on the magnetic correlations.

From Rietveld method we have determined: cell parameters, volume cell, atomic coordinates, bond lengths and angles, magnetic structure as a function of temperature and Ln ionic radius. Furthermore, we have analysed the Jahn-Teller, tilting effects and the bandwidth of e_g -Mn.

In literature a complete description of the nuclear and magnetic structure is available only for the Pr and Nd compounds. For the other compounds of the series, measurements were published for the nuclear structure at high temperature but the coordinates were not reported.

For all samples, we have found a $Pbnm$ symmetry group overall temperature region explored, with a Jahn-Teller distortion a compression in z-direction. We do not have structural phase transition as reported by other groups for Pr compounds with composition close to 0.5.

A strong anomaly of all these parameters is observed at T_{CO} . At this temperature the bandwidth in the xy-plane is smaller than the bandwidth in the z-direction, that can be interpreted as a reduction the carrier mobility in the xy-plane. Below T_{CO} , the bandwidth decrease corresponds to a localization of the carriers which stabilises

orbital and charge ordering.

Below ~ 150 K four magnetic peaks arise at the low angle region (as an example, see fig. 3.4 at 10 K and fig. 3.10) with moments described in two sublattices having two different propagation vectors for Mn^{3+} and Mn^{4+} . The description corresponds to the *pseudo*-CE model with the canting of the magnetic moments for all our samples. With these results we complete the description in the phase diagram of half-doped family Ln/Ca.

Although, the series as a function of Ln radius is not complete we have enough samples to study the changes of all parameters (cell parameters, JT, etc...) with the Ln radius. The changes are continuous and smooth except for the percentage different between Mn^{4+} - Mn^{3+} moments. This percentage follows a discontinuous curve. In particular, at the extremes of the series (La, Lu compounds), we found the highest percentage variation of the moments and for the other compounds the values seem to be distributed in groups. This fact suggests that perturbative effects like cristal field on the 4f orbitals of the lanthanides occur.

In the following two chapters we will present electronic structure calculations to investigate these experimental results.

Conclusions

Dans ce chapitre, nous avons introduit les résultats des expériences de structure et de magnétisme réalisés par des mesures de magnétisme macroscopique et par diffraction de neutron sur poudre. Les expériences de magnétisme macroscopique, réalisées dans un intervalle de température de 5 à 530 K, nous ont permis de déterminer la nature des corrélations magnétiques en dessus et en dessous de la température de l'ordre de charge (T_{CO}) dans le contexte du modèle des polarons introduit par Zener. En dessus de T_{CO} , l'inverse de la susceptibilité suit la loi de Curie avec des corrélations ferromagnétiques et des interactions dues au double-échange. En dessous de T_{CO} , nous avons pu observer une région où l'inverse de la susceptibilité suit une loi de Curie-Weiss avec des corrélations antiferromagnétiques et une augmentation des interactions de super-échange. Dans l'hypothèse de la présence de polarons de Zener, le changement de l'état paramagnétique en proximité de T_{CO} s'explique par la modification des unités magnétiques.

Enfin, en-dessous de 150 K, les corrélations antiferromagnétiques à longue portée deviennent dominantes et on peut distinguer deux sous-mailles magnétiques correspondant aux moments associés aux ions Mn^{3+} and Mn^{4+} .

Nous avons ensuite étudié les structures nucléaires et magnétiques des échantillons contenant les lanthanides Pr, Nd, Dy, Ho, Er, Tm et Lu par DNP en fonction de la température (10 ÷ 300 K) et nous avons analysé l'influence du rayon ionique sur les corrélations magnétiques.

Les paramètres suivants ont été déterminés par la méthode de Rietveld en fonction de la température et du rayon ionique du lanthanide : paramètres de maille, le volume de la maille, les coordonnées atomiques, les longueurs et les angles de liaisons et la structure magnétique. Nous avons également analysé l'effet de Jahn-Teller, l'effet de tilt et la longueur de bande de e_g -Mn.

A ce jour, seuls les composés à base de Pr et Nd ont été décrits de manière complète dans la littérature. Pour les autres composés de la série, la structure nucléaire a été résolue à haute température mais les coordonnées atomiques ne sont pas disponibles.

Pour tous les échantillons, nous avons trouvé un groupe d'espace de type $Pbnm$ sur toute la gamme de température explorée avec une distorsion de Jahn-Teller et une compression dans la direction z .

Tous ces paramètres présentent une anomalie notable à T_{CO} , comme, par exemple, la longueur de bande dans le plan xy qui est plus petite que celle le long de l'axe

z. Ceci peut être interprété par une diminution de la mobilité des porteurs de charge dans le plan xy. Au dessous de T_{CO} , la diminution de la longueur de bande correspond à une localisation des charges qui stabilise l'ordre orbital et l'ordre de charge.

En dessous de 150 K, nous avons remarqué l'apparition de quatre pics magnétiques à petits angles (fig. 3.4 à 10 K et fig. 3.10) avec des moments magnétiques décrits par deux sous-mailles avec deux vecteurs de propagation différents pour Mn^{3+} and Mn^{4+} . Ceci est décrit par le modèle *pseudo*-CE avec le canting du moment magnétique pour tous les échantillons. L'ensemble de ces résultats nous a permis d'obtenir une description complète du diagramme de phase de la famille des Ln/Ca half-doped.

Cette étude nous a permis d'évaluer les changements des paramètres mentionnés précédemment (paramètres de mailles, distorsion de Jahn-Teller, etc...) en fonction du rayon du lanthanide pour la majorité des lanthanides de la série. Ces paramètres présentent une variation continue à l'exception du pourcentage de variation du moment magnétique entre Mn^{4+} et Mn^{3+} pour lequel la variation présente une discontinuité marquée. Pour ce paramètre, la différence maximale a été observée pour les composants comportant les lanthanides aux extrêmes de la série (La et Lu). Pour les autres membres de la série, nous avons pu observer la présence de groupes présentant une différence similaire. Ceci nous amène à penser que les effets perturbatifs du champ cristallin pourraient affecter les orbitales 4f.

4 *Méthodes de simulation: théorie et pratique*

Dans ce chapitre, les méthodes de simulation utilisées pour modéliser la série des $\text{Ln}_{0.5}\text{Ca}_{0.5}\text{MnO}_3$ sont présentées.

Pour l'étude de tels systèmes, nous avons eu recours à des méthodes dites ab-initio basées sur la résolution de l'équation de Schrödinger appliquée aux électrons du système pour obtenir des propriétés intrinsèques de ces matériaux.

La théorie DFT est présentée à travers les théorèmes de Hohenberg-Kohn et les équations de Kohn-Sham et une discussion à propos de l'interprétation de l'énergie d'échange-corrélation et des approximations nécessaires à son estimation. Tous les calculs ont été réalisés à l'aide du programme VASP [75] avec des pseudopotentiels PAW [76]. Une description succincte des fichiers d'entrée et de sortie de ce programme est présentée en fin de chapitre.

4

Computational methods: theory and practice

We have studied the manganites extensively from an experimental point of view, but the complexity of their physical properties across the phase diagram has pushed a strong development of theories, including the use of numerical methods and modelling, to explain these properties. In this chapter, the computational methods used to model the $\text{Ln}_{0.5}\text{Ca}_{0.5}\text{MnO}_3$ series are presented.

The work has been performed at the quantum-mechanical level, in the sense that the characteristics of materials are derived from the results obtained by solving an approximated Schrödinger equation for the electrons of the system under study. For physical properties, the valence electrons are particularly important. Since the core electrons are strongly bound to the atomic nuclei, it is the valence electrons that have the freedom necessary to create bonds with neighbouring atoms, thus being predominantly responsible for the stability and structure of any atomic aggregate, particularly crystalline solids in the context of this thesis.

It is therefore interesting to solve Schrödinger's equation for the valence electrons, moving in an *external potential* (the potential exerted on them by the atomic nuclei, including the core electrons, and possible external fields). However, a complete, exact solution is practically impossible. Various approximation schemes have to be adopted, in such a way that sufficient approximations are introduced to make the problem tractable, but without losing the key physics and the accuracy needed for the desired goal.

Many approximate methods for solving the Schrödinger's equation have been devised during the now century-long history of quantum mechanics, some more accurate but computationally expensive, others less accurate but quicker to evaluate. First of all, in this work, the time-independent Schrödinger's equation is

used because we have studied ground state properties and not the excited state properties.

In this context, the next approximation consists of separating the nuclear and electronic degrees of freedom in two components. It is known as the Born-Oppenheimer approximation [77] which, in a dynamical sense, allows a clear separation of time scales between the electronic and nuclear motions, since the electrons are lighter than the nuclei by three orders of magnitude. Considering the ensemble of nuclei as fixed point charges, it is possible to solve the Schrödinger's equation for the electronics in the static electric potential arising from the nuclei in that particular arrangement. Now, the electron-electron interactions must be considered which is a many-electron problem. Electron-electron repulsions are critically important and must be included in any accurate electronic structure treatment, as in the Hartree-Fock method [78], where the wavefunction relative to the electron-electron repulsion is treated in an 'average' field. Each electron is considered to be moving in the electrostatic field of the nuclei and the average field of the other $n-1$ electrons. The Hartree-Fock approach is a first principles or *ab initio* method.

First-principles methods like Hartree-Fock [78] or density-functional theory (DFT) [79, 80], do not depend on any input data other than the atomic positions and atomic numbers. They thus solve Schrödinger's equation, in suitably approximated forms, without any further assumptions. Of course, first-principles methods are computationally more demanding, but yield results that are more reliable and of higher predictive power.

During the last thirty years, a dramatic step forward has taken place in the development and applicability of first-principles methods, arising from the powerful combination of three separate developments. First, the formulation of density-functional theory (DFT) by Kohn, Hohenberg and Sham in the 1960's [81, 82] provided a theoretical point of view from which to approach the many particle problem of electrons moving in an external potential in a very efficient way. Second, the rapid development of computer technology has provided the means with which these theories, still requiring an impressive computational power, can be applied in practice. Third, there has been a strong development in computational algorithms.

In the first section of this chapter, density-functional theory is reviewed: the Hohenberg-Kohn theorems and the Kohn-Sham equations are presented, the interpretation of the exchange-correlation energy in terms of the exchange-correlation

hole is discussed, and approximate forms for the exchange-correlation energy are presented.

4.1 First principle

The world around us is mostly made of condensed matter, i.e. matter whose energy is low enough that it has condensed to form stable systems of atoms and molecules, in solid or liquid phases. The large variety of ways in which these systems can take form leads to a rich diversity of physical phenomena. Therefore, approaching the field of condensed matter physics from a theoretical or computational angle can be a very challenging task. For the most part, the way this is done is to pick a particular macroscopic phenomenon, which has been well studied experimentally, and to build empirical, or semi-empirical, models to describe the experimentally observed results.

This often provides a good understanding of the physics of the system under study, and it is often possible to interpolate or extrapolate these models in order to predict the behaviour of related systems under conditions not yet tested experimentally. However, due to the complexity of condensed matter systems, and the difficulty in building accurate models, the predictive power of such an approach can be severely limited. The first principles approach to condensed matter theory is entirely different from this point of view.

The first principles approach starts from what we know about all condensed matter systems - that they are made of atoms, which in turn are made of a positively charged nucleus, and a number of negatively charged electrons. The interactions between atoms, such as chemical bonding, are determined by the interactions of their constituent electrons and nuclei. All of the physics of condensed matter systems arises ultimately from these basic interactions. If we can model these interactions accurately, then all of the complex physical phenomena that arise from them should emerge naturally in our calculations. The physics that describes the interaction of electrons and nuclei that is relevant to most problems in condensed matter is actually relatively simple. There are only two different types of particle involved, and the behaviour of these particles is mostly governed by basic quantum mechanics. What makes first principles calculations difficult is not so much the complexity of the physics, but rather the size of the problem in terms of its numerical formulation.

We performed our calculations, for this work, using density functional theory, as used for similar compounds in literature [12, 11, 13, 83], because DFT can describe this type of system adequately, including electron correlations.

4.2 Density functional theory

As stated above, calculations aim at solving the stationary Schrödinger equation for the many-particle problem of a general system of N electrons moving in an external potential. To apply Schrödinger's equation to a system of many atoms requires several approximations. The most common approximation is known as the *Born-Oppenheimer* [77], which allows the dynamics of the electrons and much heavier nuclei to be decoupled. In this case, the electrons are treated within a quantum approach and the nuclei can be treated classically. The energy of the system becomes:

$$E = E_{core}[R_a] + E_{e-} \quad (4.1)$$

and it depends of the atomic positions R_a . The energy of a system with N electrons is represented by the ground state solution of the Schrödinger Equation:

$$H[R]\Psi = E\Psi \quad (4.2)$$

and the electronic properties of the system are described by the wavefunction of the ground state $\Psi(r_1, r_2, \dots, r_N)$, which should be antisymmetric with respect to the exchange of two electrons according to the Pauli exclusion principle. The Hamiltonian H of a system with N electrons contains the kinetic term and Coulomb's interaction term (for two-body model), and the external potential V_{ext} , representing the interaction of the electrons with the cores:

$$H = \sum_{i=1}^N -\frac{1}{2}\nabla_{r_i}^2 + V_{ext}(r_i, R) + \frac{1}{2} \sum_{i \neq j} \frac{1}{|r_i - r_j|} \quad (4.3)$$

Approximations allow to reduce the complexity of solving Schrödinger's equation. The approximations can be divided into two classes. The first results from quantum chemistry and uses exact the Hamiltonian H for electron exchange, based on antisymmetrised, many electron wavefunctions. The most famous approach in this class is the Hartree-Fock method [84], which is based on the wavefunction of a many-body system in the form of a single Slater determinant (a matrix notation, which fulfilled anti-symmetry and *Pauli exclusion principle*).

The second class of quantum methods is based on the Kohn-Sham equation and is embodied in density functional theory (DFT) [85]. In this case the knowledge of electronic density is enough to determine the energy of the ground state system of interacting electrons. The ground state energy of the electron system in an external

potential is a functional of the electron density.

The fundamental theorem underpinning DFT was formulated by Hohenberg and Kohn in 1964 [81]: **Hohenberg-Kohn Theorem**. The electronic density of the ground state determines only (except for an additive constant) the external potential of the Hamiltonian's system. According to this theorem, there is a unique correspondence between the external potential of the system and its electronic density $\rho(R)$ with the ground state. The form of the external potential is sufficient to determine $\rho(R)$. Given that:

$$\rho(R) = N \int dr_2 \cdots dr_N \psi^*(r, r_2, \cdots, r_N) \psi(r, r_2, \cdots, r_N) \quad (4.4)$$

the electronic energy of system can be written in the form:

$$E = \min_{\psi^* \psi = \rho} \int dr_2 \cdots dr_N \psi^*(r, r_2, \cdots, r_N) \times \\ \times \left[-\frac{1}{2} \sum_{i=1}^N \nabla_{r_i}^2 = 1 + \frac{1}{2} \sum_{i \neq j}^N \frac{1}{|r_i - r_j|} \right] \psi(r, r_2, \cdots, r_N) + \int dr V_{ext}(r) \rho(r) = E[\rho] \quad (4.5)$$

This equation shows that the energy is a functional of the electronic. To make available this approach from a computational point of view, the **Kohn-Sham Theorem** is necessary, formulated in 1965 [82]:

*Any electronic density which is the ground state of an interacting electrons system is also the solution of a not interacting electrons system subjected to an effective potential called **Kohn-Sham potential**.*

This theorem makes it possible, now, to have a simpler system of equations describing individual electrons in a mean field. The remaining difficulty is to determinate the Kohn-Sham potential. The Kohn-Sham formalism consists of finding a system of $N/2$ orthonormal functions $\Psi_i(r)$ which minimizes the following energy functional:

$$E = -\frac{1}{2} \sum_{i=1}^{N/2} \int \Psi_i^*(r) \nabla^2 \Psi_i(r) dr + \frac{1}{2} \int \rho(r) V_H dr + \int V_{ext}(r) \rho(r) dr + E_{ex}[\rho(r)], \quad (4.6)$$

where ρ is the electronic density of a system of non-interacting electrons, $V_{ext}(R)$ is an external potential due to the nuclei (or cores), $V_H(R)$ is the Hartree potential,

representing the Coulomb interaction of the system of electrons and E_{xc} is the exchange-correlation energy of the electrons:

$$\rho(r) = 2 \sum_{i=r}^{N/2} \Psi_i^*(r) \Psi_i(r) \quad \nabla^2 V_H(r) = -4\pi\rho(r). \quad (4.7)$$

Note that the terms in the total energy equations above, and therefore the corresponding Schrödinger equations, depend on the electron density, which is constructed from the wavefunctions that are the solutions of the Schrödinger equation. This equation therefore has to be solved self-consistently, that is until the output wavefunctions are the same as the input wavefunctions, within a given tolerance.

4.2.1 Exchange-correlation functional

Following Hohenberg-Kohn and Kohn-Sham theorems, the solution of Schrödinger's equation of a system with N electrons is thus expressed in term of a system of N independent particles subjected to an external potential and an exchange-correlation potential. The formal definition of this exchange-correlation potential is given by the equation:

$$\begin{aligned} E_{xc}[\rho(r)] = \int dr V_{xc}(r) \rho(r) = \min_{\Psi^* \Psi = \rho} & \left\{ \int dr_2 \cdots dr_N \Psi^*(r, r_2, \cdots, r_N) \times \right. \\ & \times \left[-\frac{1}{2} \sum_{i=1}^N \nabla_{r_i}^2 + \frac{1}{2} \sum_{i \neq j} \frac{1}{|r_i - r_j|} \right] \times \Psi(r, r_2, \cdots, r_N) \\ & \left. - \left\{ -\frac{1}{2} \sum_{i=1}^{N/2} \int \Psi_i^*(r) \nabla^2 \Psi_i(r) dr + \frac{1}{2} \int \rho(r) V_H(r) dr \right\} \right\} \quad (4.8) \end{aligned}$$

In words, it expresses the difference between the system of interacting electrons and the system of non-interacting electrons. It contains information on the energy due to correlation and exchange of electrons, hence its name. Note that electron exchange is described exactly in the Hartree-Fock approach but electron correlation effects have to be included in post Hartree-Fock corrections. The Kohn-Sham wavefunctions, therefore, must be the first $N/2$ energy functions of the following Schrödinger's equation:

$$H_{KS} \Psi_i = \epsilon_i \Psi_i \quad (4.9)$$

$$H_{KS} = \left(\frac{1}{2} \nabla^2 + V_H[\rho] + V_{xc} + V_{ext} \right). \quad (4.10)$$

And the total energy of the system will be given by the sum over the corresponding eigenvalues.

It should be noted that, if one knows the complete form of the exchange-correlation potential, the solution of the Kohn-Sham problem gives the exact energy of the electronic system, the density ρ corresponding exactly to the ground state, electronic density of the system. The Kohn-Sham wavefunctions $\Psi_i(r)$ are not associated to any physical quantities, they must be regarded as auxiliary functions required to solve Schrödinger's equation. Unfortunately, the explicit form of the exchange-correlation functional is not known. There are various approximations for the exchange-correlation energy $E_{xc}[\rho(r)]$, for example the LDA (local density approximation). This approximation consists of considering the exchange-correlation energy of a homogeneous gas of electrons that has a density $[\rho(r)]$ in each point of space. This approximation is quite simple, but it describes very well the physical properties of many systems. Another possible class of approximations, widely used in the last years, is represented by extensions called GGA (Generalized Gradient Approximation), where the exchange-correlation functional also depends on the gradient of the electronic density. Of the various existing GGA, the GGA-PBE (Perdew, Burke and Ernzerhof) [86] is widely used.

4.2.2 Pseudo-potential Approximation

The electrons sensitive to the environment around the atom and thus taking part in, for example, chemical bonds are the peripheral electrons, which are called the valence electrons. The others, named core electrons, are not very sensitive to the environment of the atom. A widely-used approximation thus consists of taking into account only the valence electrons, leaving the configuration of the core electrons 'frozen'. This reduces considerably the number of electrons to consider at the possible expense of not taking into account the influence of the core electrons. In order to separate valence and core electrons, a modified electron-ion potential is required in the Kohn-Sham Hamiltonian. The *pseudopotential* [24] takes into account the influence of the core electrons on the valence electron interaction with the nuclei. This potential is not local any more because the influence of the core electrons on the system is that of a diffuse potential with spherical symmetry. This kind of approximation is very reasonable and reduces the complexity of the problem considerably. Moreover, the approximation of the pseudopotential is less strong than the approximation induced by the exchange-correlation functional.

The pseudopotentials eliminate the 'fast variations' from the wavefunctions of the valence electrons close to the cores which are imposed by the constraints of orthonormalisation with the wavefunctions of the core electrons (see figure 4.1). This is critical in the case of a numerical implementation because it reduces considerably the number of basis functions required to express the electronic properties of the system.

Several kinds of pseudopotentials exist, and they can be classified according to

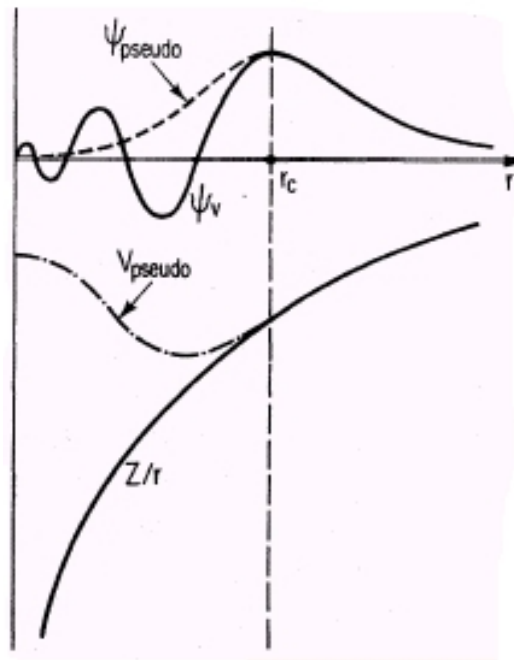


Figure 4.1: Schematic illustration of the potential and the wavefunction to any electrons (solid lines), and the pseudopotential and pseudofunction respectively (drawn lines). The values of two curves intersection is r_c [87].

their properties. Norm-conserving pseudopotentials connect the wavefunctions for electrons with the pseudofunction:

$$\int_0^{r_c} dr |\Psi_{ae}(r)|^2 = \int_0^{r_c} dr |\Psi_{ps}(r)|^2 \quad (4.11)$$

$$\Psi_{ae}(r) = \Psi_{ps}(r) \quad |r| > r_c. \quad (4.12)$$

Where r_c is the cut-off radius between the core and valence regions. Equation 4.11 expresses the norm-conserving condition. This kind of pseudopotential is normally more precise but requires a large basis set and is therefore computationally demanding. Smaller basis sets can be used by relaxing the norm-conserving condition

for individual wavefunctions and replacing it by a generalised orthonormality condition. This is the principle underlying ultra-soft pseudopotentials. A further development of the ultra-soft approach has produced PAW pseudopotentials, which combine the accuracy of norm-conserving pseudopotentials, and even all-electron calculations, with the requirement of small basis sets for computational efficiency (see below).

4.2.3 Projected Augmented Waves Approximation

In this thesis, all the electronic structure calculations and geometry optimizations have been performed using the projector augmented wave (PAW) method [76]. The PAW method is an all-electron frozen core method, which combines the features of both the ultra-soft pseudopotentials and augmented plane wave methods. Following the latter, the wavefunctions have a dual representation: within spheres centered on each atomic position (the augmentation region) the wavefunctions are expanded by partial-waves and, outside the core, they are expanded into plane waves or some other convenient basis set. The PAW method is based on the linear transformation that relates the set of valence all-electron functions Ψ_q to the smooth functions $\tilde{\Psi}_q$, which is given by:

$$|\Psi_q\rangle = \tau |\tilde{\Psi}_q\rangle \quad (4.13)$$

The requirement that the transformation is linear leads to the following form for the operator τ :

$$\tau = \hat{1} + \sum_i (|\phi_i\rangle - |\tilde{\phi}_i\rangle) \langle \tilde{p}_i | \quad (4.14)$$

and therefore the all-electron eigenstate can be written as:

$$|\Psi_q\rangle = |\tilde{\Psi}_q\rangle + \sum_i (|\phi_i\rangle - |\tilde{\phi}_i\rangle) \langle \tilde{p}_i | \tilde{\Psi}_q \rangle \quad (4.15)$$

The ϕ_i is the all-electron partial wave, which is the solution of the radial Schrödinger equation for the isolated atom. Therefore, the index i refers to the atomic site R , the angular momentum quantum numbers $L = l, m$ and an additional index s referring to the reference energy.

4.2.4 LDA and GGA approximations

The local density approximation (LDA) [88] is quite simple. It assumes that the exchange-correlation energy at a given point is equivalent to that of a homogeneous electron gas having the same electron density. The exchange-correlation energy of the homogeneous electron gas has been calculated by Ceperley and Alder [89] for different electron densities. This data has been used by Perdew and Zunger [90] to parameterize a LDA exchange-correlation energy density as a function of the electron density which is widely used. The LDA exchange-correlation energy is then the expectation value of the exchange correlation function, weighted by the electron density:

$$E_{xc}^{LDA}[n] = \int n(r) \epsilon_{xc}^{LDA}(r) dr, \quad (4.16)$$

To treat magnetic materials, the spin-polarization of the material has to be taken into account. This can be achieved by using the Local Spin Density approximation (LSDA) [91], where the electron density is divided into a spin-up and a spin-down electron density. It is precisely the exchange-correlation potential that causes the difference between the two electron densities. The total electron density is the sum of the two densities,

$$n(r) = n_{\uparrow}(r) + n_{\downarrow}(r) \quad (4.17)$$

The magnetization or the spin-polarization, is the weighted difference between the majority and minority spin contributions. The LDA or LSDA (Local Spin Density Approximation) works well for slowly varying electron densities, for instance in bulk materials.

A natural way to improve the LDA is to consider the exchange-correlation energy depending on the density $n(r)$ and also on its gradient $\nabla n(r)$. This is implemented through an approach called generalized gradient approximation (GGA) which can include spin-polarization (s-GGA). The most widely used parametrization for the GGA-functional are those obtained by Becke [88], by Perdew and Wang (PW91) [92], by Perdew, Burke and Enzerhof (PBE) [86].

4.2.5 The Hubbard model: GGA+U

Metallic behavior occurs because electrons save kinetic energy by being delocalized over the whole of a crystal [93]. In some systems the Coulomb energy per site

(i.e. two electrons on the same lattice site) is so strong that electrons cannot move freely through the crystal. The high energetic cost of double occupancy of a site means that the metallic behavior breaks down.

The DFT-GGA-PBE method, widely used in the band structure calculations, is not suited to study systems with strong electron correlation effects because the local density functional does not incorporate the strong on-site Coulomb interaction. As a result the band gap tends to be underestimated and insulators or semi-conductors become metals. Within LDA and GGA approximations, an additional correction term has been introduced in order to account for the strong on-site Coulomb interaction, U , which is considered as source of the strong electron correlation. This correction gave rise to the method denoted as GGA+ U (generalized gradient approximation + Hubbard correction) [94, 95, 96]. Within GGA+ U the electron system is separated into two subsystems, localized d (or f) electrons for which the Coulomb d - d (f - f) interactions are accounted for by the term U , and delocalized s , p electrons, described by the orbital-independent one-electron potential in GGA.

Although DFT has been considered as a method with a complete absence of adjustable parameters, the values for U often vary significantly in different studies on the same compound. The U term expresses the strength of the Coulomb interactions and determines the extent of the localization of the electrons, therefore the use of U with different magnitudes for the same compound results in a sort of classification of the compound according to its electron correlation effects.

4.2.6 DFT in practice: VASP

We employed, in this work, the Vienna ab initio simulation package (VASP) [97], with the following options:

- GGA functional with parametrization given by Perdew-Burke-Ernzerhof (PBE).
- Projector augmented wave (PAW) pseudopotential method.
- Hubbard correction giving an effective on-site Coulomb potential for the d -states for Mn atoms.

In order to perform our calculations, the VASP code needs four input files:

POSCAR: A file containing the atomic coordinates describing the geometry of the system.

POTCAR: A file describing the pseudopotential and electronic configuration (core and valence electrons) and, in the case of VASP, the functional i.e. GGA-PBE. For any atom there is a choice of pseudopotentials which concerns mainly the number

of plane waves and the number of electrons to be treated in the calculation. For the Lanthanides, a set of pseudopotentials exists specifically for the case of an oxidation state 3+, of relevance here, in which three (otherwise) valence electrons are included in the core, helping electronic convergence. The plane-wave energy cut-off is one of two convergence criteria in a plane wave calculation. There is a choice of ultrasoft or PAW pseudopotentials, the latter being used here.

KPOINTS: Part of the DFT calculation is performed in reciprocal space which therefore has to be sampled on a finite mesh described by this file. The density of k-points is the second convergence criterion in a plane wave calculation.

INCAR: An input file determining the kind of job which VASP will perform e.g. single point energy calculation, geometry optimisation, spin polarised calculation, etc.

We report a typical INCAR file used to perform geometry optimisation:

```
NELMIN = 4    (minimum number of electronic self-consistent step);
EDIFF = 1E-5  (break condition for the electronic self-consistent loop in eV);
NSW = 30     (maximum number of ionic steps i.e. upto 30 ionic configurations
will be produced during a geometry optimisation );
EDIFFG = -1E-3 (break condition for the ionic relaxation loop in eV/A);
IBRION = 1    (minimisation method, good close to minimum ground state
configuration of the ions);
ISIF = 3     (atomic coordinate and cell parameter optimisation);
LREAL = A    (determines whether the projection operators are evaluated in
real-space or in reciprocal space);
ISMEAR = 0   (determines how the partial occupancies at the Fermi level  $f_{nk}$  are
set for each orbital);
SIGMA = 0.01 (in eV, width relating to smearing, above);
ISPIN = 2    (spin polarized calculations are performed);
MAGMOM =     (list of initial magnetic moments);
LORBIT = 11  (determines information content of output files, for example
magnetic moments, site projected electronic density of states, etc);
LDAU = .TRUE.
```

VASP produces many files. The following have been of particular use:
OUTCAR: contains all output from a VASP calculation, including, for example, partial charges and magnetic moments (depending on the value of LORBIT, above) and total energies, forces on atoms and stress tensors during geometry optimisation

calculations.

OSZICAR: gives a summary of the self-consistent electronic cycles and ionic cycles.

CONTCAR: contains the final, output structure, for example, after geometry optimisation.

XDATCAR: contains the series of structures from a geometry optimisation.

DOSCAR: contains the electronic density of states, including site and orbital projections, depending on the value of LORBIT, above.

CHGCAR: contains the real space electron density, separated into spin up and down parts, allowing charge and spin density to be visualised.

All calculations were performed on clusters at ILL using version 4.6 of VASP, compiled using the Portland Group compilers with MPI for parallel execution. Up to 16 cores were used in any one calculation.

In the next chapter, the results of the VASP calculations on half-doped managanites are presented.

5 Résultats des simulations

Ce chapitre présente les résultats ab-initio des calculs sur les manganites pures et semi-dopés. Ces calculs ont été réalisés pour confirmer (ou infirmer) des résultats expérimentaux et, réciproquement, pour voir dans quelle mesure les calculs ab-initio peuvent reproduire des propriétés physiques complexes. Ceci permettant alors d'obtenir une meilleure compréhension des résultats expérimentaux par l'intermédiaire de grandeurs aisément accessibles par la simulation telles que la densité d'états électronique (DOS).

Les simulations ont été effectuées avec la DFT standard et polarisé en spin avec la fonctionnelle d'échange-corrélation GGA-PBE, et, quand nécessaire, avec une correction d'Hubbard dans l'approche GGA+U, pour prendre en considération la corrélation électronique forte dans les manganites. Tous les calculs ont été menés avec le programme VASP [75], à partir de pseudopotentiels PAW [76].

Nous avons choisi comme système deux manganites purs: CaMnO_3 et NdMnO_3 , ayant déjà fait l'objet d'études précédentes [13, 11], afin de valider notre protocole de simulation. Deux systèmes semi-dopés – $\text{Nd}_{0.5}\text{Ca}_{0.5}\text{MnO}_3$ et $\text{Lu}_{0.5}\text{Ca}_{0.5}\text{MnO}_3$ – ont alors été considérés par la suite. Nous avons choisi ces systèmes pour deux raisons: (i) les composés semi-dopés contenant le La et le Pr ont déjà fait l'objet de travaux antérieurs [11, 12], et il nous a donc semblé naturel de poursuivre la série de lanthanide avec le système Nd-Ca; (ii) nous avons choisi les composés de LuCa parce que le Lu, à l'instar de La, est saturé au niveau de ses orbitales 4f et qu'il présente de surcroît le plus petit rayon ionique dans la série de lanthanides. Pour chaque système, une optimisation totale de la structure, à savoir des paramètres de maille et des coordonnées atomiques, a été effectuée, suivie d'une étude des propriétés électroniques et magnétiques.

Ce chapitre est organisé selon le plan suivant. Après une description générale des

calculs, les résultats structuraux seront présentés, suivis des résultats concernant les propriétés électroniques et magnétiques de ces manganites.

5

Computational results

This chapter presents the results of the ab-initio calculations on pure and half-doped manganites. These calculations have been performed to confirm (or invalidate) experimental results and, conversely, to see to what extent ab initio calculations can reproduce complex physical properties, and to gain further insight into experimental results via quantities more easily accessible in calculations (for example, the electronic density of states).

The calculations were performed with standard, spin-polarized DFT with the GGA-PBE, exchange-correlation functional, and, when needed, with a Hubbard correction in the GGA+U approach, to take into account the strong electronic correlation in manganites. All calculations were performed with the VASP code [75], with Projector Augmented Wave (PAW) pseudopotentials [76].

The calculations involved two pure manganites: CaMnO_3 and NdMnO_3 , which have been previously studied [13, 11], in order to test the computational approach. Two half-doped systems – $\text{Nd}_{0.5}\text{Ca}_{0.5}\text{MnO}_3$ and $\text{Lu}_{0.5}\text{Ca}_{0.5}\text{MnO}_3$ – were considered thereafter. We have chosen these systems for two reasons: (i) the half-doped compounds containing La and Pr already were studied [11, 12], therefore we decided to continue the lanthanide series with Nd-Ca system; (ii) we have chosen the Lu-Ca compounds because Lu has a completely full 4f shell and the smallest ionic radius in the lanthanides series, comparable to La. For each system a full structure optimization, that is of lattice parameters and atomic coordinates, was performed, followed by a study of the electronic and magnetic properties.

This chapter is organized as explained below. After a general description of the calculations, the structural results are reported, followed by results concerning the electronic and magnetic properties of these manganites.

5.1 Calculation model

The manganites studied were described in the $Pbnm$ crystal structure model, where the unit cell contains 4 LnMnO_3 units. This unit cell which is a $(\sqrt{2}, \sqrt{2}, 2)$ multiplication of the simple cubic perovskite cell and it allows the study of tilting of 4 MnO_6 octahedra. In half-doped manganites three inequivalent arrangements of Ln-site cations have been considered, they are shown below in figure 5.1.

In this work, we used the VASP code that implements density functional theory

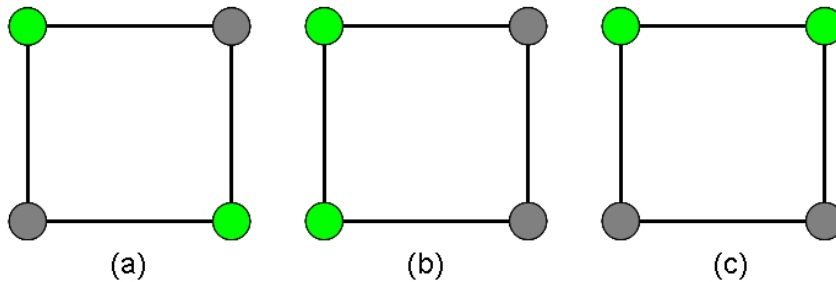


Figure 5.1: Arrangement Neodymium (gray circles)-Calcium (green circles) (Nd/Ca) in the three different cases for $\text{Nd}_{0.5}\text{Ca}_{0.5}\text{MnO}_3$ system simulated

(DFT) to determine the electronic structure of a configurations of ions. The input is an initial configuration of atoms (and their magnetic moments) in a crystallographic cell, which describes periodic boundary. The simplest output is the energy of that configuration of atoms and the forces on the atoms, which can be used to find the equilibrium structure of the crystal for which the total energy is a minimum and the residual forces are close to zero. Another form of output is the electronic structure as a real space array of electronic density and a population of electronic energy levels (bands in a solid), which can be integrated to give the electronic density of states. Calculations were all performed using PAW pseudopotentials and the GGA-PBE functional to describe electronic exchange and correlation effects.

The PAW pseudopotentials were taken from the database provided in the VASP package. The valence configuration reported in table 5.1: the electronic configuration of Nd in the is case (11 electrons, Nd_3 POTCAR file) actually mimics that of La, leaving the $4f$ electrons frozen in the core, when the Nd is in a $3+$ oxidation state. We also performed calculations including all $4f$ electrons (14 valence electrons in all, Nd POTCAR file), but this pseudopotential resulted in difficulties in electronic convergence. This is due to the fact that the GGA functional is not able to reproduce the localized character of the f electrons of

lanthanides [98].

A similar problem arises for the localized electronic density of the Mn d-orbitals.

O	$2s^2 2p^4$
Mn	$3p^6 4s^2 3d^5$
Ca	$3s^2 3p^6 4s^2$
Nd	$5s^2 5p^6 4f^1 6s^2$

Table 5.1: External electronic configuration considered in PAW data sets

In this case, the Hubbard correction, GGA+U, was used to account for the effect of electron correlation, which enhances electronic localisation. The onsite interaction for the Mn d-orbitals was modelled using Dudarev's spherical approach [99], the $|U - J|$ parameter, significant for this model, was chosen according to literature [12] that indicates the values 7.9 eV and 0.9 eV for U and J respectively.

All calculations were performed using a plane wave basis set with an energy cut-off of 400 eV [83]. For Brillouin-Zone integrations, sums over Monkhorst-Pack grids [100] were used. For structural relaxation we used a 2x2x2 k-point mesh, while magnetic properties were calculated using a 6x6x6 k-point grid, in order to have a greater accuracy in the electronic calculations. In all calculations, the electronic self-consistent cycles were made to converge until the variation of the total energy was less than 10^{-6} eV. All structural relaxations were run until forces on ions were lower than 10^{-2} eV/Å.

5.2 Structure geometry optimization

In order to test the DFT-based approach for modeling manganites, we started by simulating the structural and magnetic properties of CaMnO_3 and the NdMnO_3 , that have already been studied by Filippetti et al. and Dabrowsky et al. [13, 101]. These two systems present a perovskite, cubic structure with six oxygen atoms and one manganese atom in the orthorhombic structure, shown in figure 5.2. The magnetic structure of CaMnO_3 is known to be G-type and NdMnO_3 is A-type [102]. These calculations were then extended to half-doped, Nd-Ca, represented in a $(\sqrt{2}, \sqrt{2}, 2)$ cell, for which the most appropriate magnetic structure is C-type. The known magnetic structure is CE-type which requires a supercell to be studied

and this model will be presented at the end of this chapter.

The calculations were performed in two steps. First of all, we performed geometry

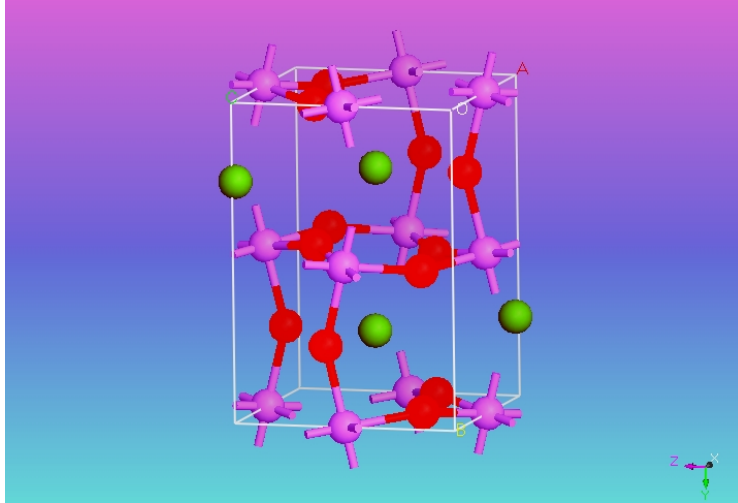


Figure 5.2: CaMnO_3 structure obtained from geometry relaxation simulation with the Hubbard correction.

optimisation, including lattice parameters and atomic coordinates, using the most appropriate magnetic structures. These results are described below and compared with experimental structures in the next section. Thereafter, these nuclear structures were used as the starting point for a more detailed study of the relative stability of different magnetic structures and the electronic density of states.

In order to verify the convergence of the calculations we checked the trend and final value of the biggest and average forces. Figure 5.3 shows the typical convergence of forces in a VASP geometry optimisation. Tests were performed, including a much larger number of ionic shifts. Beyond 30 ionic displacements, there was no significant improvement in the residual forces.

The calculation of the ground state total energy of a system supplies a criterion

Parameters	GGA_AFM	GGA_FM	GGA+U_AFM	GGA+U_FM
F_{max} [$\text{eV}\text{\AA}^{-1}$]	0.002992	0.003700	0.001508	0.002320
\bar{F} [$\text{eV}\text{\AA}^{-1}$]	0.001112	0.001179	0.0005391	0.0006144
Energy tot [eV]	-150.0800	-149.8720	-131.5328	-131.6995

Table 5.2: Convergence parameters and final energy of relaxation of CaMnO_3 with and without Hubbard correction, in FM and AFM (G-type) spin configurations.

for choosing the atomic arrangement that a system is most likely to adopt. In table

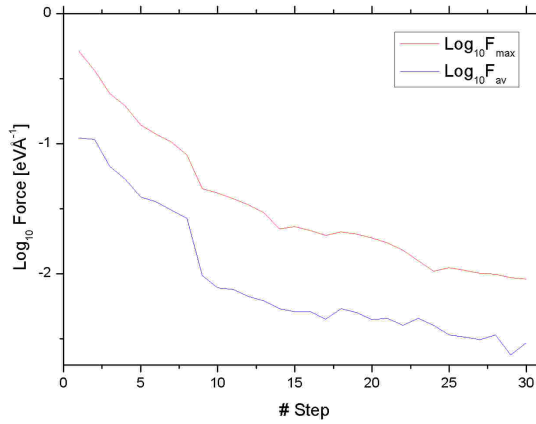


Figure 5.3: The trend of forces acting on atoms (max and average) during geometry optimisation. This example relates to the Nd-Ca half-doped system in the antiferromagnetic, C-type spin configuration, without Hubbard correction.

5.2, we report the converged forces (maximum and average) forces and final, total energy of structural relaxations for CaMnO_3 . Without the Hubbard approximation, the most stable configuration (lowest total energy) is obtained for the known G-type AFM configuration, the energy difference with respect to the FM structure being 0.21 eV. Including the Hubbard correction, this order is inverted with the FM structure being 0.16 eV more stable than the AFM structure. We emphasise here the point that the Hubbard correction for the Mn d-orbital increases the total energy by approximately 20 eV. Energies from calculations performed with and without the Hubbard correction cannot therefore be compared.

In the case of NdMnO_3 the FM structure is more stable than the AFM structure both with and without the Hubbard correction, see table 5.3. Without the Hubbard correction the FMM state is more stable by 0.43 eV, whereas this value is much smaller, 0.05 eV, with the Hubbard correction.

With the same procedure we optimised the structure of half-doped $\text{Nd}_{0.5}\text{Ca}_{0.5}\text{MnO}_3$ in the single crystallographic cell. The starting structure (lattice parameters and atomic coordinates) was taken from the work of Blasco et al. [102] since we have not repeated the diffraction study on this system. The results for the most symmetric configuration of the Nd and Ca (see Figure 5.1(a)) are reported in table 5.4. For the half-doped compound, the results follow the trend observed for the Ca manganite. Without the Hubbard correction, the AFM structure is more stable than

Parameters	GGA_AFM	GGA_FM	GGA+U_AFM	GGA+U_FM
F_{max} [eVÅ ⁻¹]	0.000917	0.005449	0.000570	0.004872
\bar{F} [eVÅ ⁻¹]	0.0002944	0.001804	0.0002185	0.002063
Energy tot [eV]	-166.6893	-167.1262	-153.9829	-154.0358

Table 5.3: Convergence parameters and final energy of relaxation of NdMnO₃ with and without Hubbard approximation, in FM and AFM (A-type) spin configurations.

the FM structure by 0.12 eV. This order is inverted when the Hubbard correction is applied, the FM structure being 0.09 eV more stable.

At this point, we tentatively conclude that DFT calculations cannot be used to

Parameters	GGA_AFM	GGA_FM	GGA+U_AFM	GGA+U_FM
F_{max} [eVÅ ⁻¹]	0.016001	0.009301	0.002533	0.002430
\bar{F} [eVÅ ⁻¹]	0.0060604	0.003395	0.000599	0.001046
Energy tot [eV]	-159.2785	-159.1517	-143.3151	-143.4075

Table 5.4: Convergence parameters and final energy of relaxation of Nd_{0.5}Ca_{0.5}MnO₃ calculated with and without Hubbard correction, in FM and AFM (C-type) spin configurations.

predict the correct magnetic order. Indeed the calculations performed with the Hubbard correction, which is the most appropriate for the manganites, systematically predict that the FM structure is more stable than the AFM structure, although the energy difference with respect to the AFM structure is small; 0.05 eV, 0.09 eV and 0.16 eV in the three cases studied here. These initial calculations are the basis for higher precision studies of the magnetic order and electronic structure that are presented later in this chapter. In the context of this thesis and the experimental structure determination of half-doped manganites, it is essential to compare the structures resulting from this set of geometry optimisations with experimental data, which follows below.

5.3 Comparison between experimental and computational structural data

Experimentally, CaMnO₃ and NdMnO₃ have an orthorhombic perovskite structure (in the *Pbnm* symmetry group) of GdFeO₃-type at room temperature [103]. A

common characteristic of this structure is the oxygen octahedra and the fact that the octahedra are distorted and tilted. This is indeed typical of rare earth manganites because of the Jahn-Teller effect on the d-electronic shell of manganese ions in a cubic environment.

CaMnO_3 and NdMnO_3 are experimentally found to be antiferromagnetic systems

Parameters	GGA_AFM	GGA_FM	GGA+U_AFM	GGA+U_FM	Exp
a [\AA]	5.2477	5.2479	5.3055	5.3143	5.2687(1)
b [\AA]	5.3119	5.3065	5.3995	5.4080	5.2813(1)
c [\AA]	7.3987	7.4303	7.4902	7.5108	7.4582(1)
Vol [\AA^3]	206.24	206.92	214.57	215.86	$\sim 207.5(1)$
Mn-O _z [\AA]	1.887	1.901	1.925	1.936	1.895(1)
Mn-O _y [\AA]	1.915	1.915	1.955	1.960	1.904(3)
Mn-O _x [\AA]	1.914	1.913	1.948	1.950	1.903(3)
Mn-O _{ap} -Mn [deg]	157.2°	155.4°	153.3°	151.7°	152.1°(1)
Mn-O _{eq} -Mn [deg]	154.3°	154.2°	151.8°	151.6°	150.4°(1)

Table 5.5: Cell parameters, volume, bond lengths and angles of CaMnO_3 from DFT-VASP calculations, with and without Hubbard approximation, in FM and AFM spin configurations, compared with the available experimental data [102].

at low temperature, below 123 K and 78 K respectively for these systems. Experimental lattice and structural parameters have been reported by several authors [102, 101] but full data has not been found at low temperature in the antiferromagnetic phases. The experimental data shown in the tables below are therefore room temperature data, corresponding to a paramagnetic phase, unless otherwise stated. In the following comparison, we will bear in mind the effect of thermal expansion and magneto-elastic differences between the low temperature AFM structure and the higher temperature, paramagnetic phase. According to the recent work of Chatterjii et al. [104] on NdMnO_3 , thermal expansion (from 100 K to 300 K) and magneto-elastic effects both equate to a $\sim 1\%$ change in cell volume and therefore a few 0.1% in cell parameters.

In table 5.5 we compare the computational results with the experimental ones for CaMnO_3 . Note that the calculations correspond to a temperature of 0 K. Looking at the cell volumes, it is clear that the calculations without Hubbard correction give optimised structures that are closest to the experimental structure. The difference of any structural parameter between experimental and calculated values is less than 1%. The difference between AFM and FM structures is similarly small, indicating a small magneto-elastic effect. The bond angle Mn-O-Mn in the xy-plane is

smaller than the corresponding angle along the z-direction, which is characteristic of the tilt of the Mn-O₆ octahedra and in good agreement with experiment. The effect of the Hubbard correction is a significant elongation (by ~ 0.05 Å) of the Mn-O bond length, which results in an expansion of the cell parameters, hence the overestimate of the cell volume by about 10 Å³. For the NdMnO₃ we report

Parameters	GGA_AFM	GGA_FM	GGA+U_AFM	GGA+U_FM	Exp
a [Å]	5.4162	5.4105	5.4440	5.4503	5.41678(51)
b [Å]	5.6501	5.5355	5.7167	5.6037	5.85182(54)
c [Å]	7.6426	7.7734	7.7034	7.8291	7.54791(72)
Vol [Å ³]	233.88	232.82	239.74	239.12	239.25(4)
Mn-O _z [Å]	1.970	1.994	1.997	2.021	1.9520(5)
Mn-O _y [Å]	1.929	1.984	1.940	2.012	2.2234(15)
Mn-O _x [Å]	2.108	1.997	2.151	2.028	1.9109(15)
Mn-O _{ap} -Mn [deg]	151.9°	154.0°	149.4°	151.2°	150.38°
Mn-O _{eq} -Mn [deg]	151.6°	152.9°	149.2°	150.7°	149.27°

Table 5.6: Structural parameters of NdMnO₃ single cell with and without Hubbard approximation, in FM and AFM configuration, compared with the experimental results [101].

our computational results ($T = 0$ K) and the corresponding experimental results [101] (at room temperature) in table 5.6. In this case the structures obtained with and without Hubbard approximation are less different than in the Ca case. At first sight, the calculations with Hubbard correction give a cell volume in almost perfect agreement with the experimental value, in contrast to the result obtained for the Ca system. However, allowing for a typical expansion of a few Å³ upto room temperature, the calculations with Hubbard correction will slightly overestimate the cell volume, while the calculations without Hubbard correction will underestimate the cell volume by a similar amount. But for both AFM calculations, with and without Hubbard correction, the optimised structures are clearly in better agreement with the experimental data than the FM structures. In the case of NdMnO₃ and in contrast to CaMnO₃, there is no inverse Jahn-Teller effect so the Mn-O bond in the z-direction is not the smallest. This effect is reproduced by all calculations but the difference between bond lengths in the z-direction and in the xy-plane is bigger in the AFM structures and compares better with the experimentally observed difference. Finally the Mn-O-Mn bond angles which relate to the tilting of the octahedra are better reproduced by the AFM calculations in terms of the absolute values but the differences in bond angles between the

z-direction and the xy-plane is better with the FM structures.

We calculated the nuclear structure for three different arrangements of

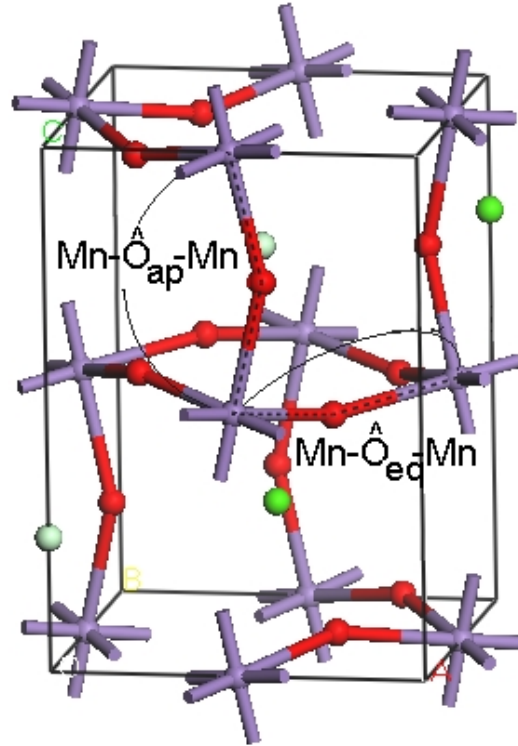


Figure 5.4: $\text{Nd}_{0.5}\text{Ca}_{0.5}\text{MnO}_3$ system obtained from geometry relaxation simulation in GGA+U approach. In red circles: O; in magenta circles: Mn; in gray circles: Nd; in green circles: Ca.

$\text{Nd}_{0.5}\text{Ca}_{0.5}\text{MnO}_3$. We report in table 5.7 only the results for the structure (a) of figure 5.1 because this structure is closest to our experimental results obtained by neutron powder diffraction on D20 at the ILL (see chapter 5).

As for CaMnO_3 , the best agreement is obtained between experimental structures and those computed without the Hubbard correction. Adding the Hubbard correction again leads to longer Mn-O bonds and a significantly increased cell volume. The difference between the AFM and FM calculations is almost negligibly small, for both kinds of calculation. We can observe an inverse Jahn-Teller effect, evidenced by the Mn-O_x and Mn-O_y distances being longer than Mn-O_z bond lengths, from all our calculations and this is in good agreement with the experimental measurements. In terms of the Mn-O-Mn angles, all calculations report a bigger angle in the xy-plane compared to along the z-axis, as observed experimentally. However the absolute values obtained from the calculations

Parameters	GGA_AFM	GGA_FM	GGA+U_AFM	GGA+U_FM	Exp
a [Å]	5.3874	5.3841	5.4371	5.4373	5.4132(3)
b [Å]	5.4439	5.4337	5.5176	5.5198	5.4336(3)
c [Å]	7.4515	7.4934	7.5167	7.5387	7.4858(3)
Vol [Å ³]	218.54	219.22	225.49	226.26	220.18(3)
Mn-O _z [Å]	1.905	1.920	1.936	1.946	1.917(1)
Mn-O _y [Å]	1.955	1.954	1.989	1.990	1.944(6)
Mn-O _x [Å]	1.965	1.963	1.997	1.999	1.963(6)
Mn-O _{ap} -Mn [deg]	155.1°	155.1°	151.4°	150.3°	154.9°(1)
Mn-O _{eq} -Mn [deg]	156.9°	156.9°	154.3°	154.0°	158.1°(2)

Table 5.7: Cell parameters, volume, bond lengths and angles of Nd_{0.5}Ca_{0.5}MnO₃, NdCa_a (see figure 5.1(a)) compared with our experimental results (obtained on D20 instrument at ILL).

without Hubbard correction are most accurate.

At this point, we can conclude that DFT, with or without a Hubbard correction, accurately reproduces the trends in structural features of the pure and half-doped manganites, for example, the tilting of octahedra and the (inverse) Jahn-Teller effect. For the pure Ca system and the half-doped system, the calculations without Hubbard correction are quantitatively more accurate. In the systems studied here, the Hubbard correction systematically increases the Mn-O distances and therefore the cell parameters. This is consistent with the result from the previous section that the Hubbard correction favours the FM structure, that is FM is favoured when the magnetic centres are further apart.

5.4 Magnetic properties

The main goal of these calculations was the study of the magnetic properties of the half-doped Nd_{0.5}Ca_{0.5}MnO₃, starting from the two (extremal), pure manganites, CaMnO₃ and NdMnO₃. For the two pure systems, the single cell is enough to reproduce the experimentally observed magnetic configuration (AFM). However, to study Nd_{0.5}Ca_{0.5}MnO₃ system, we should adopt a larger super-cell and this will be described in a later section. In the single cell calculations presented here, the most relevant magnetic structure is C-type.

The systems under investigation exhibit G (Ca), C (Nd-Ca) and A (Nd)-type magnetic orders, see figure 5.5. In the following calculations, the structures from the previous sections have been used in a series of higher precision (6x6x6 k-point

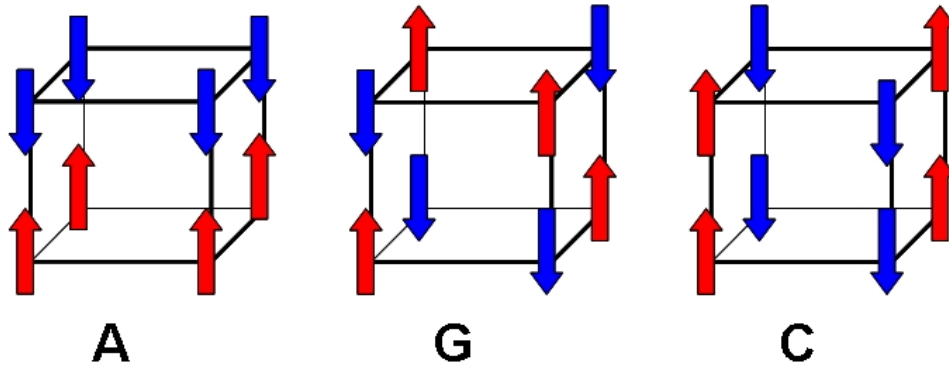


Figure 5.5: Layout of AFM structure of simulated systems: A-type for the NdMnO_3 (FM in the plane and AFM between the planes), G-type for the CaMnO_3 (completely AFM) and C-type for the $\text{Nd}_{0.5}\text{Ca}_{0.5}\text{MnO}_3$ (AFM in the plane and FM between the planes.) Note that in a single cell only Mn are present and we cannot describe the whole spin configuration in all cases.

mesh), geometry optimisation calculations to investigate the relative stability of different AFM structures. In addition, we have also optimised the FM, B-type structure for comparison, since this has tended to be favoured energetically in calculations presented so far. We specified the initial magnetic moments for each Mn ion in the structure according to the magnetic order structure type, starting from magnetic moments of $5 \mu_B$, corresponding to $1.2 \times \mu_{\text{theoretical}}$ as suggested in the VASP manual [75]. Geometry optimisation does not allow the magnetic structure to change from one type to another.

For all magnetic configurations, we have performed calculations in the GGA and GGA+U approximations. In the following tables the column headings indicate the origin of the starting structure, for example, GGA+U_FM indicates that the starting structure was the result of the geometry optimisation performed with the Hubbard correction and a FM magnetic order. The purpose of using slightly different starting structures was to better explore the potential energy landscape since geometry optimisation only gives access to a local minimum close to the starting point.

CaMnO₃ Neutron powder diffraction measurements [102] indicate that the most stable magnetic configuration for CaMnO_3 is G-type (see figure 5.5). Our results from calculations are reported in table 5.8. In contrast with the experimental results, we find that, without the Hubbard correction, the most stable configuration

Type	GGA_AFM	ΔE	GGA_FM	ΔE	GGA+U_AFM	ΔE	GGA+U_FM	ΔE
A	-150.0095		-150.0192	-	-131.7906	0.1535	-131.8169	0.1789
G	-149.9472	0.0623	-149.9659	0.0533	-131.5130	0.4311	-131.5281	0.4677
C	-149.8439	0.1655	-149.8958	0.1234	-131.5731	0.3710	-131.6013	0.3945
B	-149.7797	0.2298	-149.3129	0.7063	-131.9441	-	-131.9958	-

Table 5.8: Values of total energy in eV for CaMnO_3 . The details of calculations are specified in the text. ΔE corresponds to the variation of the energy with respect to the appropriate minimum values.

is AFM-A. The AFM-G state is slightly higher in energy, ~ 0.05 eV. This disagreement with the experiment may come from neglecting many-body effects within the GGA approximation [105].

The calculations performed with the Hubbard correction, which results in more extended structures (see above), continue to favour the FM, B-type structure. In order to see if the value of the effective correlation potential (U-J) on the Mn-d electrons influences this result, we have performed a set of calculations for different values of U compared to the values used so far: $U = 7.9$ eV and $J = 0.9$ eV (as in Ref. [12]). Selected results are reported in table 5.9. The value of U does not change the relative stability of the magnetic structures, be it FM with respect to AFM, or between the different AFM structures. Increasing U increases the energy differences between the different structures. Extrapolating to very small values of U would allow the relative stability of structures to change since the A-type AFM structure is most stable without the Hubbard correction. However, other considerations, like the band gap in the electronic density of states (see below), and values found in literature, make us believe that the value of $|U-J| = 7$ eV is most reasonable and we retain this value in all future calculations.

In the figure 5.6, we report the calculated electronic densities of states for Mn-d

Type	U=6.9 [eV]				U=7.9 [eV]				U=8.9 [eV]			
	AFM	ΔE	FM	ΔE	AFM	ΔE	FM	ΔE	AFM	ΔE	FM	ΔE
A	-133.9067	0.0843	-133.9528	0.1028	-131.7906	0.1535	-131.8169	0.1789	-129.8558	0.2259	-129.9162	0.2640
G	-133.7200	0.2710	-133.7574	0.2982	-131.5130	0.4311	-131.5281	0.4677	-129.4541	0.6276	-129.5032	0.6770
C	-133.7425	0.2485	-133.7902	0.2654	-131.5731	0.3710	-131.6013	0.3945	-129.5633	0.5184	-129.6293	0.5509
B	-133.9910	-	-134.0556	-	-131.9441	-	-131.9958	-	-130.0817	-	-130.1802	-

Table 5.9: Values of total energy in eV for CaMnO_3 calculated for three different values of Coulomb interaction, $U = 6.9$ eV - 7.9 eV - 8.9 eV, in the GGA+U approach.

orbitals decomposed into $d_{x^2-y^2}$ and d_{z^2} for e_g , and d_{xy} , d_{xz} and d_{yz} for t_{2g} , in

FM (B-type) and AFM G-type states. The calculations were performed with the Hubbard approximation. In the G-type magnetic configuration, there is an energy gap in the Mn-d orbital of about 1 eV. Filippetti et al. obtained about 0.4 eV using *ab-initio* simulations [13]. This energy gap is obtained only for the AFM structure and using the Hubbard correction. In figure 5.6, on the right side of the Fermi level ($E > 0$), we find the empty e_g levels and on the left side of the Fermi level ($E < 0$), we observe the populated, majority spin channel, t_{2g} states, corresponding to the Mn^{4+} ions having only the t_{2g} states half-filled with three spin-up electrons, as expected for this compound. The magnetic moment of Mn ions, calculated with the Hubbard correction and visualised from the difference of spin-up and spin-down channels in figure 5.6, is $\sim 3.4 \mu_B$, as found in literature [13]. This value of the Mn magnetic moment is consistent, although slightly larger than expected for a $S = 3/2$ spin configuration.

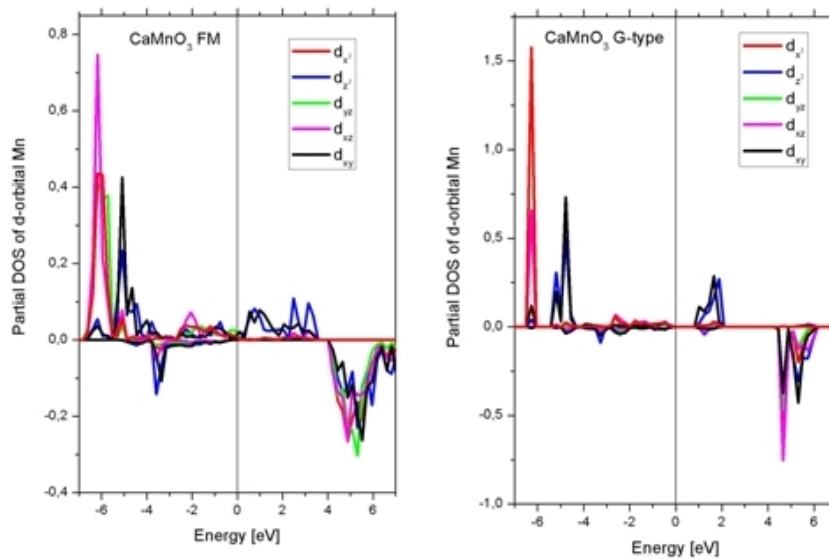


Figure 5.6: CaMnO_3 : the orbital-decomposed partial electronic density of state of Mn 3d components, in CaMnO_3 : $d_{x^2-y^2}$ and d_{z^2} for e_g , and d_{xy} , d_{xz} and d_{yz} for t_{2g} .

NdMnO₃ Experimentally, this system is an antiferromagnetic insulator with AFM-A magnetic spin configuration [101, 106]. In table 5.10, we show the results from a range of calculations.

In all GGA and GGA+U calculations, the FM B-type configuration is energetically

Type	GGA_AFM	ΔE	GGA_FM	ΔE	GGA+U_AFM	ΔE	GGA+U_FM	ΔE
A	-166.8585	0.0970	-166.6333	0.6197	-154.4445	0.0856	-153.8823	0.5458
G	-166.4371	0.5184	-166.2779	0.9751	-154.1096	0.4206	-153.2399	1.1882
C	-166.6428	0.3125	-166.6370	0.6160	-154.1532	0.3352	-153.4124	1.0157
B	-166.9555	-	-167.2530	-	-154.5301	-	-154.4281	-

Table 5.10: Values of total energy in eV for NdMnO_3 . The details of calculations are specified in the text. ΔE corresponds to the variation of the energy with respect to the appropriate minimum values.

most stable. Interestingly the next most stable structure in all cases is the observed, AFM A-type structure. This energy difference with respect to the FM structure can be as small as 0.08 eV while the next most stable AFM structure (C-type) is ~ 0.3 eV higher.

The electronic density of states of the NdMnO_3 system for the Mn-d orbitals are shown in figure 5.7, for the FM and AFM A-type structure. These calculations were performed with the Hubbard correction. The energy gap for the AFM structure is about 1 eV, consistent with results from Yamauchi et al., who obtained a value of 0.5 eV. On the left side of the Fermi level ($E < 0$) we observe the populated, majority spin channel, t_{2g} states and, just below the Fermi level, the single occupied e_g state, corresponding to Mn^{3+} . The unoccupied e_g level in the spin-up channel is about 1 eV above the Fermi level so that these two e_g levels define the band gap.

The magnetic moment calculated without the Hubbard correction for the AFM-A configuration gives a value of $\sim 3.6 \mu_B$, which is in reasonable agreement with the experimental magnetic moment of $3.22(9) \mu_B$ found by Munoz et al. [106]. Using the Hubbard correction, we found a bigger value of about $4.1 \mu_B$, compared to the theoretical value of $4 \mu_B$ for this system.

$\text{Nd}_{0.5}\text{Ca}_{0.5}\text{MnO}_3$ We have attempted the same approach for the $\text{Nd}_{0.5}\text{Ca}_{0.5}\text{MnO}_3$ system, within the approximation that single cell calculations under consideration here cannot represent the true CE-type AFM structure. In this case, the most appropriate magnetic structure is C-type.

In the table 5.11 we report the total energies of FM and AFM geometry optimised configurations. The GGA+U calculations (AFM) shows that the FM B-type magnetic energy is still most stable, whereas the calculations without Hubbard correction favour the A-type AFM structure. In fact a significant energy difference

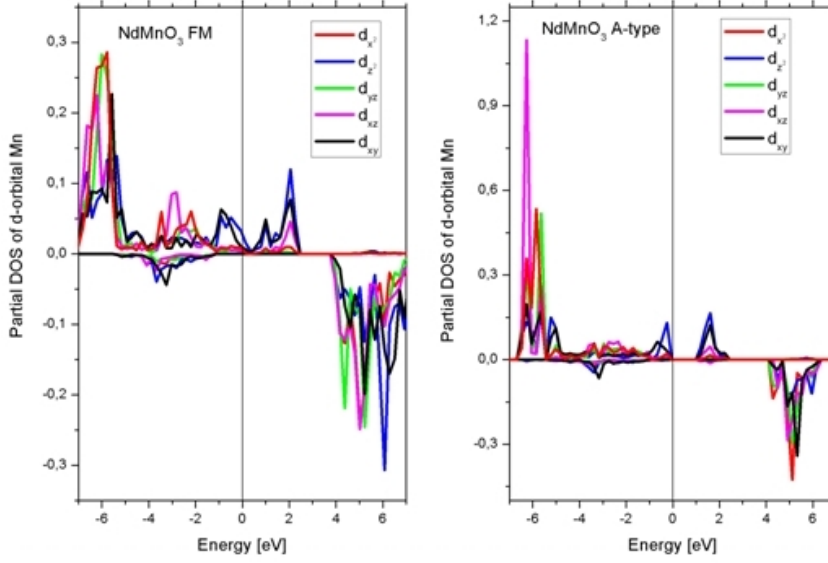


Figure 5.7: NdMnO_3 : the orbital-decomposed partial electronic density of state of Mn 3d components: $d_{x^2-y^2}$ and d_{z^2} for e_g , and d_{xy} , d_{xz} and d_{yz} for t_{2g} , in the NdMnO_3 system.

Type	GGA_AFM	ΔE	GGA_FM	ΔE	GGA+U_AFM	ΔE	GGA+U_FM	ΔE
A	-159.3112	-	-159.3262	-	-143.6602	0.0854	-143.6796	0.0997
G	-158.6774	0.6338	-158.7352	0.5910	-142.0768	1.6688	-142.1129	1.6664
C	-158.5987	0.7125	-158.6943	0.6319	-142.6400	1.1056	-142.7081	1.0712
B	-159.1659	0.1453	-159.2138	0.1124	-143.7456	-	-143.7793	-

Table 5.11: Values of total energy in eV for the half-doped Nd-Ca system. The details of calculations are specified in the text. ΔE corresponds to the variation of the energy with respect to the appropriate minimum values.

of ~ 1.1 eV is found between the FM B-type and AFM C-type configurations for calculations performed with the Hubbard correction and, without the Hubbard correction, the C-type structure is still the most energetic.

In the case where we used the Hubbard approximation the A-type magnetic structure results as energetically more stable, with an energy difference of about 0.7 eV between the A-type and C-type magnetic states.

For this half-doped system, for the Mn^{3+} and Mn^{4+} magnetic moments we found values of $2.90 \mu_B$ and $2.89 \mu_B$ in the AFM C-type magnetic structure, without the Hubbard correction. We found $3.81 \mu_B$ for Mn^{3+} and $3.80 \mu_B$ for Mn^{4+} , in GGA+U method. The theoretical values for the magnetic moments are $4 \mu_B$ and $3 \mu_B$ for Mn^{3+} and Mn^{4+} , respectively, while the experimental values are $2.25 \mu_B$

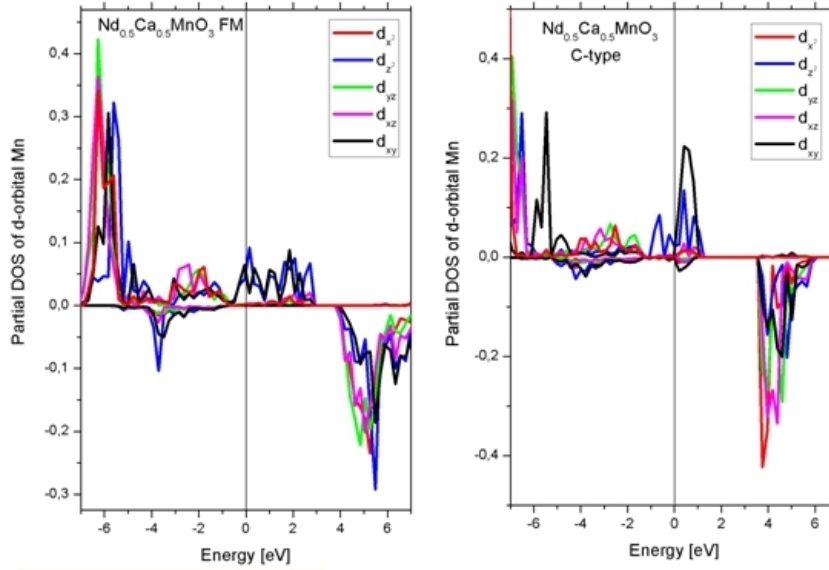


Figure 5.8: $\text{Nd}_{0.5}\text{Ca}_{0.5}\text{MnO}_3$: the orbital-decomposed partial electronic density of state of Mn 3d components: $d_{x^2-y^2}$ and d_{z^2} for e_g , and d_{xy} , d_{xz} and d_{yz} for t_{2g} , calculated for $\text{Nd}_{0.5}\text{Ca}_{0.5}\text{MnO}_3$.

and $2.45 \mu_B$ for Mn^{3+} and Mn^{4+} , respectively). The similarity between the two calculated magnetic moments, which is also reported by Anisimov, may reflect the fact that the Nd and Ca ions are in similar (even identical) chemical environments and that the C-type magnetic order does not a significant electronic ordering to be established.

In the figure 5.8 the electronic density of states of Mn-d levels for the $\text{Nd}_{0.5}\text{Ca}_{0.5}\text{MnO}_3$ in FM and in AFM C-type configurations, calculated with the GGA+U method, are reported. In contrast to the results on pure manganites, we did not find the energy gap in Mn-d level in AFM C-type magnetic structure.

At this point, we conclude that more precise magnetic calculations, including geometry optimisations starting from different initial structures do not change the relative stability of FM and AFM structures. For Ca-manganite, the correct G-type structure is the second most stable AFM structure, without the Hubbard correction, while it is the least stable structure with the Hubbard correction. For Nd-manganite, the situation is different and the sought-after A-type structure is the most stable AFM structure in all calculations, although the FM structure is most stable overall. In terms of magnetic moments, the electronic localisation caused by the Hubbard correction gives bigger moments that are in better agreement with theoretical values, but significantly overestimated compared to experimental values. The

Hubbard correction is however indispensable in terms of producing a band gap consistent with the insulating properties of these manganites. For the half-doped manganite, the results are poor in that the most reasonable magnetic structure is the most energetic and the Hubbard correction in this case does not open-up a band gap in the electronic density of states. In order to investigate the effect of the limited structural model, we have also performed calculations on a supercell which allows the CE-type magnetic order to be modelled, see below.

5.5 $Nd_{0.5}Ca_{0.5}MnO_3$ and $Lu_{0.5}Ca_{0.5}MnO_3$ super-cell structures

In this section we present the results of calculation on Nd-Ca and Lu-Ca supercells systems. The $2 \times 2 \times 1$ supercells, with 16 Mn atoms, are needed to reproduce two sublattices, associated with Mn^{3+} and Mn^{4+} ions, in CE-type magnetic configuration. La-Ca and Pr-Ca half-doped compounds have already been studied [11, 12] so we decided to continue the Ln series with Nd-Ca system. We have also included the Lu-Ca compound since Lu has the smallest ionic radius in the lanthanides series, relating to the 4f shell being completely full; Lu is therefore comparable in many respects to La. For these two systems we have considered three Ln/Ca arrangements in the supercell, labeled $LnCa_a$, $LnCa_b$ and $LnCa_c$, which replicate the structure considered in the single cell (see figure 5.1).

We investigated structural and magnetic properties: cell parameters, volume,

Parameters	$NdCa_a$	$NdCa_b$	$NdCa_c$	Nd/Ca Exp	$LuCa_a$	$LuCa_c$	Lu/Ca Exp
a[Å]	5.3961	5.3839	5.3951	5.4132(3)	5.2504	5.2509	5.3143(1)
b[Å]	5.4206	5.4155	5.3977	5.4336(3)	5.4270	5.4313	5.4667(1)
c[Å]	7.5953	7.5907	7.6055	7.4858(3)	7.4713	7.4643	7.4026(1)
$V[\text{Å}^3]$	222.16	221.32	221.48	220.1801(3)	212.89	212.88	215.0576(1)
Mn- O_z	1.942	1.944	1.938(1)	1.917(1)	1.919	1.951	1.912(1)
Mn- O_y	1.959	1.960	1.968(1)	1.963(6)	1.940	1.966	1.993(3)
Mn- O_x	1.952	1.945	1.953(1)	1.944(6)	1.924	1.955	1.961(3)
Mn- O_{ap} -Mn	154.372°	155.931°	155.463°	154.9°(1)	146.1°	146.3°	149.5°(1)
Mn- O_{eq} -Mn	155.463°	154.432°	155.463°	158.1°(2)	147.9°	150.5°	148.9°(1)

Table 5.12: $Nd_{0.5}Ca_{0.5}MnO_3$ and $Lu_{0.5}Ca_{0.5}MnO_3$ structural features: cell parameters, bond distances Mn-O and bond angles Mn-O-Mn, without Hubbard correction.

bond lengths and angles, Jahn-Teller distortion, tilting effect and the magnetic

structure for the $\text{Nd}_{0.5}\text{Ca}_{0.5}\text{MnO}_3$ and $\text{Lu}_{0.5}\text{Ca}_{0.5}\text{MnO}_3$ super-cells. Following a procedure similar to that used for the single-cell, we started with the optimization of the super-cell structure in the AFM CE-type, spin polarised configuration. This calculation was performed without the Hubbard correction, since better structural results were obtained this way for the single cell calculation. The optimised structural parameters are given in table 5.12 and compared with the nuclear structure from our experimental results. We observe a reasonably good agreement between computational and experimental results. The difference in Mn-O-Mn bond angles between the z-direction and the xy-plane is close to zero for the Nd system, while a difference of 3 degrees is reported experimentally. This structural aspect was better reproduced by the single cell calculation. For the Lu compound, the calculated equatorial angle is bigger than the 'apical' angle, whereas, experimentally, this difference is inverted. On a positive note, for all proposed geometrical arrangements of Ln-Ca (Ln = Nd and Lu), we found an inverse Jahn-Teller effect, with Mn-O_z bond distances smaller than Mn-O bond lengths in the xy-plane, in agreement with the experimental structure.

5.5.1 Electronic density of states of $\text{Nd}_{0.5}\text{Ca}_{0.5}\text{MnO}_3$ and $\text{Lu}_{0.5}\text{Ca}_{0.5}\text{MnO}_3$ super-cells

We calculated the total and site-projected electronic density of states allowing us to analyse the p-orbitals of calcium and oxygen and the d-orbitals of manganese atoms and therefore the character of the valence and conduction bands of these systems. Mn d-orbitals, which determine the magnetic ordering, and the p-orbitals of oxygen, are considered as they are responsible for the super-exchange mechanism i.e. the p-shell of oxygen was analyzed in view of its strong hybridization with the the d-electrons of Mn.

The total and partial DOS for $\text{Nd}_{0.5}\text{Ca}_{0.5}\text{MnO}_3$ (structure (a)) are plotted in figure 5.9. The total DOS does not show a band gap for the FM structure. This remark is also true for the AFM CE-type structure, although the DOS does show a minimum at the Fermi level, suggesting that the structural input and computational conditions may be close to producing an appropriate electronic band structure. The d-orbitals of Mn are divided into two bands: by symmetry, as a result of the crystal field splitting, we assume they are, at lower energy, t_{2g} bands and, at higher energies, e_g bands. Because the Mn-O₆ octahedra are not be aligned with the Cartesian axes, the labeling of the atomic orbitals we used for the projections does not actually

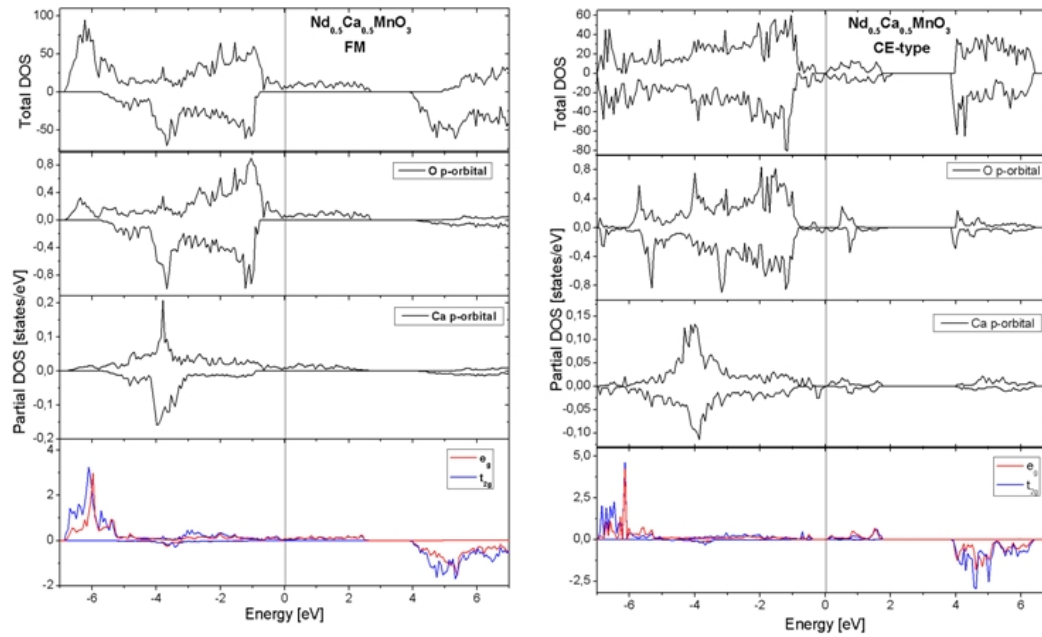


Figure 5.9: The total and partial DOS for $Nd_{0.5}Ca_{0.5}MnO_3$ in FM and AFM CE-type magnetic structure.

correspond to this assumed classification. In the region between $-6 \div 0$ eV we observe a significant overlap in energy scale between the p-orbital of O and the d-orbital of Mn, revealing a significant hybridization. This hybridization may contribute to the failure of the Hubbard approximation in opening the band gap.

The calculated magnetic moments of the manganese atoms are ~ 3.8 and $4.0 \mu_B$ for Mn^{4+} and Mn^{3+} , respectively. Our results are close to the corresponding values reported by Anisimov et al. [12]: $3.98 \mu_B$ and $3.99 \mu_B$, although we distinguish the two kinds of anions better, as indicated by the difference in magnetic moments. The difference between the Mn^{4+} and Mn^{3+} magnetic moments, $0.2 \mu_B$, is consistent with the measured one, the moments being $2.25 \mu_B$ and $2.45 \mu_B$, although experimentally the measured moments are smaller than the calculated ones. This difference indicates the presence of charge localization and charge-ordering.

The total and partial, site-projected DOS for $Lu_{0.5}Ca_{0.5}MnO_3$ are shown in figure 5.10 for a substituted structure of type (a). There is a qualitative similarity with the results presented above for the Nd-Ca system. We did not observe a band gap either for the FM or the AFM CE-type magnetic configurations. The Mn-d and O-p bands are significantly hybridized. Again, the strong hybridization of the e_g band with other orbitals may be at the origin of the failure of the Hubbard-like interaction

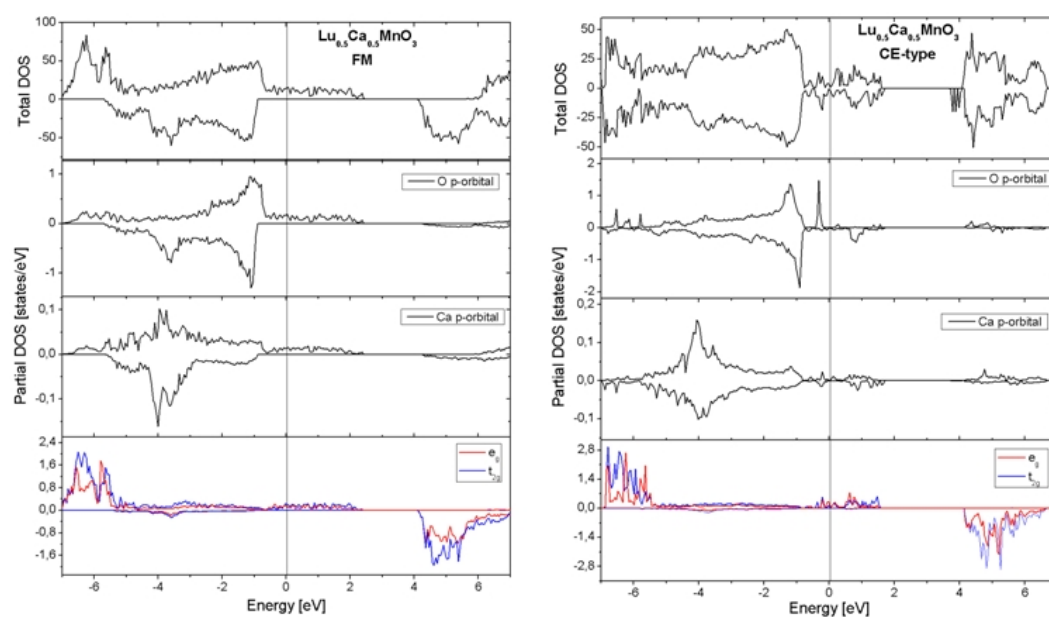


Figure 5.10: The total and partial DOS for $\text{Lu}_{0.5}\text{Ca}_{0.5}\text{MnO}_3$ in FM and AFM CE-type magnetic structure.

in opening the gap.

The calculated magnetic moments of Mn ions are 3.9 and $4.0 \mu_B$ for the Mn^{4+} and Mn^{3+} , respectively. The difference between the magnetic moments is less pronounced than in the Nd case but still reflects charge localization and ordering.

5.6 Conclusions

In this chapter, we have reported the structural and magnetic results obtained from the ab initio calculations and compared them with our experimental results and published work. Spin polarized, DFT calculations using the GGA-PBE functional, with and without a Hubbard correction, have been used to study pure (CaMnO_3 and NdMnO_3) and half-doped ($\text{Nd}_{0.5}\text{Ca}_{0.5}\text{MnO}_3$) systems described within a single unit cell. For the half-doped system, a (2,2,1) super-cell was also used in order to study the observed CE-type magnetic order and these calculations were also extended to Lu.

In the case of CaMnO_3 , we found a good agreement between calculated and measured structures, without using the Hubbard correction. The Mn-O-Mn bond angles are greater along z-direction than in the xy-plane indicating that the tilting effect is more developed along the z-axis. The experimentally observed, inverse Jahn-Teller effect is reproduced by all calculations. For the NdMnO_3 single cell, we found similarly good agreement between calculated and experimental structural parameters, although the difference between calculations with and without Hubbard corrections is less significant in this case. In terms of cell volume and parameters, the calculations with Hubbard corrections look better but this conclusion is not so clear when thermal expansion is taken into account. As for the Ca system, the Mn-O-Mn bond angles are bigger than in the z-direction than in the xy-plane and therefore the tilting effect is more pronounced along this direction. The 'normal' Jahn-Teller distortion, as observed in experimentally determined structures is found in the calculated structures.

In both of these pure systems, there is a tendency for the FM structure to be the most stable, the one exception being for the Ca system for calculations performed without a Hubbard correction, which gave an AFM structure as most stable. However, more detailed magnetic calculations showed the stable AFM structure to be A-type, with the observed G-type structure slightly more energetic (+0.06 eV). The Hubbard correction was required in both of these cases to calculate an electronic density of states with a band gap of the order of 1 eV. In addition, the observed magnetic order also had to be used to obtain this result, which is consistent with published calculations. Finally in terms of magnetic moments, the calculations with Hubbard correction gave magnetic moments of 3.4 and 3.6 μ_B for the Mn^{4+} and Mn^{3+} ions in the Ca and Nd systems, respectively.

In the context of this thesis, our primary interest concerns the half-doped manganites, in particular Nd/Ca in these computational studies. A generally good

agreement was obtained between calculated and observed structures, with the smaller unit cell obtained from calculations without the Hubbard correction being in better agreement with the experimental structure. The inverse Jahn-Teller effect, observed experimentally, was well reproduced by all calculations in the single cell model, as was the tilting of the octahedra.

The trends in the relative stability of magnetic structures mimicked those of the pure Ca system, that is FM stabilized by the calculations with the Hubbard correction, which result in bigger unit cells, and AFM stabilized by the calculations without Hubbard correction. However the C-type structure was one of the least stable magnetic structures. The density of states failed to show a band gap even using the Hubbard correction and the most appropriate, C-type magnetic order. These single cell calculations showed a small difference between the magnetic moments of different Mn ions, 3.80 and 3.81 μ_B .

In order to improve the calculations further by including the full CE-type magnetic order, a (2,2,1) supercell was considered. In this approach, the structural agreement was less good in terms of octahedral tilting and a band gap could still not be opened using the Hubbard correction and the known CE-type magnetic structure. The most significant improvement from this type of calculation concerned the magnetic moments on the Mn ions, with values close to those calculated for the pure manganites, 3.8 and 4.0 μ_B , indicating a high degree of charge ordering. Extending this type of calculation to the Lu-Ca half-doped system also failed to produce a band gap, despite the fact that calculations, giving a band gap, have been published on the La-Ca half-doped system, which is disappointing given the electronic similarity between Lu and La.

Thus we conclude that the level of DFT calculations used here reproduce well the structural aspects of pure and half-doped manganites. While all magnetic structures can be stabilized and, thereafter, investigated in more detail, the calculations cannot correctly predict the most stable magnetic structure. For all systems, the electronic band structure and DOS appears reasonable, revealing the occupation of the Mn-d orbitals and the overlap and hybridization with O-p orbitals, but the required band gap of these insulators could only be calculated for the pure systems. The supercell calculations were able to show a high degree of charge ordering through the magnetic moments on the Mn ions.

Finally, we conclude that electronic and magnetic structures are very sensitive to structural details. We have systematically optimized all structural parameters and feel, in retrospect, that it would be useful to perform calculations directly on

experimentally determined structures.

Conclusions

Dans ce chapitre, nous avons présenté les résultats des structures nucléaires et magnétiques pour les systèmes étudiés obtenus à partir des calculs ab-initio et comparé ceux-ci à nos résultats expérimentaux ou à résultats publiés antérieurement. Les calculs de DFT en spin polarisée, utilisant la fonctionnelle GGA-PBE, avec et sans la correction de Hubbard, ont été utilisés pour étudier les systèmes purs (CaMnO_3 et NdMnO_3) et le système semi-dopé ($\text{Nd}_{0.5}\text{Ca}_{0.5}\text{MnO}_3$) décrits dans une maille simple. Pour le système semi-dopé, la super-maille $a(2,2,1)$ a également été utilisée lors de l'étude de l'ordre magnétique de type CE et ces calculs ont alors été prolongés au système Lu.

Dans le cas de CaMnO_3 , nous avons trouvé un bon accord entre les structures calculées et mesurées, sans utiliser la correction de Hubbard. Les angles Mn-O-Mn sont plus grands le long de la direction z que dans le plan xy indiquant que l'effet de tilting est développé selon l'axe z . L'effet Jahn-Teller inverse, expérimentalement observé, est reproduit par tous les calculs. Pour la maille de NdMnO_3 , nous avons également trouvé un bon accord entre les paramètres structuraux calculés et expérimentaux, bien que la différence entre les calculs avec et sans la correction de Hubbard soit moins significative dans ce cas. En terme de volume et de paramètres de maille, les calculs avec la correction de Hubbard sont meilleurs mais à considérer toutefois avec précaution du fait de l'introduction d'une dilatation thermique dans le système. Comme pour le système Ca, les angles Mn-O-Mn sont plus grands selon l'axe z que dans le plan xy indiquant donc un effet de tilting plus prononcé le long de cette direction. Enfin, l'effet Jahn-Teller normal est présent dans les structures calculées, à l'instar des structures expérimentales.

Dans les deux systèmes purs, il y a une tendance indiquant une meilleure stabilité de la structure FM, à la seule exception du système Ca pour laquelle les calculs sans correction de Hubbard ont donné une structure AFM plus stable. Cependant, des calculs magnétiques plus détaillés ont montré que la structure AFM la plus stable était de type A, tandis que la structure expérimentale de type G a été trouvée comme légèrement moins stable (+0.06 eV). La correction de Hubbard a été nécessaire dans les deux cas afin de calculer une densité électronique d'états avec un gap d'énergie de l'ordre de 1 eV. En outre, l'ordre magnétique observé a dû également être utilisé pour obtenir ce résultat, qui est compatible avec les simulations effectuées. Enfin, en terme de moments magnétiques, les calculs avec la correction de Hubbard ont donné des moments magnétiques de 3.4 et 3.6 μ_B

pour les ions Mn^{4+} et Mn^{3+} respectivement dans les systèmes de Ca et de Nd purs.

Dans le cadre de cette thèse, notre intérêt principal concerne les manganites semi-dopés, en particulier le système Nd/Ca dans le cas des simulations. Un bon accord global a été obtenu entre les structures calculées et observées, le meilleur accord avec l'expérience pour la maille élémentaire ayant été obtenu dans le cadre des calculs sans correction de Hubbard. L'effet Jahn-Teller inverse observé expérimentalement, a été correctement reproduit par tous les calculs basés sur des mailles simple, de même que l'inclinaison des octaèdres.

Les tendances obtenues au niveau de la stabilité relative des structures magnétiques se comportent de manière similaire au système Ca pur à savoir des structure FM et AFM stabilisées dans le cadre des calculs respectivement avec et sans correction de Hubbard. Cependant la structure de type C s'est avérée être l'une des structures magnétiques les moins stables. La densité d'états n'a pas montré un gap d'énergie même dans le cadre de la correction de Hubbard à partir de la structure la plus appropriée comportant un ordre magnétique de type C. Enfin, ces calculs sur les mailles simples ont montré une petite différence entre les moments magnétiques des ions de manganèse (respectivement 3.80 et 3.81 μ_B).

Afin d'améliorer les calculs sur la structure d'ordre magnétique CE, la super-maille $a(2,2,1)$ a été considérée. Dans cette approche, l'accord structural a été moins bon en terme d'effet de tilting octaédrique et le gap d'énergie au niveau de la densité d'états n'a également pas pu être reproduit avec la correction de Hubbard. Toutefois, ce calcul a permis une amélioration significative au niveau des moments magnétiques des ions de manganèse avec des valeurs calculées très proches de celles obtenues pour les systèmes purs (3.8 et 4.0 μ_B), indiquant un niveau important d'ordre de charge. L'application du même protocole de simulation au système semi-dopé Lu-Ca n'a pas permis d'obtenir le gap d'énergie contrairement aux calculs publiés sur le système La-Ca ce qui est relativement surprenant étant donné la similitude électronique entre le Lu et le La.

Ces résultats nous permettent de conclure que les calculs DFT effectués au cours de cette étude reproduisent globalement bien les aspect structuraux des manganites purs et semi-dopés. En dépit du fait que toutes les structures magnétiques ont été stabilisées avec succès et par la suite étudiées en détail, nos résultats ne sont pas en accord avec l'expérience quant à la structure magnétique la plus stable. Pour tous les systèmes, la structure de bande électronique et la DOS semblent corrects indiquant une occupation des orbitales Mn-d et leur chevauchement et leur hybridation avec les orbitales O-p. Cependant, le gap d'énergie exigé pour ces

systemes isolants a seulement pu être calculé pour les systemes purs. Les calculs de super-maille ont montré quant à eux un niveau important d'ordre de charge à travers les moments magnétiques sur les ions Mn.

En conclusion, les structures électroniques et magnétiques sont très sensibles aux détails structuraux. Nous avons systématiquement optimisé tous les paramètres structuraux et pensons, rétrospectivement, qu'il serait utile d'exécuter des calculs directement sur les structures expérimentalement déterminées.

6

General conclusions

The goal of this thesis was to study systematically the structural and magnetic properties in half-doped manganitic compounds with the chemical formula: $\text{Ln}_{1-x}\text{Ca}_x\text{MnO}_3$ ($\text{Ln} = \text{Pr, Nd, Dy, Ho, Er, Tm, Yb}$ and Lu). The series is not complete because the compounds with $\text{Ln} = \text{Sm, Eu}$ and Gd have a very strong absorption cross-section for neutrons and alternative isotopes are very expensive. We studied the magnetic and structural properties using macroscopic magnetic measurements (susceptibility), neutron diffraction and ab-initio calculations (DFT). The FC-ZFC susceptibility measured by SQUID instrument, were studied in the temperature range $5 \div 530$ K, with an applied magnetic field of 500 G. First of all, these magnetic measurements determined the choice of temperatures in the diffraction measurements, in particularly with respect to the T_{CO} temperature. The analysis of the susceptibility allows us to define the nature of magnetic correlations above and below the T_{CO} in the framework of the Zener polaron theory, as proposed by Daoud-Aladine [39]. Above the T_{CO} , the inverse of susceptibility follows the Curie law where the FM correlations are present, with an enhancement of double exchange (DE). Below T_{CO} , there is a region where the inverse susceptibility has a Curie-Weiss behavior associated with the AFM correlations.

We studied crystal and magnetic structure of samples containing Pr, Nd, Dy, Ho, Er, Tm and Lu by neutron powder diffraction (NPD) as a function of temperature ($10 \div 300$ K). Then, we analysed the effect of the change of ionic radius of lanthanide on the magnetic correlations. We determined: cell parameters, volume cell, atomic coordinates, bond lengths and angles and magnetic structure and we analysed the JT distortion, tilting effects and bandwidth (W) of the e_g level of the Mn-d orbital. We found a $Pbnm$ symmetry group throughout the temperature range studied for each sample studied. We did not observe any structural phase transition as reported

previously by other groups for Pr compounds with composition closed to 0.5. For all samples, we found an inverse JT distortion with an octahedral compression along the z-direction. A singularity is observed corresponding to T_{CO} . In particular, the bandwidth (W) of e_g in the xy-plane is smaller than that in the z-direction, which we interpret as a reduction of the carrier mobility in the xy-plane. We found a decrease of W below T_{CO} corresponding to a localization of the carriers which stabilises orbital and charge ordering. Far below T_{CO} (around 100 K), we observed magnetic peaks in the neutron diffraction pattern. We described this magnetic structure using two sublattices corresponding to two different propagation vectors for Mn^{3+} and Mn^{4+} . We found a *pseudo*-CE type magnetic configuration, with a canting of magnetic moments for all our samples. The diffraction results are in agreement with previous ones reported by other authors concerning Pr and Nd compounds. Although the series as a function of Ln radius is not complete, we have enough samples to study the changes of all parameters (cell parameters, W , JT) with the Ln radius. The changes are continuous and smooth, except for the percentage difference between Mn^{4+} - Mn^{3+} moments. In particular, at the extremes of the series (La, Lu compounds), we found the highest percentage variation of the moments and for the other compounds the values seem to be distributed in groups. This fact suggests that perturbative effects, like crystal field, on the 4f orbitals of the lanthanides occur.

We completed the thesis work by confronting the physical properties measured in the experimental investigation with ab-initio calculations. The computations were performed using DFT methods, adopting the GGA-PBE exchange-correlation functional, including, when needed, the Hubbard correction to take into account the strong electronic correlations. All calculations were performed using the VASP code, with the Projector Augmented Wave (PAW) method. They were purely structural involving the optimisation of the electronic structure, atomic coordinates and cell parameters.

We tested our computational method on two simple manganites: $CaMnO_3$ and $NdMnO_3$, already well studied [13, 11]. We chose to model the half-doped manganites $Nd_{0.5}Ca_{0.5}MnO_3$ and $Lu_{0.5}Ca_{0.5}MnO_3$, the Lu sample being chosen for its similarity with La, since the ionic radius is smallest in the lanthanides series due to the 4f shell being full. The calculations for the half-doped systems were performed initially in the crystallographic cell, referred to as a single cell, and then in a supercell, doubled in the a and b directions, since this structure is required to model the CE-type magnetic structure.

The structural parameters obtained from the single cell calculations for $\text{Nd}_{0.5}\text{Ca}_{0.5}\text{MnO}_3$ are in good agreement with our experimental results. The Jahn-Teller inverse effect is observed with a compression of the octahedra along z-direction. The Mn-O-Mn bond angles in the xy-plane are greater than the ones along z-direction, as found experimentally. For the single cell, we simulated A-, G-, C- and B-type magnetic configurations for the $\text{Nd}_{0.5}\text{Ca}_{0.5}\text{MnO}_3$, with and without the Hubbard correction. We found the A-type configuration as energetically most stable whereas, experimentally, we determined a CE-type state, which would be best approximated by the C-type order in the single cell. None of the DFT calculations performed could be relied upon to predict the correct magnetic structure, even for the pure manganites and when the single cell is sufficient to describe the known magnetic order. We studied in detail the electronic DOS in both approaches, but we did not observe a band gap for the half-doped systems. The calculations do show an appropriate band gap for the pure manganites provided the Hubbard correction is used to treat the electron correlation.

In order to reproduce the CE-type magnetic configuration for the half-doped manganites, we used a supercell with the magnetic moments described in two sublattices. As for the single cell calculations, we considered three Nd/Ca arrangements. We observed a quite good agreement between computational and experimental results, although the additional degrees of freedom in the supercell resulted in a worse calculation of Mn-O-Mn bond angles, which describe the tilting of octahedra. However, for all geometrical arrangements of Ln/Ca (Ln = Nd and Lu), we found an inverse Jahn-Teller effect, with Mn-O_z bond distances are smaller than Mn-O bond lengths in the xy-plane, in agreement with experimental structure. As for the single cell calculations, the supercell does not allow the correct magnetic order to be determined as the most energetically stable. Concerning the electronic DOS, a number of interesting features are observed, like the hybridisation of the O-p and Mn-d orbitals and the spin-dependent occupation of the Mn-d levels. However a band gap is not observed for either half-doped manganite, despite the similarity between the Lu and La systems, the latter being the subject of published calculations which do reveal a band gap. On a positive note, the calculated magnetic moments of the manganese atoms Mn^{4+} and Mn^{3+} , for both compounds, reveal a clear charge ordering effect as found in our experimental results.

In terms of perspectives, polarized neutron scattering would allow structural and magnetic contribution to the elastic scattering to be separated, which would in turn allow the magnetic correlations to be followed over a larger temperature range. In

non-polarised neutron diffraction, the AFM nature of the correlations in half-doped manganites gives a superposition of magnetic and nuclear peaks and the magnetic signal only becomes significant at quite low temperature. There is therefore a wide temperature range below T_{CO} in which it would be useful to have a microscopic view of magnetic fluctuations and order.

In terms of perspectives for half-doped systems, it has been recently found that the magnetic properties of half-doped manganites can be tuned by changing the grain size of powders in the nanometric range [107, 108, 109]. This fact opens a new field of investigation in manganites in which the magnetic and structural properties in nanopowders could be studied by small and wide angle diffraction.

Finally, in terms of the computational work, the results presented here need, on the one hand, to be extended to the whole Ln series. In view of the results obtained, we can expect that the structural details from a full series of calculations would be reliable. The same can be said of the charge ordering, which is clearly observed in supercell calculations. On the other hand, there are some outstanding discrepancies between our calculations and published work on other half-doped manganites in the series, particularly concerning the band structure, and these should be investigated in more detail. Given the sensitivity of the magnetic structure to fine details of the crystal structure, the first step would be to perform calculations on the most reliable crystallographic structures, without optimising the atomic coordinates and cell parameters.

Conclusions générales

Le but de ce travail était de réaliser une étude systématique des propriétés structurales et magnétiques des manganites semi-dopés de formule chimique : $\text{Ln}_{1-x}\text{Ca}_x\text{MnO}_3$ ($\text{Ln} = \text{Pr}, \text{Nd}, \text{Dy}, \text{Ho}, \text{Er}, \text{Tm}, \text{Yb}$ et Lu). La série n'est pas complète car les composés pour lesquels $\text{Ln} = \text{Sm}, \text{Eu}$ et Gd ont une section d'absorption très forte pour les neutrons et leurs isotopes sont très coûteux.

Nous avons étudié les propriétés magnétiques et structurales à l'aide de mesures magnétiques macroscopiques (susceptibilité), de diffraction de neutrons et de calculs ab-initio.

La susceptibilité a été mesurée en mode FC et ZFC par SQUID en fonction de la température ($5 \div 530$ K), avec un champ magnétique appliqué de 500 G. Ces mesures magnétiques nous ont dicté le choix des températures à utiliser pour les mesures de diffraction de neutrons. L'analyse de la susceptibilité nous a permis de définir la nature des corrélations magnétiques au-dessus et en-dessous de T_{CO} dans le cadre de la théorie des polarons de Zener comme proposé par Daoud-Aladine [39]. Au-dessus de T_{CO} , l'inverse de la susceptibilité suit la loi de Curie avec des corrélations FM et une amélioration du double échange (DE). En-dessous de T_{CO} , il y a une région où l'inverse de la susceptibilité a un comportement de type Curie-Weiss lié aux corrélations AFM.

Nous avons étudié la structure nucléaire et magnétique des échantillons contenant le Pr, Nd, Dy, Ho, Er, Tm et Lu par diffraction de neutrons sur poudres (NPD) en fonction de la température ($10 \div 300$ K). Puis, nous avons analysé l'effet du changement du rayon ionique du lanthanide sur les corrélations magnétiques.

La méthode de Rietveld nous a permis d'affiner nos données afin d'en extraire les structures nucléaires et magnétiques. Pour cela, nous avons utilisé le programme FullProf Suite. Nous avons déterminé les paramètres et le volume des

mailles, les coordonnées atomiques, les liaisons et les angles ainsi que la structure magnétiques. Nous avons également analysé le factor de JT, le tilting et la largeur de bande (W) du niveau e_g de l'orbitale d-Mn.

Le même groupe de symétrie ($Pbnm$) a pu être observée sur toute la gamme de température utilisée. Nous n'avons observé aucune transition de phase structurale comme rapporté par d'autres groupes pour des composés de Pr avec des compositions proches de 0.5.

Pour tous les échantillons, nous avons trouvé un facteur inverse de JT de compression le long de la direction z . Nous avons observé une singularité à T_{CO} . En effet, la largeur de bande (W) du niveau e_g dans le plan xy est plus petite que celle le long de l'axe z . Cette singularité a été interprétée comme une réduction de la mobilité de charge dans le de plan xy .

Nous avons trouvé une diminution de W en-dessus de T_{CO} correspondant à une localisation des porteurs de charge qui stabilisent l'OO et CO.

Très en-dessous de T_{CO} (environ 100 K), les peaks magnétiques ont pu être distingués dans le diffractogramme. Nous avons décrit la structure magnétique en utilisant deux sous-mailles correspondant à deux vecteurs de propagation différents pour Mn^{3+} et Mn^{4+} . Nous avons trouvé une configuration magnétique de type *pseudo*-CE, avec un canting des moments magnétiques pour tous nos échantillons.

Nos résultats de diffraction pour les composés Pr et Nd sont en accord avec les études antérieures menées par d'autres auteurs.

Bien que non-exhaustive, notre série de lanthanide était suffisamment complète pour une étude de l'influence du rayon du lanthanide sur des paramètres tels que la structure de la maille, la largeur de bande et l'effet de JT. Nous avons pu observé une variation continue et régulière de ces paramètres en fonction du rayon à l'exception du pourcentage de différence du moment magnétique entre Mn^{4+} et Mn^{3+} . En effet, pour ce dernier, les composés aux extrémités de la série (La et Lu) sont les composés présentant la plus grande variation de pourcentage tandis que pour les autres composés nous avons pu noter la présence de groupes. Ceci nous amène à penser que des effets perturbatifs, comme le champ cristallin sur les orbitales 4f des lanthanides, se produisent.

La seconde partie de ce travail est consacrée aux simulations ab-initio pour déterminer les propriétés nucléaires et magnétiques, présentées dans la partie expérimentale. Celles-ci ont été effectuées par la méthode DFT avec la fonctionnelle d'échange-corrélation GGA-PBE, et l'approche GGA+U (avec la correction d'Hubbard) lorsque nécessaire, pour prendre en considération les corrélations

électroniques fortes. Tous les calculs ont été menés avec le programme VASP et la méthode PAW.

Nous avons validé notre protocole de simulation sur deux manganites purs: CaMnO_3 et NdMnO_3 ayant déjà fait l'objet d'études antérieures [13, 11]. Nous avons choisi ces deux systèmes pour deux raisons: (i) cette série a déjà été initiée avec les lanthanides La et Pr [11, 12] et il nous a donc paru naturel de la poursuivre avec le lanthanide Nd; (ii) le lutetium est le lanthanide pour lequel le rayon ionique est le plus faible de la série et sa couche 4f est saturée ce qui lui confère une configuration électronique comparable au La.

Pour chaque système, la géométrie a été optimisée pour faire l'objet d'une étude des propriétés électroniques et magnétiques.

Nous avons calculé les paramètres structuraux dans le cadre de la méthode GGA sur une maille simple de $\text{Nd}_{0.5}\text{Ca}_{0.5}\text{MnO}_3$ et nous avons trouvé un bon accord avec nos résultats expérimentaux. On observe notamment l'effet de Jahn-Teller inverse avec une compression de l'octaèdre le long de la direction z. Les angles Mn-O-Mn dans le plan xy sont quant à eux plus grands que ceux le long de l'axe z et ceci en accord avec l'expérience.

Pour la maille simple nous avons simulé les configurations magnétiques A, B, C et G pour le $\text{Nd}_{0.5}\text{Ca}_{0.5}\text{MnO}_3$ en utilisant la méthode GGA et GGA+U. Nous avons trouvé que la configuration A était la plus stable d'un point de vue énergétique, en désaccord avec la configuration magnétique expérimentale de type CE. Ceci montre la limite de l'utilisation d'une maille simple. Nous avons étudié en détail la DOS électronique dans les deux approches mais aucun gap d'énergie n'a pu être observé contrairement à des études antérieures menées sur des systèmes similaires.

Afin de reproduire la configuration magnétique de type CE nous avons étendu nos calculs à des super-maillles ($2a \times 2b \times c$), avec les moments magnétiques décrits par deux sous-maillles, pour les systèmes $\text{Nd}_{0.5}\text{Ca}_{0.5}\text{MnO}_3$ et $\text{Lu}_{0.5}\text{Ca}_{0.5}\text{MnO}_3$.

Nous avons considéré trois arrangements de Nd/Ca. Nous avons appliqué le même protocole de simulation que dans le cas des mailles simples. Nous avons commencé par l'optimisation de la géométrie des super-maillles, dans la configuration magnétique AFM-A. Nous avons observé un très bon accord entre les résultats de simulation et expérimentaux. Il est intéressant de noter que pour tous les arrangements géométriques de Ln/Ca étudiés (Ln = Nd et Lu), nous avons trouvé que l'effet de Jahn-Teller inverse, avec des distances Mn- O_z plus faibles que les longueurs Mn-O dans le plan xy, était en accord avec les structures expérimentales. L'analyse de la DOS électronique pour les deux systèmes nous a permis d'observer

une hybridation qui pourrait être à l'origine de l'échec du modèle d'Hubbard pour expliquer la présence du gap énergétique. Les moments magnétiques des atomes de manganèse Mn^{4+} et Mn^{3+} calculés pour les deux systèmes correspondent à l'ordre de charge et à l'ordre orbital observés dans nos résultats expérimentaux.

En conclusion, les structures électroniques et magnétiques sont très sensibles aux détails structuraux. Nous avons systématiquement optimisé tous les paramètres structuraux et pensons, rétrospectivement, qu'il serait utile d'exécuter des calculs directement sur les structures expérimentalement déterminées.

Du point de vue expérimental, l'utilisation de la technique des neutrons polarisée (afin de séparer la contribution nucléaire et magnétique au signal élastique) pourrait nous permettre d'accéder aux corrélations magnétiques dans une gamme de températures plus étendue. En effet, dans la diffraction de neutrons standard la nature des corrélations AFM aboutit à une superposition des pics magnétiques et nucléaires et de fait la structure magnétique ne devient accessible qu'à basse température, empêchant par la même occasion l'observation des pics AFM à une température de l'ordre de T_{CO} .

Récemment il a constaté que les propriétés magnétiques des manganites semi-dopés présentent une dépendance avec la grosseur du grain des poudres dans la gamme nanométrique [107, 108, 109]. Cette observation ouvre un nouveau champ de recherche dans le domaine des manganites semi-dopés qui pourrait aboutir à une meilleure compréhension de la physique de ces composés. L'étude du changement des propriétés magnétiques et structurel dans les nanopoudres pourrait être une bonne suite du travail actuel.

A

Magnetism

In this chapter we illustrate the bases that are necessary in order to understand the manganitic compounds. Their electronic, magnetic and transport properties are correlated; therefore they depend on each other. The magnetic characteristics of the manganites are reported; they have been analyzed in the chapters 1 and 2. Magnetic measurements can detect the subtle electronic structure of a material. Since these measurement do not require contacts, they can be quite easy to perform and have made them quite standard in characterizing new materials. If the magnetic species interact, then their magnetic properties can be profoundly altered. Neighboring moments which prefer to be aligned parallel lead to ferromagnetism while antiparallel alignment gives antiferromagnetism. More complex interactions lead to ferrimagnetism, canted ferromagnetism, and spin glass behavior.

A.1 Ferromagnetism

The ground state properties of a metallic ferromagnet are believed to be fairly well described by the band theory which has advanced in the recent decades [110]. The thermal excitations and finite temperature properties, however, are more difficult because of the effects of strong electron-electron correlations in narrow energy bands. The quantum mechanical exchange interaction can lead to ferromagnetism in an electron gas within the band model, commonly known as Stoner ferromagnetism [111, 112] or itinerant electron ferromagnetism. Using the molecular field approximation, a ferromagnetic state is realized for $Jn(E_F) > 1$ where J is the average intra-atomic exchange energy per atom and $n(E_F)$ is the density of states at the Fermi level. This is also known as the Stoner condition for ferromagnetism. For $Jn(E_F) < 1$ the material is not ferromagnetic but has a Pauli susceptibility enhanced by $1/(1-Jn(E_F))$ [113]. This factor is called the Stoner enhancement factor.

A.1.1 Curie Temperature

At a given temperature, any metal, usually attracted from a magnet loses its possibility to be magnetized. This temperature is known as Curie temperature, T_C (Curie point). The metal is no more attracted from the magnet because the high temperature prevents to atoms of the metal to align, and therefore to generate a magnetic field. The atoms of iron's thread (or any other metal that can be attracted from a magnet) behaved like of the little ones magnets: all of them have their north pole and south pole. The Curie temperature, T_C , affects many of the properties, there are several ways of measuring it. One of the simplest is finding the paramagnetic Curie temperature, the temperature where the linear extrapolation of the $1/\chi$ curve crosses $1/\chi = 0$ (where χ is the susceptibility). Near the critical temperature however, $1/\chi$ is not necessarily linear in T since $1/\chi = (T - T_C)^\gamma$ where γ is usually large than 1. Thus the paramagnetic Curie temperature is usually slightly larger than the true critical temperature. The most basic definition of T_C for a ferromagnet is the temperature where the spontaneous magnetization drops to zero. Unfortunately due to demagnetization effects, the zero applied field magnetization will drop to zero at T_C faster and less uniformly than expected. In an applied field, the magnetization does not drop to zero because of the large susceptibility near T_C . However, below T_C the magnetization has a negative curvature while above T_C it has a positive curvature. Thus the inflection point of

the M vs. T curve (denoted here as the inflection T_C) is often used to measure the Curie temperature. In the mean field model, the inflection T_C is quite close to the real critical temperature.

A.2 Antiferromagnetism

A substance, in which the neighboring magnetic moments align antiparallel is called an antiferromagnet. In the ordered state, there is often no net moment in zero field. Thus magnetization measurements cannot easily measure the magnetic order, for this purpose we will use neutron diffraction, in which any of the magnetic peaks is a direct measure of the ordering. In a magnetic field, an antiferromagnet has a small positive susceptibility. Above the ordering temperature, or Néel temperature T_N , the susceptibility can be well described by the Curie-Weiss law used for ferromagnets. Since the interactions are antiparallel, the coupling is of the opposite sign as that for a ferromagnet. This leads to a negative paramagnetic Curie temperature $T_C \approx T_N$, where the susceptibility above T_N is given by:

$$\chi_{mol} = \frac{N_a \mu_B g^2 J(J+1)}{3K_B(T - \Theta_p)} \quad (\text{A.1})$$

Below the ordering temperature T_N , M vs. H is still linear with no $H = 0$ magnetization, but the susceptibility depends on the orientation of the magnetic field with respect to that of the magnetic moments [78].

A.2.1 Weiss model of an antiferromagnet and Néel temperature

When the material presents the negative exchange interaction, $J < 0$, it is an antiferromagnet. Very often this occurs in systems which can be considered as two interpenetrating sublattices, on one of which the magnetic moments point up and on the other of which the point down. The nearest neighbours of each magnetic moment will then be entirely on the other sublattice. Initially we will therefore assume that the molecular field on one sublattice is proportional to the magnetization of the other sublattice. So, we have the 'up-sublattice', called '+', and 'down-sublattice', called '-'; then, the molecular field on each sublattice is:

$$B_+ = -|\lambda| M_- \quad B_- = -|\lambda| M_+ \quad (\text{A.2})$$

where λ is the molecular field constant which is now negative. On each sublattice, the molecular field is therefore given by :

$$M_{\pm} = M_S B_J \frac{g j \mu_B J |\lambda| M_{\mp}}{K_B T} \quad (\text{A.3})$$

The two sublattices are equivalent in everything except the direction of the moment so that: $|M_+| = |M_-| \equiv |M|$, and hence:

$$M = M_S B_J \left(\frac{g j \mu_B J |\lambda| M}{K_B T} \right) \quad (\text{A.4})$$

The molecular field on each sublattice will follow exactly the form shown in Fig. A.1 and will disappear for temperatures above transition temperature, known as the Neél temperature T_N , which is defined:

$$T_N = \frac{g j \mu_B (J + 1) |\lambda| M_S}{3 K_B} = \frac{n |\lambda| \mu_{eff}^2}{3 K_B} \quad (\text{A.5})$$

It is temperature at which a ferromagnetic material becomes paramagnetic. The Neél temperature, T_N , is analogous to the Curie temperature, T_C , for the ferromagnetic materials. Although the magnetization on each sublattice will follow the form in Fig. A.1, the two magnetizations will be in opposite directions so that the net magnetization $M_+ + M_-$ of the antiferromagnet will be zero. One can define a quantity known as the 'staggered magnetization' as the difference of the magnetization on sublattices, $M_+ - M_-$. This amount is then non-zero for temperatures below T_N .

A.2.2 Critical Temperature

As the temperature approaches the critical temperature T_C , the spontaneous magnetization vanishes and the susceptibility diverges. This makes these properties not analytic near T_C . The observed properties are well described by a power law $|T - T_C|^n$ where n is a scaling exponent. For example, the spontaneous magnetization varies as $(T_C - T)^\beta$ for $T < T_C$, while the susceptibility varies as $(T_C - T)^\gamma$ for $T > T_C$, and for $T = T_C$ (critical isotherm) $M^\delta = H$. The scaling exponents in the critical region are called critical exponents. The critical exponents are very similar for a wide range of second order phase transitions. They tend to depend only on the general form of the interaction causing the phase transition, such as the dimensionality, and not on the particular material. Thus most ferromagnets fall into the universality class of 3-dimensional Heisenberg or Ising ferromagnets. There are only two unique critical exponents in each universality class. The others are related via the scaling relations such as $\gamma = \beta(\delta - 1)$.

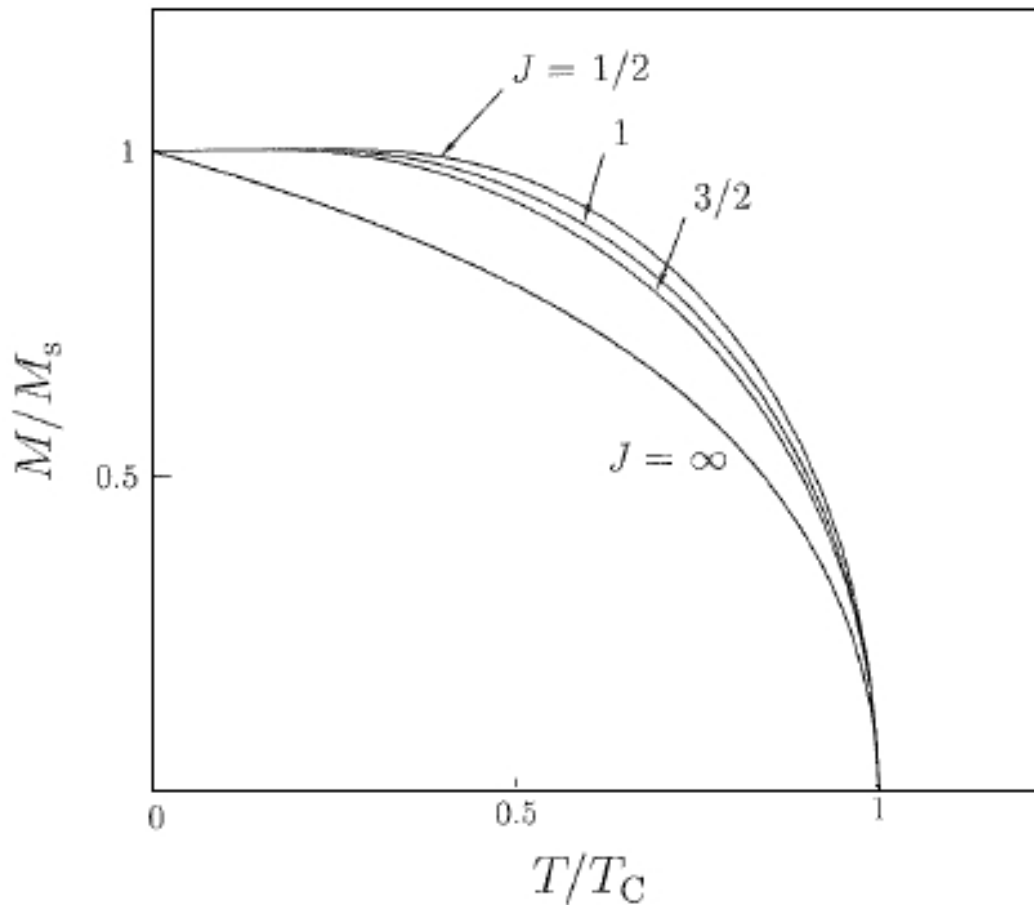


Figure A.1: The mean-field magnetization as function of temperature, performed for different values of J .

A.3 Paramagnetism and Diamagnetism

Atoms are made of well separated charged particles which move independently and can exhibit magnetic moments. A material can have different magnetic responses: a diamagnetic response is that for which the susceptibility is negative while a positive contribution to the susceptibility is paramagnetic.

A.3.1 Paramagnetism

Electrons in a metal can be partitioned into spin-up and spin-down bands, parallel and antiparallel to an applied magnetic field H . The magnetic field will lower the energy of the spin-up band compared to the spin-down band (by $2\mu_B H$, where μ_B is Bohr magneton) and spin-down electrons will flip their spins and pour over into the spin-up band. The number of electrons (per volume) that need to

flip their spins is approximately the density of electronic states, $n(E_F)$ times one half of the energy splitting. This produces a net magnetization proportional to the magnetic field and therefore a positive susceptibility, $\chi_{vol} = \mu_B^2 n(E_F)$. A more sophisticated statistical-mechanical derivation produces the same result with small corrections proportional to T^2 . The Pauli susceptibility of a metal should thus be nearly temperature independent and about the same magnitude as the Larmor diamagnetism. If a material has unpaired electrons, their magnetic spins will be highly susceptible to a magnetic field. The energy to orient the spins comes from the magnetic energy MH which for an atom with effective magnetic moment p , is $\mu_B p H$. The thermal energy $k_B T$, randomizes the spins to oppose the alignment, so the amount of alignment is roughly proportional to $\mu_B p H / k_B T$. The net magnetization is then $\mu_B p$ times the fraction of moments that are aligned. So, the magnetic susceptibility of free spins should behave like $\mu_B^2 p^2 / k_B T$.

A.3.2 Diamagnetism

Electrons in an atom are essentially free charges orbiting around nuclei, therefore the application of a magnetic field, by Lenz's law, induces an opposing magnetic moment. The resulting magnetic susceptibility is therefore negative and known as Larmor or core-electron diamagnetism. Both the classical and quantum mechanical analysis yield the same result, namely that the diamagnetic susceptibility of an atom or ion is proportional to the number of electrons it contains (Z) and to its cross section.

B

Systematic study of half-doped manganites

B.0.3 Pnma vs. Pbnm symmetry group

In this paragraph the relation between Pnma and Pbnm is discussed. Orthorhombic LnMnO_3 compounds have space group Pnma, this notation is in accordance with crystallographic conventions. The physics community prefers to name the doubled axis as the c axis, which yields the space group Pbnm. These space groups are equivalent and are related via a simple transformation. The structure refinement of LnMnO_3 in space group *Pnma* yields for the lattice parameters: $a_1 \gg \sqrt{2}a_p; b_1 \gg 2a_p; c_1 \gg \sqrt{2}a_p$, where a_{ip} is the lattice parameter of the cubic perovskite subcell. Space group *Pbnm* yields $a_2 \gg \sqrt{2}a_p; b_2 \gg \sqrt{2}a_p; c_2 \gg 2a_p$. The transformation from Pnma to Pbnm is a rotation of the whole system by 90° : $\text{Pnma} \Rightarrow \text{Pbnm}$:

- $a_1 \Rightarrow b_2$
- $b_1 \Rightarrow c_2$
- $c_1 \Rightarrow a_2$

This can easily be seen from the symmetry symbols. The mirror plane, m , in Pnma is transferred from the second to the third position in Pbnm. This means that the mirror plane is perpendicular to the doubled b_1 axis and the doubled c_2 axis, respectively. Similarly the diagonal glide plane, n , is transferred from the first to the second position; the diagonal glide plane is perpendicular to the a_1 axis and the b_2 axis, respectively. The symbol a represents a glide plane perpendicular to the c_1 axis with a 'glide' component of half the vector a_1 . Likewise, the symbol

b represents a glide plane perpendicular to the a_2 axis with a 'glide' component of half the vector b_1 .

B.0.4 Structural and magnetic properties of $\text{Ln}_{0.5}\text{Ca}_{0.5}\text{MnO}_3$, Ln = Dy, Ho, Er, Tm and Lu

From the Rietveld analysis we found that Pr, Nd, Ho and Lu are single phase samples with an occupancy of 0.5. The other samples resulted composed principally of $\text{Ln}_{0.5}\text{Ca}_{0.5}\text{MnO}_3$ but with a presence of a second phase with composition very closed to 0.5.

In particular, we considered that the compound containing Ho presents the

Samples 1-phase	Percentage	Samples 2-phase	Percentage
$\text{Pr}_{0.5}\text{Ca}_{0.5}\text{MnO}_3$	100	$\text{Pr}_{0.5}\text{Ca}_{0.5}\text{MnO}_3$	0
$\text{Nd}_{0.5}\text{Ca}_{0.5}\text{MnO}_3$	100	$\text{Nd}_{0.5}\text{Ca}_{0.5}\text{MnO}_3$	0
$\text{Dy}_{0.5}\text{Ca}_{0.5}\text{MnO}_3$	66.57	$\text{Dy}_{0.6}\text{Ca}_{0.4}\text{MnO}_3$	33.43
$\text{Ho}_{0.5}\text{Ca}_{0.5}\text{MnO}_3$	74.52	$\text{Ho}_{0.53}\text{Ca}_{0.47}\text{MnO}_3$	25.48
$\text{Er}_{0.5}\text{Ca}_{0.5}\text{MnO}_3$	62.83	$\text{Er}_{0.6}\text{Ca}_{0.4}\text{MnO}_3$	37.17
$\text{Tm}_{0.5}\text{Ca}_{0.5}\text{MnO}_3$	46.47	$\text{Tm}_{0.4}\text{Ca}_{0.6}\text{MnO}_3$	53.53
$\text{Lu}_{0.5}\text{Ca}_{0.5}\text{MnO}_3$	81.35	$\text{Lu}_{0.3}\text{Ca}_{0.7}\text{MnO}_3$	18.65

Table B.1: Table of first and second phase of our samples, obtained by Rietveld refinement of NPD data measured on D1A and D20 at ILL, at $\lambda = 1.9$ [Å].

occupancy in the second phase very close to 0.5 and the sample containing Lu has the percentage of the second phase negligible respect to the first phase at $x = 0.5$.

We reported the structural and magnetic results with compounds (with $x = 0.5$) containing Dy, Ho, Er (see table B.2), Tm and Lu (see table B.3.) Furthermore, the patterns at room temperature are shown for the compounds DyCa in fig. B.1, for HoCa in fig. B.2, for ErCa in fig. B.3 and for TmCa in fig. B.4. The patterns of LuCa compound at room temperature is reported in the chapter 4.

-	-	Dy	Dy	Ho	Ho	Er	Er
Parameters		300 [K]	20 [K]	300 [K]	10 [K]	300 [K]	25 [K]
a[Å]		5.3119(5)	5.3194(4)	5.3077(2)	5.3143(1)	5.2887(4)	5.2928(3)
b[Å]		5.4498(5)	5.4601(3)	5.4609(1)	5.4667(1)	5.4547(3)	5.4546(3)
c[Å]		7.4519(6)	7.4065(5)	7.4519(3)	7.4026(1)	7.4368(6)	7.3921(5)
V[Å ³]		215.7249(5)	215.1122(4)	215.9916(2)	215.0576(1)	214.5403(6)	213.4067(6)
Ln/Ca	x	0.9927(1)	0.9901(1)	0.9904(1)	0.9911(1)	-0.0047(1)	0.0004(1)
	y	0.0569(1)	0.0538(1)	0.0544(1)	0.0556(1)	0.0597(1)	0.0559(1)
O1	x	0.2931(1)	0.2871(1)	0.2987(1)	0.2909(1)	0.2928(1)	0.2911(1)
	y	0.7016(1)	0.7049(1)	0.7035(1)	0.7037(1)	0.7026(1)	0.7030(1)
	z	0.9585(1)	0.9521(1)	0.9567(1)	0.9568(1)	0.9582(1)	0.9565(1)
O2	x	0.4145(1)	0.3993(1)	0.4134(1)	0.4122(1)	0.4126(1)	0.4081(1)
	y	0.9688(1)	0.9668(1)	0.9758(1)	0.9759(1)	0.9739(1)	0.9706(1)
Mn-O _{eq} [Å]		1.937(2)	1.926(2)	1.963(3)	1.932(3)	1.928(4)	1.924(5)
Mn-O _{eq} [Å]		1.977(2)	2.001(2)	1.967(3)	1.991(3)	1.982(5)	1.988(5)
Mn-O _{ap} [Å]		1.924(4)	1.936(3)	1.923(1)	1.913(1)	1.921(2)	1.918(2)
Mn-O _{eq} -Mn[deg]		150.1(2)	145.4(2)	151.2(1)	150.6(1)	150.8(2)	149.1(1)
Mn-O _{ap} -Mn[deg]		157.9(7)	152.1(4)	151.4(1)	152.8(1)	152.6(2)	151.5(2)
μ_{Mn}^{3+}		-	2.73(8)	-	2.55(3)	-	2.52(7)
μ_{Mn}^{4+}		-	2.53(8)	-	2.35(3)	-	2.32(7)
φ		-	134°	-	220°	-	131°
ϑ		-	114°	-	87°	-	102°
Bragg-f		8	7	3.8	3.6	5.1	5.7
R(F2)		2.56	4.4	5.02	4.92	3.13	3.01
χ^2		6	2.1	2.8	2.1	3.0	3.19

Table B.2: Dy_{0.5}Ca_{0.5}MnO₃, Ho_{0.5}Ca_{0.5}MnO₃ and Er_{0.5}Ca_{0.5}MnO₃ structural parameters determined at room and lower temperature, measured on D1A at ILL, at $\lambda = 1.9$ [Å]; the manganese atom is in high symmetry site (1/2, 0, 0).

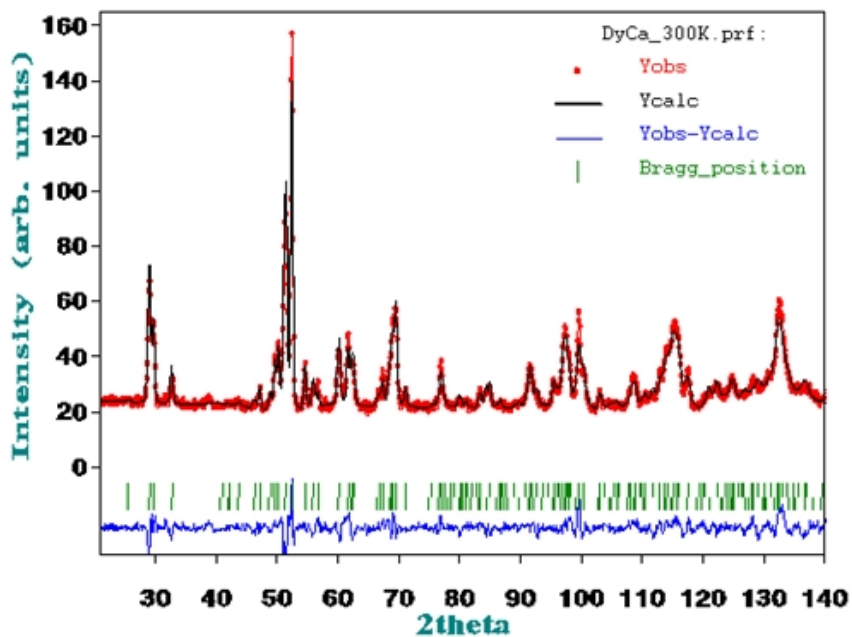


Figure B.1: Pattern of Dy_{0.5}Ca_{0.5}MnO₃ at T = 300 K and λ = 1.9 Å

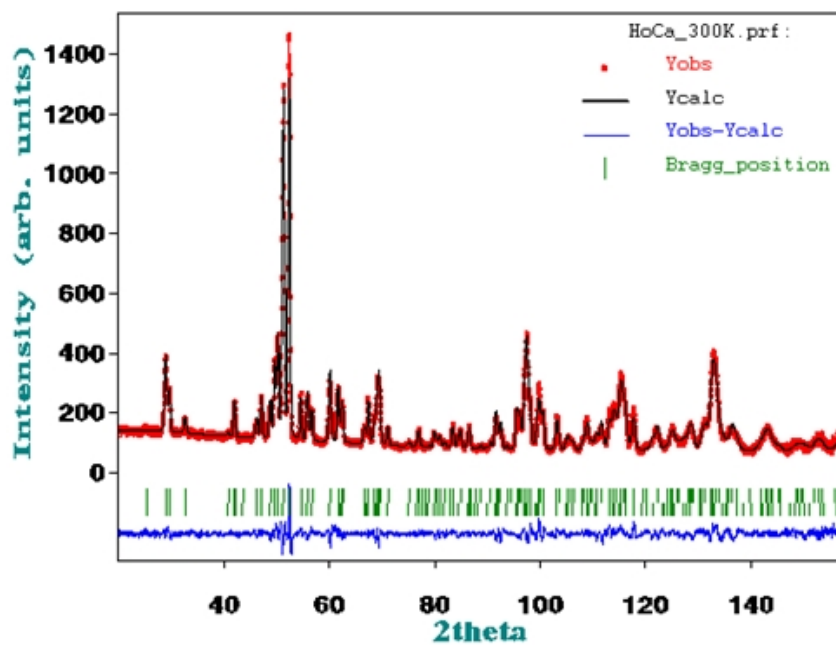


Figure B.2: Pattern of Ho_{0.5}Ca_{0.5}MnO₃ at T = 300 K and λ = 1.9 Å

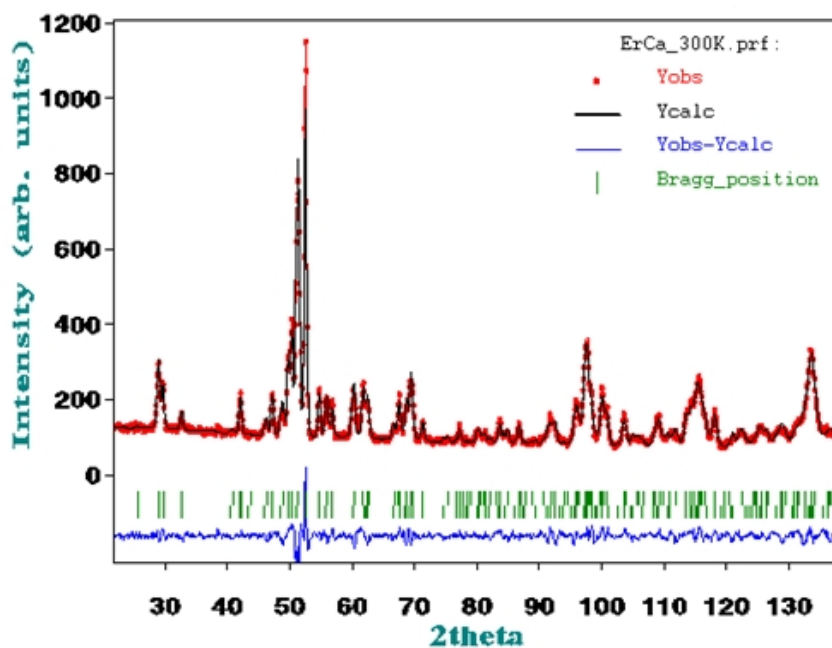


Figure B.3: Pattern of $\text{Er}_{0.5}\text{Ca}_{0.5}\text{MnO}_3$ at $T = 300\text{ K}$ and $\lambda = 1.9\text{ \AA}$

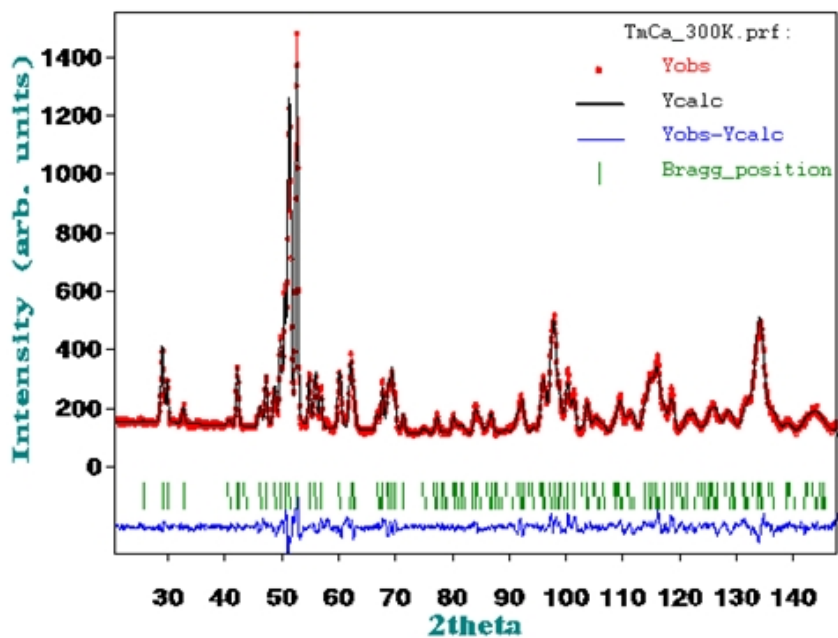


Figure B.4: Pattern of $\text{Tm}_{0.5}\text{Ca}_{0.5}\text{MnO}_3$ at $T = 300\text{ K}$ and $\lambda = 1.9\text{ \AA}$

-	-	Tm	Tm	Lu	Lu
Parameters		300 [K]	20 [K]	300 [K]	10 [K]
a[Å]		5.2862(6)	5.2894(3)	5.2647(3)	5.3143(1)
b[Å]		5.5171(4)	5.5078(3)	5.5044(2)	5.4667(1)
c[Å]		7.4247(7)	7.3914(5)	7.4145(4)	7.4026(1)
V[Å ³]		216.5381(6)	215.3321(4)	214.8645(3)	215.0576(1)
Ln/Ca	x	0.9792(1)	0.9851(1)	-0.0187(1)	-0.0153(1)
	y	-0.0650(1)	-0.0672(1)	0.0648(1)	0.0668(1)
O1	x	0.8036(1)	0.8022(1)	0.3051(1)	0.3007(1)
	y	0.2010(1)	0.1995(1)	0.6996(1)	0.6995(1)
	z	0.0500(1)	0.0475(1)	-0.0492(1)	-0.0494(1)
O2	x	0.0919(1)	0.0901(1)	0.4065(1)	0.4091(1)
	y	0.5253(1)	0.5257(1)	-0.0291(1)	-0.0279(1)
Mn-O _{eq} [Å]		1.984(7)	1.972(5)	1.979(4)	1.961(3)
Mn-O _{eq} [Å]		1.986(7)	1.989(5)	1.981(5)	1.993(3)
Mn-O _{ap} [Å]		1.924(3)	1.914(2)	1.924(2)	1.912(1)
Mn-O _{eq} -Mn[deg]		148.5(3)	149.2(2)	148.2(2)	148.9(1)
Mn-O _{ap} -Mn[deg]		149.5(1)	149.9(2)	148.8(1)	149.5(1)
μ_{Mn}^{3+}		-	2.28(5)	-	1.09(6)
μ_{Mn}^{4+}		-	2.19(5)	-	0.89(6)
φ		-	235°	-	229°
ϑ		-	88°	-	50°
Bragg-f		5.1	5	3.8	4.5
R(F2)		3.16	2.8	5.02	2.57
χ^2		4.8	4.1	2.8	3.1

Table B.3: Tm_{0.5}Ca_{0.5}MnO₃ and Lu_{0.5}Ca_{0.5}MnO₃ structural parameters determined at room and lower temperature, measured on D1A at ILL, at $\lambda = 1.9$ [Å]; the manganese atom is in high symmetry site (1/2, 0, 0).

Bibliography

- [1] G. Jonker and J. V. Santen *Physica* **16** (1950) 337.
- [2] W. Koehler and E. Wollan *Phys. Rev.* **100** (1955) 545.
- [3] W. Koehler and E. Wollan *Phys. Rev.* **97** (1955) 1177.
- [4] Y. Tokura, *Fundamental features of colossal magnetoresistive manganese oxide*. Gordon and Breach, London, 1999.
- [5] J. Goodenough *Phys. Rev.* **100** (1955) 564.
- [6] C. Shull and J. S. Smart *Phys. Rev.* **76** (1949) 1257.
- [7] R. Kusters, J. Singleton, D. Keen, R. McGreevy, and W. Hayes *Physica B* **155** (1989) 362.
- [8] R. von Helmolt, J. Wecker, B. Holzapfel, L. Schultz, and K. Samwer *Phys. Rev. Lett.* **71** (1993) 2331.
- [9] C. Searle and S. Wang *Canadian Journal of Physics* **47** (1969) 2703.
- [10] A. Daoud-Aladine, *Étude par diffraction des corrélations entre magnétisme et structure des manganites à ordre de charge*. PhD thesis, Université Paris XI, UFR Scientifique D'Orsay.
- [11] K. Yamauchi, F. Freimuth, S. Blügel, , and S. Picozzi *Phys. Rev. B* **78** (2008) 014403.
- [12] V. Anisimov, I. Elfimov, and M. Korotin *Phys. Rev. B* **55** (1997) 15494.
- [13] A. Filippetti and N. Hill *Phys. Rev. B* **65** (2002) 195120.
- [14] J. van Santen and G. Jonker *Physica* **16** (1950) 599–600.
- [15] Y. Tomioka, A. Asamitsu, H. Kawahara, H. Moritomo, and Y. Tokura *Phys. Rev. B* **53** (1996) R1689.
- [16] P. Levy, F. Parisi, G. Polla, D. Vega, G. Leyva, H. Lanza, R. Freitas, and L. Ghivelder *Phys. Rev. B* **62** (2000) 6437.
- [17] J. Loudon, N. Mathur, and P. Midgley *Nature* **420** (2002) 797–800.

- [18] M. Cheong, M. Castro, R. Burriel, and S. Cheong *J. Magn. Magn. Mater.* **196-197** (1999) 512.
- [19] P. Joy and S. Date *J. Magn. Magn. Mater.* **220** (2000) 106.
- [20] B. van Aken, O. Jurchescu, A. Meetsma, Y. Tomioka, Y. Tokura, and T. Palstra *Phys. Rev. Lett.* **90** (2003) 066403.
- [21] J. Dho, I. Kim, S. Lee, K. Kim, H. Lee, J. Jung, and T. Noh *Phys. Rev.* **B 59** (1999) 492.
- [22] C. Chen, S. Cheong, and H. Hwang *J. Appl. Phys.* **81** (1999) 4326.
- [23] M. Tokunaga, N. Miura, Y. Tomioka, and Y. Tokura *Phys. Rev.* **B 57** (1998) 5259.
- [24] C. Martin, A. Maignan, M. Hervieu, and B. Raveau *Phys. Rev.* **B 60** (1999) 12191.
- [25] W. Harrison, *Electronic structure and the properties of solids. The physics of the chemical bond.* Freeman, San Francisco, 1980.
- [26] Z. Jirak, S. Krupicka, Z. Simsa, M. Dlouha, and Z. Vratislav *J. Magn. Magn. Mater.* **53** (1985) 13.
- [27] T. Hotta and E. Dagotto *Phys. Rev.* **B 61** (2000) R11879.
- [28] P. Radaelli, G. Iannone, M. Marezio, H. Hwang, S.-W. Cheong, J. Jorgensen, and D. Argyriou *Phys. Rev.* **B 56** (1997) 8265.
- [29] V. Goldschmidt *Skriker Norske Videnskaps-Akad. Oslo, I. Mat.-Nat. Kl.* **8** (1926) .
- [30] J. Coey, M. Viret, and S. V. Molnár *Adv. in Phys.* **48** (1999) 167.
- [31] C. Zener *Phys. Rev.* **81** (1951) 440.
- [32] C. Zener *Phys. Rev.* **82** (1951) 403.
- [33] E. Dagotto, T. Hotta, and A. Moreo *Phys. Rep.* **1** (2001) 344.
- [34] J. Kanamori *J. Appl. Phys.* **31** (1960) 14S.

- [35] Y. Yamada, O. Hino, S. Nohdo, and R. Kanao *Phys. Rev. Lett.* **77** (1996) 904.
- [36] J. Elemans, B. van Laar, K. van der Veen, and B. Loopstra *J. Solid State Chem.* **3** (1971) 238.
- [37] A. Millis *Nature* **392** (1998) 147.
- [38] J. Burgy, A. Moreo, and E. Dagotto *Phys. Rev. Lett.* **92** (2004) 097202.
- [39] A. Daoud-Aladine, J. Rodríguez-Carvajal, L. Pinsard-Gaudart, T. Fernández-Díaz, and A. Revcolevschi *Phys. Rev. Lett.* **89** (2002) 097205.
- [40] M. Coey *Nature* **430** (2004) 155.
- [41] C. Zener *Phys. Rev.* **82** (1951) 403.
- [42] P. DeGennes *Phys. Rev.* **118** (1960) 141.
- [43] H. Jahn and E. Teller *Proc. R. Soc. London A* **161** (1937) 5220.
- [44] D. Worledge, G. Snyder, M. Beasley, and T. Geballe *J. Appl. Phys.* **80** (1996) 5158.
- [45] J. D. Teresa, K. D'órr, K. M'uller, L. Schultz, and R. Chakalova *Phys. Rev. B* **58** (1998) 5928.
- [46] J. Medvedeva, V. Anisimov, O. Mryasov, and A. Freeman *J. Phys. Condens. Matter* **14** (2002) 4533.
- [47] D. Efremov, J. van den Brink, and D. Khomskiik *Cond. Mat* **V1** (2006) 0306651.
- [48] M. Cieplak *Phys. Rev. B* **18** (1978) 3470.
- [49] P. Anderson and H. Hasegawa *Phys. Rev.* **100** (1955) 675.
- [50] K. Kubo and N. Ohata *J. Phys. Soc. Japan* **33** (1972) 21.
- [51] K. D'órr *J. Phys. D: Appl. Phys.* **39** (2006) 125.
- [52] A. Urushibara, Y. Moritomo, T. Arima, A. Asamitsu, G. Kido, and Y. Tokura *Phys. Rev. B* **51** (1995) 14103.

- [53] H. F. et al. *J. Phys. Soc. Japan.* **67** (1998) 1799.
- [54] R. Kajimoto, H. Yoshizawa, H. Kawano, H. Kuwahara, Y. T. K. Ohoyama, and M. Ohashi *Phys. Rev. B* **60** (1999) 9506.
- [55] K. Ahn, T. Lookman, and A. Bishop *Nature* **428** (2004) 401.
- [56] N. Veglio, F. Bermejo, J. Gutierrez, J. Barandiarán, A. Peña, M. González, P. Romano, and C. Mondelli *Phys. Rev. B* **71** (2005) 212402.
- [57] Q. Design, *Magnetic Property Measurement Systems: MPMS-5S User Manual*. Quantum Design, San Diego, 1998.
- [58] G. Bacon, *Neutron Diffraction*. Clarendon Press, Oxford, 1975.
- [59] G. Squires, *Introduction to the theory of thermal neutron scattering*. Cambridge University Press, Cambridge, 1978.
- [60] W. Bragg and W. L. Bragg *Proc. R. Soc. Lond.* **88** (1913) 428.
- [61] W. L. Bragg *Proc. Camb. Phil. Soc.* **17** (1913) 43.
- [62] H. Rietveld *J. Appl. Cryst.* **2** (1969) 65.
- [63] J. Rodríguez-Carvajal *Fullprof Program*, <http://www.ill.eu/sites/fullprof/>.
- [64] A. Dianoux and J. Lander, *Neutron Data Booklet*. ILL, 2001.
- [65] S. Husain, R. Choudhary, R. Kumar, S. Patil, J. Srivastava, and J. Pramana *J. Phys* **58** (2002) 1045.
- [66] D. Cox, P. Radaelli, M. Marezio, and S. Cheong *Phys. Rev. B* **57** (1998) 3305.
- [67] A. Martinelli, M. Ferretti, C. Castellano, C. Mondelli, M. R. Cimberle, M. Tropeano, and C. Ritter *Phys. Rev. B* **73** (2006) 064423.
- [68] C. Frontera, J. García-Munõz, A. Llobet, C. Ritter, J. Alonso, and J. Rodríguez-Carvajal *Phys. Rev. B* **62** (2002) 3002.
- [69] F. Millange, S. de Brion, , and G. Chouteau *Phys. Rev. B* **62** (2000) 5619.
- [70] A. Martinelli and M. Ferretti *Powder Diffraction* **20** (2005) 22.

- [71] <http://icsd.ill.fr/icsd/index.html>.
- [72] S. Satpathy *Phys. Rev. Lett.* **76** (1996) 960.
- [73] J. García-Munõz, M. Suaaidi, J. Fontcuberta, and J. Rodríguez-Carvajal *Phys. Rev. B* **55** (1997) 34.
- [74] P. Woodward *Acta Crystallogr.* **B53** (1997) 44.
- [75] <http://cms.mpi.univie.ac.at/vasp/>.
- [76] P. Blochl *Phys. Rev. B* **50** (1994) 17953.
- [77] M. Born and R. Oppenheimer *Zur Quantentheorie der Molekeln. Ann. Phys.* **t. 84** (1927) 457.
- [78] N. Ashcroft and N. Mermin, *Solid State Physics*. Saunders, 1976.
- [79] R. Jones and O. Gunnarsson *Rev. Mod. Phys.* **61** (1989) 689.
- [80] G. Vignale and M. Das, *Electronic Density Functional Theory: Recent Progress and New Directions*. Plenum Press, New York and London, 1998.
- [81] P. Hohenberg and W. Kohn *Phys. Rev.* **136** (1964) B864.
- [82] W. Kohn and L. J. Sham *Phys. Rev. A* **140** (1965) 1133.
- [83] G. Giovannetti, S. Kumar, J. van den Brink, and S. Picozzi *Phys. Rev. Lett.* **103** (2009) 037601.
- [84] J. Slater *Phys. Rev.* **81** (1951) 385.
- [85] P. Atkins and R. Friedman, *Molecular quantum mechanics*. Cambridge University Press, Cambridge, 2005.
- [86] J. Perdew, K. Burke, and M. Ernzerhof *Phys. Rev. Lett.* **77** (1996) 3865.
- [87] M. Payne, M. Teter, D. Allan, T. Arias, , and J. Joannopoulos *Rev. Mod. Phys.* **64** (1992) 1045.
- [88] A. Becke *Phys. Rev. A* **38** (1988) 3098.
- [89] D. Ceperely and B. Alder *Phys. Rev. Lett.* **45** (1980) 566.

- [90] J. Perdew and A. Zunger *Phys. Rev. B* **23** (1981) 5048.
- [91] U. V. Barth and L. Hedin *J. Phys. C* **5** (1972) 1629.
- [92] J. Perdew and Y. Wang. *Phys. Rev. B* **45** (1992) 13244.
- [93] S. Blundell, *Magnetism in Condensed Matter*. Oxford University Press, Oxford, 2004.
- [94] V. Anisimov, J. Zaanen, and O. Anderson *Phys. Rev. B* **44** (1991) 943.
- [95] V. Anisimov, I. Solovyev, M. Korotin, M. Czyzyk, and G. Sawatzky *Phys. Rev. B* **48** (1993) 16929.
- [96] I. Solovyev, P. Dederichs, and V. Anisimov *Phys. Rev. B* **50** (1994) 16861.
- [97] G. Kresse and J. Furthmuller *Phys. Rev. B* **54** (1996) 11169.
- [98] W. Temmerman, L. Petit, A. Svane, Z. Szotek, M. Luders, P. Strange, J. Staunton, I. Hughes, and B. Gyorffy, *Handbook on the Physics and Chemistry of Rare Earths*, vol. 39. North-Holland, Amsterdam, 2009.
- [99] S. Dudarev, G. Botton, S. Savrasov, C. Humphreys, and A. Sutton *Phys. Rev. B* **57** (1998) 1505.
- [100] H. Monkhorst and J. Pack *Phys. Rev. B* **13** (1976) 5188.
- [101] B. Dabrowski, S. Kolesnika, A. Baszczukb, O. Chmaissem, T. Maxwella, and J. Mais *J. of Solid State Chem.* **178** (2005) 629.
- [102] J. Blasco, C. Ritter, J. Garcya, J. M. de Teresa, J. Perez-Cacho, and M. R. Ibarra *Phys. Rev. B* **62** (2000) 5609.
- [103] C. Khattak, F. Wang, in: K.A.Jr. Gschneidner, and L. E. (Eds.), *Handbook on the Physics and Chemistry of Rare Earths*. North-Holland, Amsterdam, 1979.
- [104] T. Chatterji, B. Ouladdiaf, and D. Bhattacharya *J. Phys.: Condens. Matter* **21** (2009) 306001.
- [105] W. Yin, D. Volja, and W. Ku *Phys. Rev. Lett.* **96** (2006) 116405.

- [106] A. Muñoz, J. Alonso, M. Martínez-Lopez, J. García-Muñoz, and M. Fernández-Díaz *J. Phys.: Condens. Matter* **12** (2000) 1361.
- [107] T. Sarkar, B. Ghosh, and A. Raychaudhuri *Phys. Rev. B* **77** (2008) 235112.
- [108] M. Pėkala, V. Drozd, J. Fagnard, and P. Vanderbemden *Journal of Alloys and Compounds* **507** (2010) 350.
- [109] E. Rozenberg, M. Auslender, A. Shames, Y. Mukovskii, E. Sominski, and A. Gedanken *Journal of Alloys and Compounds* **354** (2008) 5282.
- [110] T. Moriya *J. Magn. Magn. Mater.* **100** (1991) 261–271.
- [111] E. Stoner.
- [112] D. Edwards and E. Wohlfarth *Proc. R. Soc. London Ser. A* **303** (1968) 127–137.
- [113] E. Stoner *Acta Metallurgica* **2** (1954) 259.